DEVELOPEMENT OF WIDEFIELD MULTI-CONTRAST OPTICAL METHODS FOR *IN VIVO* MICROVASCULAR SCALE IMAGING

By
Janaka Senarathna

A dissertation submitted to Johns Hopkins University in conformity with the requirements for the degree of Doctor of Philosophy

Baltimore, Maryland

March, 2017

Abstract

Traditional *in vivo* optical imaging methods rely on a single contrast mechanism, thereby limiting one's ability to characterize more than one biological variable. However, most biological systems are complex and are comprised of multiple variables. Therefore, optical methods that employ multiple contrast mechanisms and are capable of visualizing multiple biological variables would permit a more comprehensive understanding of biological systems. Multi-contrast optical imaging, therefore, has great potential for both fundamental and applied biomedical research.

The goal of this dissertation is to develop optical methods to enable multi-contrast imaging *in vivo* over a wide field of view while retaining a microvascular scale spatial resolution. We present the integration of three types of optical imaging contrast mechanisms: fluorescence (FL), intrinsic optical signals (IOS) and laser speckle contrast (LSC). Fluorescence enables tracking pre-labelled molecules and cells, IOS allow quantification of blood volume and/or intravascular oxygen saturation, and LSC permits assessment of tissue perfusion. Together, these contrast mechanisms can be harnessed to provide a more complete picture of the underlying physiology at the microvascular spatial scale.

We developed two such microvascular resolution optical multi-contrast imaging methods, and demonstrated their utility in multiple biomedical applications.

First, we developed a multi-contrast imaging system that can interrogate in *vivo* both neural activity and its corresponding microvascular scale hemodynamics in the brain of a freely moving rodent. To do this, we miniaturized an entire benchtop optical imaging system that would typically occupy 5 x 5 x 5 feet, into just 5 cm^3. Our miniaturized microscope weighs only 9 g. The miniature size and light weight permitted us to mount our microscope on a rodent's head and image brain activity *in vivo* with multiple contrast mechanisms. We used our microscope to study the functional activation of the mouse auditory cortex, and to investigate the alteration of brain function during arousal from deep anesthesia. Our miniaturized microscope is the world's first rodent head-mountable imaging system capable of interrogating both neural and hemodynamic brain activity. We envision our microscope to usher an exciting new era in neuroscience research.

Second, we developed an optical imaging system to extensively characterize microvascular scale hemodynamics *in vivo* in an orthotopic breast tumor model. We specifically designed it as a benchtop based system to allow ample space for surgical preparation and small animal manipulation. Using it, we continuously monitored *in vivo* microvascular scale changes in tissue perfusion, blood volume and intravascular oxygen saturation of an orthotopic breast tumor microenvironment for multiple hours over a field of view encompassing the entire tumor extent. This unique dataset enabled us for the first time to characterize the temporal relationship between different tumor hemodynamic variables at the scale of individual microvessels. We envision our work to inspire a whole new avenue of experimental cancer research where the role of a tumor's

hemodynamic microenvironment is extensively characterized at its native (i.e. microvascular) spatial scale.

In summary, this dissertation describes the design, implementation and demonstration of two microvascular resolution, wide-field, multi-contrast optical imaging systems. We believe these methods to be a new tool for broadening our understanding of biology.

Dissertation committee

Dr. Arvind P. Pathak (primary advisor, reader)

Russell H. Morgan Department of Radiology and Radiological Science,

Johns Hopkins University School of Medicine.

Dr. Nitish V. Thakor (reader)

Department of Biomedical Engineering,

Johns Hopkins University.

Dr. Betty M. Tyler

Department of Neurosurgery,

Johns Hopkins University School of Medicine.

Dr. Kristine Glunde

Russell H. Morgan Department of Radiology and Radiological Science,

Johns Hopkins University School of Medicine.

Acknowledgements

I would like to sincerely thank my advisor, Dr. Arvind P. Pathak. He has been an exceptional mentor in many ways that words would not suffice to describe (I will leave it at that.). And, above all thank you for being an incredibly inspiring human being. I would also like to thank the rest of my thesis committee: Dr. Nitish V. Thakor for his guidance and expertise on neuroimaging, Dr. Betty M. Tyler for her kind guidance and extensive help with animal models, and Dr. Kristine Glunde for her kind guidance regarding the optics aspects of my dissertation.

This work would not have been possible without the immense support I received from '*the Pathaks*': i.e. the Pathak Lab team. Stacy Gil, our lab manager has 'magical hands' and did an amazing job with surgical preparations. Former and current lab members: Hang Yu, Alice Zou and Callie Deng directly contributed to the design and implementation of the imaging methods described in this dissertation. The rest of the team: Darian Hadjiabadi, Namrata Batra, Akanksha Bhargava, Gayatri Susarla and Manel Dfajjal also helped in innumerable ways. Also, former Thakor Lab members Drs. Abhishek Rege, Kartikeya Murari, and Nan Li were inspirational and helpful. In addition Dr. Qihong Wang (Thakor Lab) and Dr. John Issa (Calcium Signals Lab) provided crucial help with experiments. Jay Burns, the lab manager at the Biomedical Engineering Mechanical Workshop, taught me many things about machining and helped me whenever I landed in a tough situation with system miniaturization.

My family and friends played a critical role. I would like to sincerely acknowledge the sacrifice my family made: letting go of their son after twenty five years' worth of investment without expecting anything in return. My friends Kai-Yuen Lim, Rahul Agarwal, Chelsea Zhou and Haiyun Liu have been a great asset to me, especially when I needed emotional support. Elliot Greenwald played the role of 'tech-support' for me, for almost the entirety of my PhD, by graciously being a sounding board for my ideas.

Finally, thank you to all those wonderful people who throughout the centuries have humbly toiled in the name of scientific progress. Everything I've done, I've built on your shoulders, in the hope that my work too will someday help future generations.

For the betterment of mankind

Contents

List of Tables

List of Supplementary Tables

List of Figures

List of Supplementary Figures

Chapter 1 **Introduction**

The purpose of this dissertation is to develop multi-contrast optical imaging methods that enable new *in vivo* observations previously not possible. Specifically, we have designed and fabricated two imaging systems (with complimentary processing pipelines), that answer unmet needs in today's scientific community.

1.1 Specific aims

Aim 1: To design, construct and demonstrate the utility of a miniature, rodent head-mountable, multi-contrast optical microscope that can image *in vivo* both neural and hemodynamic activity in awake animals.

Rationale: Today's miniature head-mounted microscopes that permit interrogation of brain function in freely moving animals can image either the neural activity[1, 2] or the hemodynamics[3, 4], but not both. Imaging systems that can image neural and hemodynamic activity are usually bulky and benchtop based[5, 6] and therefore typically require the animal to be anesthetized.

Approach: We overcame this barrier by: (i) implementing a novel miniaturized design that incorporated optical imaging of multiple contrast mechanisms within a compact rodent head-mountable housing, and (ii) by using computer aided 3D printing technologies and state of the art miniature optoelectronic components.

Results: We demonstrated the utility of our miniaturized microscope by (i) imaging neuronal and hemodynamic responses to auditory stimulation, (ii) performing wide-area functional mapping analogous to classic fMRI paradigms, and (iii) characterizing hemodynamic and electrophysiological changes that accompany arousal from anesthesia.

Aim 2: To build a customized optical imaging system capable of simultaneous *in vivo* interrogation of multiple microvascular scale hemodynamic variables in an orthotopic breast tumor model.

Rationale: The hemodynamic microenvironment plays a crucial role in tumor growth[7] and metastasis[8]. Therefore, the ability to characterize tumor hemodynamics at the scale in which they occur: i.e. at the microvascular scale, is crucial. However, the state of the art is to interrogate only a single tumor hemodynamic variable: e.g. either tumor oxygenation[9] or tumor perfusion[10], but not both. This precludes achieving a comprehensive understanding of the complex role hemodynamics play in tumor progression.

Approach: Therefore, we custom built a multi-contrast optical imaging system that enables us to simultaneously interrogate dynamic changes in (i) perfusion, (ii) blood volume, and (iii) intravascular oxygen saturation *in vivo* within the tumor microenvironment. We incorporated ample space for surgical and experimental manipulations necessary for *in vivo* experimentation with orthotopic tumor models by designing this as a benchtop based system.

Results: Using our custom built system to image an orthotopic breast tumor model, we demonstrated for the first time (i) simultaneous microvascular scale instabilities in tumor perfusion, blood volume and oxygenation over a duration of two hours, and (ii) heterogeneity in the temporal relationship between perfusion, blood volume and intravascular oxygen saturation at the scale of individual microvessels *in vivo*.

1.2 Contributions

This dissertation has resulted in the following publications:

(i) A review of current miniaturized optical microscope technologies.

"Yu, H., Senarathna, J., Tyler, B. M., Thakor, N. V. & Pathak, A. P. Miniaturized optical neuroimaging in unrestrained animals. *Neuroimage* **113,** 397-406 (2015)."

(ii) A miniature, rodent head-mountable multi-contrast microscope for optical neuroimaging in awake animals.

"Senarathna, J., Yu, H., Gil, S., Zou, A. L., Hadjiabadi, D. H., Wang, Q. , Issa, J. B., Tyler, B. M., Thakor, N. V., & Pathak, A. P. A Miniature Microscope for Multi-Contrast Optical Neuroimaging in Awake Animals. *Nat. Methods* (Submitted)."

(iii) A custom built multi-contrast optical imaging system for interrogating multiple aspects of a tumor's hemodynamic microenvironment.

"Senarathna, J., Gil, S., Deng, C., Fang, V., Thakor, N. V. & Pathak, A. P. *In vivo* Multi-contrast Optical Imaging Reveals Spatio-temporal heterogeneity in Tumor Hemodynamics at the Microvascular Scale. *Cancer Res.* (In preparation)."

1.3 Dissertation organization

Chapter Two: Reviews the current status of miniaturized optical microscopes. This chapter sets the stage for the development of our miniature microscope. (This chapter is an adaptation of [11].)

Chapter Three*:* Describes the design, validation and applications of our miniature microscope. (This chapter is an adaptation of [12])

Chapter Four: Introduce conventional optical techniques currently used to image tumor hemodynamics. Next, it describes our benchtop based imaging system and concludes with its use for interrogating multiple aspects of tumor hemodynamics at the microvascular scale in an orthotopic breast cancer model.

Chapter Five: Summarizes the overall conclusions and discusses future directions.

Chapter 2 **Miniaturized Optical Neuroimaging in Unrestrained Animals**

The confluence of technological advances in optics, miniaturized electronic components and the availability of ever increasing and affordable computational power have ushered in a new era in functional neuroimaging, namely, an era in which neuroimaging of cortical function in unrestrained and unanesthetized rodents has become a reality. Traditional optical neuroimaging required animals to be anesthetized and restrained. This greatly limited the kinds of experiments that could be performed in vivo. Now one can assess blood flow and oxygenation changes resulting from functional activity and image functional response in disease models such as stroke and seizure, and even conduct long-term imaging of tumor physiology, all without the confounding effects of anesthetics or animal restraints. These advances are shedding new light on mammalian brain organization and function, and helping to elucidate loss of this organization or 'dysfunction' in a wide array of central nervous system disease models.

In this review, we highlight recent advances in the fabrication, characterization and application of miniaturized head-mounted optical neuroimaging systems pioneered by innovative investigators from a wide array of disciplines. We broadly classify these systems into those based on exogenous contrast agents, such as single- and two-photon microscopy systems; and those based on

endogenous contrast mechanisms, such as multispectral or laser speckle contrast imaging systems. Finally, we conclude with a discussion of the strengths and weaknesses of these approaches along with a perspective on the future of this exciting new frontier in neuroimaging.

2.1 Introduction

Imaging the brain has provided unprecedented insights into its functioning as well as disruption of this function due to various neuropathologies. Noninvasive imaging techniques such as functional Magnetic Resonance Imaging (fMRI)[13], Positron Emission Tomography (PET)[14] and Computed Tomography (CT)[15] have been widely used for neuroimaging. However, these clinical or 'human-scale' imaging modalities often lack the resolution to spatially and temporally resolve underlying neuronal processes. Therefore, investigators circumvented this drawback by utilizing pre-clinical animal models in conjunction with imaging methods capable of high spatial and temporal resolution.

The availability of an ever-increasing spectrum of optical contrast agents[16], and technical advances in optics[17, 18], coupled with optogenetic constructs for manipulating neuro-circuitry[18], have resulted in optical neuroimaging becoming the tool of choice for neuroscientific applications. Moreover, these optical neuroimaging techniques permit cellular-scale spatial resolution and millisecond temporal resolution[17].

Much of today's optical neuroimaging is performed using sophisticated optics and cumbersome electronic hardware[19]. The bulky nature of such setups requires the

animal to be anesthetized and restrained stereotactically, greatly limiting the types of experiments that can be performed in vivo and at multiple time points. Additionally, the use of anesthetics has been found to alter the baseline physiology of the brain during in vivo imaging[20]. Therefore, miniaturization of the imaging hardware in conjunction with the ability to image the brains of awake and unanesthetized animals would circumvent these issues.

Recent advances in miniaturized optics and electronic devices[21] paved the way for the “next generation” optoelectronic systems capable of unique real-time, awake optical imaging. **Figure 2.1** shows the evolution of neuroimaging systems from benchtop setups to ‘head-mounted’ platforms. It is not always necessary to miniaturize the entire system. As shown in **Figure 2.1**, depending on the type of experiment, individual elements of the imaging system can be modified to match the required level of animal mobility. This can range from having the animal's head affixed while the animal pedals on a moving ball[22], to systems that allow unrestrained animal mobility[2]. It is worth noting that similar technical advances were also responsible for the development of ‘implantable’ microimagers[23, 24]. These implantable devices are image sensor array chips that have been packaged into ‘ready-to-use’ modules. Recent work has elegantly demonstrated their utility in applications ranging from neural imaging[23, 24] to blood-flow imaging in freely moving rats[25]. However, the focus of the current review is on non-implantable imagers. An excellent recent review by Kerr and Nimmerjahn focused on functional imaging at the cellular level and primarily covered imaging approaches that utilized exogenous contrast agents[26]. In this review, we examine

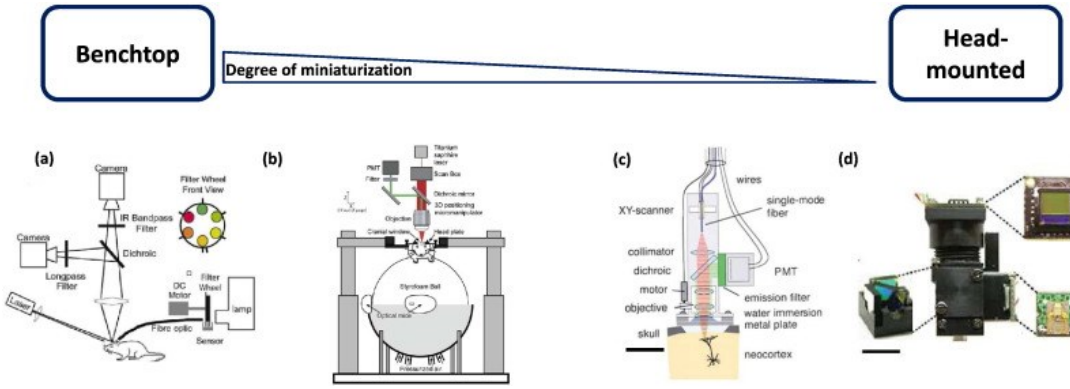

Figure 2.1 Evolution of benchtop to 'head-mounted' neuroimaging systems. The degree of miniaturization increases from (a) to (d). (a) A dual modality benchtop system for simultaneous multispectral imaging and laser speckle contrast imaging in anesthetized animals[27]. (b) Schematic of the system setup for imaging in head-restrained, awake mice[22]. The head-mounted imaging system was modified from a standard two-photon microscope. The head of each mouse was restrained while the animal moved on a treadmill for behavioral testing. (c) Additionally miniaturized fiber-optics-based system[29], in which the photomultiplier tube (PMT) was incorporated into the head piece, wherein the excitation light was still derived from a benchtop system. The head piece was 7.5 cm long (scale bar = 23.5 mm). (d) An integrated head-mounted system[2], using surface mounted LEDs for exciation and a minaturized CMOS sensor for detection (scale bar = 5 mm). This self-contained system enabled experiments involving interactive and natural animal behaviors. All images have been adapted with permission of the publishers.

miniaturized neuroimaging systems that utilize exogenous contrast agents, e.g. wide-field fluorescence imaging[28, 29], two-photon fluorescence imaging[30, 31], as well as those that exploit intrinsic optical properties of biological tissues, e.g. multispectral imaging and blood flow based laser speckle imaging systems[32]. Finally, we discuss the relative advantages and disadvantages of each approach and the exciting prospects of this technology from the micro- (i.e. cellular) to the macro-scale (i.e. whole tissue) for neuroimaging.

2.2 Miniaturized optical systems based on exogenous contrast agents

Optical contrast agents permit visualization of underlying microvasculature[33] as well as functional cellular dynamics such as membrane potentials[34] and intercellular calcium concentrations[35]. Conjugation of fluorescent dyes with genetically encoded biomarkers/target molecules[36], as well as their ability to shift emission spectra in response to biological perturbations[37] has enabled fluorescent imaging to be utilized in a wide range of applications[38, 39]. Although variability in contrast agent delivery or unstable gene expression can affect the emitted fluorescence, an ever increasing array of fluorescent dyes with different excitation spectra, better quantum yields and extinction coefficients has greatly enhanced our ability to simultaneously monitor a multitude of targets and neurophysiologic processes.

Miniaturization of fluorescent microscopy was first attempted by using an optic fiber bundle to relay the emitted fluorescent light as well as the high intensity excitation illumination to and from a standard benchtop system[30]. However, recent technological breakthroughs have enabled additional miniaturization of fluorescent microscopy systems as discussed below. A summary of miniaturized and mobile brain imaging platforms from the recent literature can be found in **Table 2.1.**

Single-photon exogenous contrast microscopes:							
Contrast agent	*Weight*	*Size*	*Field of view*	*In-plane resolution*	*Temporal resolution*	*Application*	*Reference*
VSD (RH1691)	N/A	N/A	3 × 3 mm^2	N/A	2 ms per frame	Whisker barrel cortex imaging	(Ferezou et al., 2006)
Fluorescein-dextran, Ca^{2+} indicator (Oregon green)	1.1 g	N/A	0.07 mm^2	~2.8–3.9 μm	Up to 100 Hz	Blood flow speed/distribution, Ca^{2+} dynamics of Purkinje cells	(Flusberg et al., 2008)
GCaMP3	N/A	N/A	4 mm^2	N/A	N/A	Ca^{2+} imaging of Glia cells	(Cha et al., 2014)
VSD (RH1692)	10 g	N/A	4.88 mm^2	25 μm	Up to 900 Hz	Whisker barrel cortex imaging	(Osman et al., 2012)
Fluorescein-dextran, Ca^{2+} indicator (Oregon green)	1.9 g	N/A	~0.5 mm^2	~2.5 μm	36 Hz or 100 Hz	Blood flow speed/distribution, Ca^{2+} dynamics of Purkinje cells	(Ghosh et al., 2011)
Cy 5.5 dye	0.7 g	1 cm^3	N/A	N/A	N/A	N/A	(O'Sullivan et al., 2013)
Two-photon exogenous contrast microscopes:							
Contrast agent	*Weight*	*Size*	*Field of view*	*Lateral resolution*	*Temporal resolution*	*Application*	*Reference*
Fluorescent-dextran Ca^{2+} indicator (green-1)	25 g	7.5 cm long	N/A	Dendritic spines resolved	N/A	N/A	(Helmchen et al., 2001)
Fluorescein-dextran Rhodamine	N/A	N/A	0.8 mm diameter	Lateral: 3.2 μm Axial: 20 μm	N/A	N/A	(Göbel et al., 2004)
Fluorescein-dextran	2.9 g	2 × 1.9 × 1.1 cm^3	N/A	Lateral: 1.29 ± 0.05 μm Axial: 10.3 ± 0.3 μm	1–15 Hz	Blood flow analysis	(Piyawattanametha et al., 2009)
GAD67-GFP	~1.5 g	N/A	300 μm diameter	Lateral: 3.2 ± 0.4 μm Axial 5.1 ± 1 μm	N/A	N/A	(Engelbrecht et al., 2010)
Sulforhodamine 101 & Ca^{2+} indicator	5.5 g	N/A	N/A	Single soma resolved	90 ms per frame	Ca^{2+} dynamics from visual stimuli	(Sawinski et al., 2009)
Ca^{2+} indicator	0.6 g	N/A	Up to 200 μm	Lateral: 0.98 ± 0.09 μm Axial: 7.68 ± 1.3 μm	25 Hz	Ca^{2+} dynamics of Purkinje cells	(Engelbrecht et al., 2008)
Endogenous contrast microscopes:							
Contrast agent	*Weight*	*Size*	*Field of view*	*Lateral resolution*	*Temporal resolution*	*Application*	*Reference*
LSCI	~20 g	3.1 cm long	N/A	16 lp/mm	N/A	Vasculature/relative blood flow	(Miao et al., 2011)
LSCI & multispectral	1.5 g	N/A	N/A	5.5 μm	N/A	Cortical spreading depression	(Liu et al., 2013)
LSCI	~7 g	5 cm^3	3.5 × 3.3 mm	N/A	6 Hz	Vasculature/relative blood flow	(Senarathna et al., 2012)

Table 2.1 Summary of miniaturized and mobile brain imaging systems.

2.2.1 Single-photon microscopy systems

Since single-photon microscopy does not need an expensive near-infrared laser or a laser scanning mechanism, it is less complicated and more affordable than two-photon microscopy. These advantages also make it well-suited for miniaturized optical neuroimaging applications. The absence of a laser scanning mechanism endows single-photon microscopy with a high temporal resolution that is suitable for imaging dynamic neurobiological phenomena. However,

single-photon systems can only acquire two dimensional images and the use of wide-field excitation increases the risk of photo-bleaching the sample.

Ferezou et al. were one of the first to report in vivo fluorescent imaging in freely moving animals[28]. In their system, a customized multi-fiber array (**Figure 2.2a**) placed in direct contact with the rat whisker barrel cortex relayed emission and excitation light to and from a standard benchtop epifluorescence imaging system. A voltage sensitive dye (RH1691) was employed for functional imaging of the barrel cortex following whisker stimulation. The dye primarily stained layer 2/3 sensory neurons. The system had a temporal resolution of 2 ms and covered a 3 mm × 3 mm field of view (FOV). Spatial resolution was limited by the size of individual fibers in the fiber optic bundle as well as by the low numerical aperture due to the absence of an objective lens at the specimen–optical fiber interface. While the exact spatial resolution of the system was not reported, the authors could successfully visualize the barrel cortex at sub-columnar resolution. Images from the fiber optic microscope were compared with those from a conventional fluorescent imaging setup, and no significant differences in peak fluorescence amplitude, duration or spatial extent of the sensory response to whisker stimulation were observed. Furthermore, the sensory response to whisker stimulation in rats anesthetized with isoflurane was compared to that of awake rats. The authors showed that awake animals exhibited a response longer in duration and larger in spatial extent than their anesthetized counterparts [28].

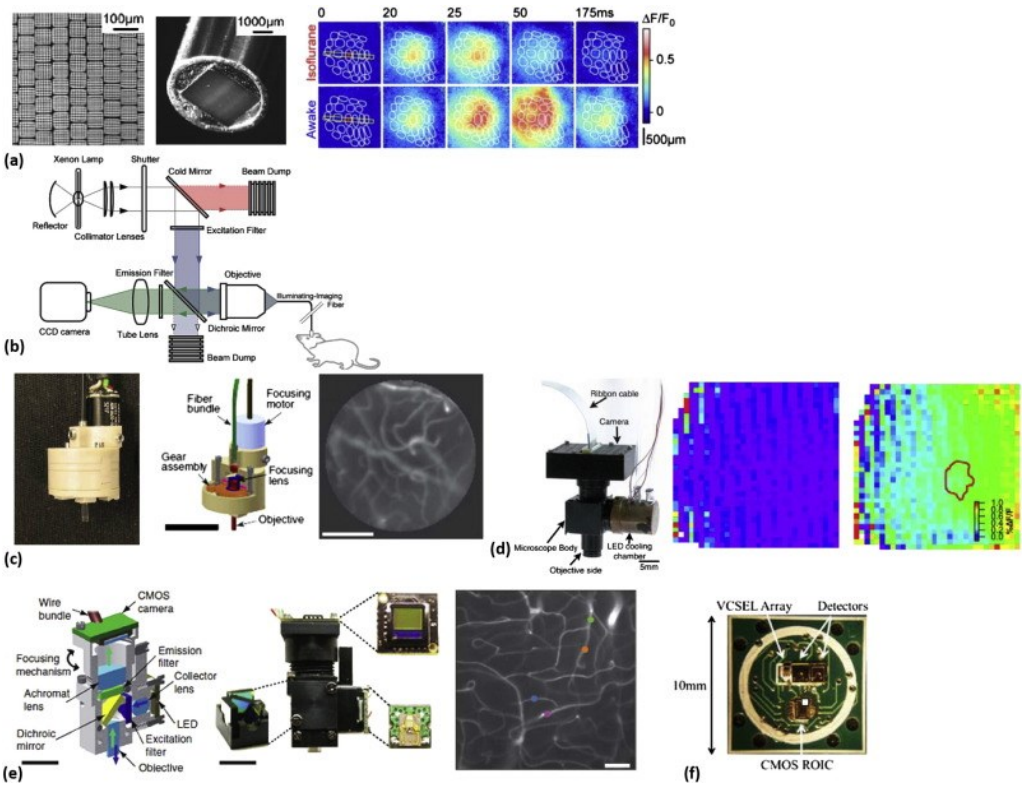

Figure 2.2 Miniaturized single-photon optical systems. (a) Images of the custom manufactured fiber optic bundle from[27], based on wound image bundle technology (Schott Fiber Optics, Southbridge MA). The left panel shows a high-maginification image of the fiber bundle tips: each group consisted of 6 × 6 fibers; each fiber had 8 μm cores and a resulting numerical aperture of 0.6. The middle panel shows an image of the fiber bundle (diameter 5 mm) that was in direct contact with the rat cortex. The right panel shows the comparison of cortical responses to C2 whisker perturbation imaged by voltage sensitive dye (VSD) between an isoflurane anesthetized and an awake mouse. VSD analysis on C2 barrel column revealed that the duration of the response was much longer in the awake mouse. (b) Single-fiber system schematic for side-on imaging of pyramidal cells in layer 5 of the rat neocortex[40]. The fiber bundle was used to transmit excitation light and collect fluorescence signals from a standard benchtop system. (c) Fiber optic single-photon microscope from Flusberg et al.[28], showing the head mount comprising of focusing optics, the fiber bundle and focusing motor. The head piece weighed 1.1 g, and the

system had a frame rate of less than 100 Hz. The two GRIN objective lenses of different focal lengths enabled deep (6.2 mm) and superficial tissue (1.4 mm) imaging. The right panel shows the image of neocortical vasculature from an awake freely moving mouse (Scale bar = 100 μm). (d) A self-contained fluorescence microscope[43], consisting of a LED light source, CMOS image sensor, focusing optics and exciatation/emission filters. The microscope was designed for high speed imaging and detecting small changes (< 1% ΔF/F) in fluorescence signals. The middle panel shows a baseline %ΔF/F image of the mouse barrel cortex labeled with VSD RH1691 (averaged from 9–12 ms before whisker deflection). The right panel shows an average %ΔF/F image in the same FOV 9–12 ms after the onset of stimulation (Osman et al., 2012). (e) The self-contained one-photon[2], light source (LED) and image sensor (CMOS camera) were mounted on the head piece (weight 1.9 g). The electrical signal was transmitted via the wire bundle to a FPGA, for both LED control and image acquisition. Microvasculature of freely behaving mouse was acquired after injection of fluorescein-dextran. The image is the standard deviation from 10 second acquisition, to emphasize vasculature. (Scale bar = 50 μm) (f) Photograph of the VCSEL–CMOS sensor reported by O'Sullivan et al.[45]. The custom PCB with bonded chips, consists of multiple VCSEL excitation sources, two GaAs photodiodes and a CMOS read-out integrated circuit (ROIC). All images have been adapted with the permission of the publishers.

Murayama et al.[40] reported a single-photon fiber optic system for recording dendritic calcium signals (**Figure 2.2b**). To illuminate and collect light locally from the distal dendrites of cortical layer 5 neurons, an optic fiber was directly inserted into layer 5 of the rat's brain. To acquire different views of the dendrites, two optical setups were employed: the first included a one-fiber system for a side-on view; and the second was a two-fiber system for imaging above the cortex. The one-fiber system was tested on freely moving rats. After injecting a calcium-sensitive dye (Oregon Green 488 BAPTA-1), calcium signals were recorded from layer 5 neurons in stationary and free moving states, as well as during whisker

stimulation. The amplitude of the calcium signals was observed to vary with the state of the animals. Furthermore, the authors simulated the effects of motion on their image acquisition by using a bench top stirrer assembly to vibrate an anesthetized rat while the microscope continuously acquired images. No significant changes were observed in the fluorescent signal from calcium transients. A later publication using the same system investigated dendritic calcium changes in layer 5 pyramidal cells of the somatosensory cortex in rats following sensory stimulation (Murayama et al., 2009). Their results showed that the strength of sensory stimulation was encoded in the calcium response of local layer 5 pyramidal cells in a graded manner.

Flusberg et al. [29] reported a miniaturized singe-photon microscope for cellular-level imaging at frame rates up to 100 Hz. The optical components of the microscope consisted of a compact coupling assembly, focusing mechanism and two separate objective lenses. The head-mounted microscope weighed only 1.4 g and had a spatial footprint on the scale of a centimeter (**Figure 2.2c**). This ensured that the microscope could be easily supported by an adult mouse. The head piece was then connected to a standard benchtop fluorescent imaging system. Dual objective lenses ensured that both superficial and deep tissue could be imaged. Limitations in packing density and number of individual fibers in the optic fiber bundle restricted the lateral resolution and FOV to ~ 2.8–3.9 μm and ~ 240–370 μm, respectively. Its 75 Hz data acquisition rate made it possible to discern the movement of individual erythrocytes within blood vessels. Tests on freely moving mice revealed that motion artifacts were limited to less than 2 μm

of lateral displacement. The microscope was used to record surface blood flow in the mouse neocortex and in the CA1 region of the hippocampus. Using temporal cross-correlation analysis, the authors demonstrated that blood flow velocities varied greatly among capillaries, venules and arterioles. The microscope was also used to compare Purkinje cell dendritic Ca2+ dynamics during the anesthetized and mobile states. Purkinje cells exhibited larger Ca2+ spike rates during locomotion than at rest. Additionally, correlation analysis of Ca2+ spiking between pairs of Purkinje cells revealed larger correlation coefficients during active movements than at rest.

Cha et al.[41] designed a fiber-optic fluorescence microscope that used an objective focusing lens consisting of two symmetric aspheric lenses covering a ~ 4 mm2 FOV. Their fiber optic bundle interfaced with a standard benchtop based fluorescence system. In vitro imaging demonstrated that this system was capable of resolving astrocytes and pyramidal cells in a mouse brain section, and image quality was comparable to that of a conventional fluorescence microscope. In vivo experiments with this system were conducted on head-restrained, awake mice placed on a treadmill. Using this microscope, the authors were able to demonstrate that Bergmann glia in the cerebellum showed larger amplitude of Ca2+ signals during locomotion than when the animal was at rest.

The ‘next-generation’ neuroimaging systems were fully miniaturized by using surface mount light emitting diodes (LEDs) for excitation illumination and minute (~ 3 mm × 3 mm) CMOS image sensors for image acquisition. These miniaturized microscopes enabled a transformation of the experimental paradigm

from one in which restrained animals were imaged, to one in which interacting or naturally behaving animals could be imaged.

Osman et al.[42, 43] and Park et al.[44] designed a neuroimaging system with a miniaturized illumination source, focusing optics and image sensor (**Figure 2.2d**). This microscope featured a frame rate of 500 frames per second (fps) and a sensitivity of 0.1% of the initial fluorescent signal (0.1% ΔF/F). Weighing 10 g, the system had a FOV of ~ 4.8 mm2, lateral resolution of 25 μm and a 1.8 magnification ratio. Without a physical shutter, the system required very stable illumination to precisely control the exposure time. Therefore, the LED output was actively controlled by a photodiode and microcontroller to maintain light intensity within 0.2% deviation of its mean intensity. Small changes (< 1% ΔF/F) in barrel cortical fluorescence signals due to whisker stimulation were detectable using a voltage sensitive dye (RH1691). As reported in Osman et al. (2012), the resulting signal quality was comparable to that of a benchtop fluorescent microscope equipped with a Red-Shirt-Imaging camera (Decatur, GA). However, this microscope was not a fully miniaturized prototype. The image acquisition controller was a non-miniaturized field-programmable gate array (FPGA) assembly with an electric wire bundle connected to the head piece. The microscope's use is limited because the tether's rigidity could affect the animal's mobility in certain kinds of functional experiments.

Ghosh et al.[2] designed a similarly miniaturized fluorescence microscope (**Figure 2.2e**). Weighing only 1.9 g, it could be easily carried by an adult mouse. A maximum FOV of 600 × 800 μm was reported while supporting a magnification

ratio of 5.0 and a lateral resolution of ~ 2.5 μm. The microscope was capable of high-speed cellular level imaging up to a frame rate of 100 Hz while covering a FOV of ~ 0.5 mm2. Using this system, synaptic activation via calcium tracking in up to 206 Purkinje neurons from nine cerebellar microzones was reported. The microscope was first used to study the microcirculation during mobile and rest states of mice. The authors reported an increase in erythrocyte flow speeds when the animals transitioned from rest to locomotion states. Additional studies were focused on differentiating synaptic dynamics of freely moving mice during different behavioral states using a fluorescent calcium indicator. The authors showed that mean spike rates increased as the animal transitioned from rest to groom to locomotion states, respectively[2]. When compared to the fiber-optic-based microscope previously reported by the same group[29], the new microscope showed better performance in terms of optical resolution, fluorescence signal quality and system robustness. The FOV of the fiber-bundle-based microscope was restricted by the maximum diameter and bending radius of the bundle, while the FOV in this new microscope was only limited by sensor size and the focusing optics. Additionally, the fiber bundle microscope exhibited drastic attenuation of the transmitted fluorescent light due to bending and light absorption of the fiber. The fluorescence detected by the sensor increased from ~ 20% to 95% while a ~ 700% greater FOV was achieved. No realignment of the optics was necessary between imaging sessions, and the imaging duration could be extended up to 45 min. Observed motion artifacts were limited to less than 1 μm even when imaging running animals.

O'Sullivan et al.[45] reported the fabrication of a miniature, integrated semiconductor-based fluorescence sensor, designed for detecting fluorophores and tumor-targeted molecular probes (**Figure 2.2f**). The system consisted of multiple vertical-cavity surface-emitting laser (VCSEL) dies as the excitation source, GaAs photodiodes as two point detectors, and a CMOS (complementary metal oxide semiconductor) ROIC (read-out integrated circuit) for reading out the data, mounted on a custom printed circuit board (PCB). A standard 18-pin connector was employed for data transmission. The system was extremely lightweight (~ 0.7 g) with a small footprint (~ 1 cm3). VCSEL excitation wavelengths were optimized for the Cy 5.5 dye, and the emission filter was directly coated on to the custom-made image sensor. The onboard photocurrent ranged from 5 pA to 15 nA and was amplified and digitized using the ROIC for subsequent data acquisition. When the system was tested on freely moving mice, the authors reported an increase of ~ 500 pA in the photocurrent following injection of Cy 5.5 fluorescence dye. This miniaturized system required precise positioning and fixation to the targeted object, which made it difficult to use on soft tissue or when imaging small targets[45].

2.2.2 Two-photon microscopy systems

Two-photon microscopy (2 PM) uses ultra-short pulses of a long wavelength laser to scan biological tissue in three dimensional space, creating a depth resolved image stack. This approach excites only the voxel being imaged, thereby minimizing photo-toxicity. Additionally, the use of a longer wavelength excitation light reduces scattering in biological tissues, enabling deeper imaging

depths. Nonetheless, laser scanning impacts the acquisition frame rate, enabling only relatively slow phenomena to be imaged. Also, the laser scanning pattern can be distorted by the motion of awake, unrestrained animals. Due to the high power and temporal modulation accuracy required of the laser, miniaturized 2 PM systems utilize a standard benchtop 2 PM system retrofitted with optical fiber bundle and focusing optics, to deliver excitation and collect the emitted light from the freely moving animal.

Helmechen et al. reported the first miniaturized head-mounted two photon microscope[30]. The head piece consisted of a single-mode optical fiber for excitation, a miniature scanning device, microscope optics and a miniature photo multiplier tube (PMT) (**Figure 2.3a**). Two-dimensional scanning was realized by resonant scanning in a Lissajous pattern. A line scanning mode was also available for faster imaging. The microscope was 7.5 cm high, 25 g in weight and could be supported by an adult rat. In vivo imaging on anesthetized rats injected with a dextran dye showed surface blood vessels and the underlying capillary network. The maximum imaging depth was 250 μm. Furthermore, imaging on anesthetized rats injected with a calcium indicator (calcium green-1) resolved dendritic processes in layer 2/3 neurons. Testing this microscope on freely moving animals, the authors determined that rapid turning of the head and sudden contact with a wall induced noticeable motion artifacts in the acquired fluorescence images

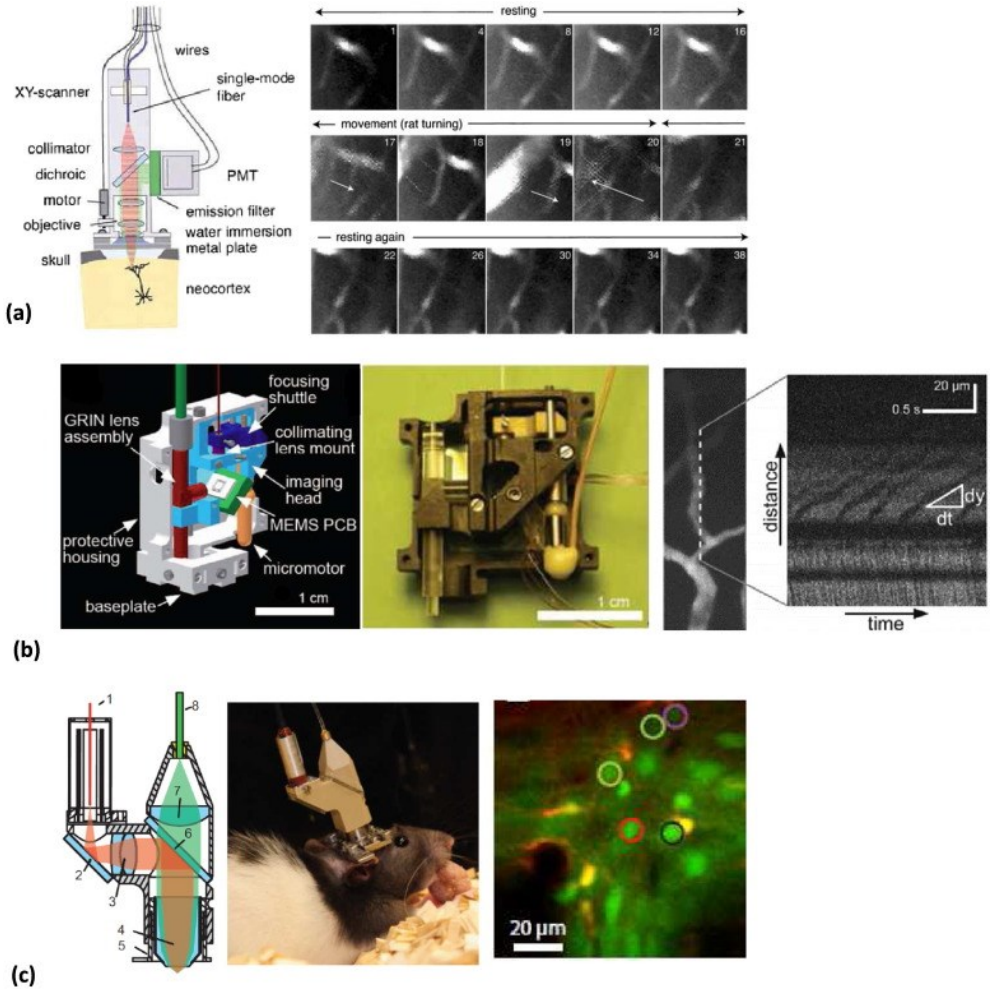

Figure 2.3 Miniaturized two-photon optical systems. (a) Left panel: The first reported head-mounted two-photon microscope[29]. Near infrared laser excitation was coupled to a single mode fiber, collimated and focused by a water-immersion objective to the neocortex. Fluorescence signal collection was achieved by a PMT. Right panel: Sample images from an awake rat labeled with fluorescein-dextran (0.5 s frame duration). Motion caused the FOV to shift from frame 17 to 20 (indicated by white arrows). (b) Schematic (left) and photograph (middle) of the two-photon microscope based on a MEMS scanning mirror[47]. The microscope weighed 2.9 g, excitation pulse and fluorescence collection were separated by using two different types of optic fibers, which enhanced the SNR of the detected fluorescence signals. Right panel: Images of neocortical capillaries from an anesthetized adult mouse injected with fluorescein isothiocyanate-dextran dye.

Line scanning mode (shown in the enlarged view on the right) allowed the microscope to track individual erythrocytes flowing parallel to the line scanning direction. (c) Left panel: Schematic of the two-photon microscope, made up of: 1. single-mode excitation fiber; 2 folding mirror; 3, tube lens; 4, objective; 5, focusing flange; 6, beam splitter; 7, collimation lens; and 8, multi-mode collection fiber. Middle panel: Photograph of a rat with the head-mounted microscope[48]; Right panel: Overlay of in vivo images acquired using two fluorescent dyes: SRS 101 that labels astrocytes (red channel) and the calcium indicator OGB-1 that labels neurons (green channel), in a rat's visual cortex. The colored circles indicate the neurons and the astrocyte from which signals were analyzed in response to visual stimulation.

A two-photon microscope with two objective gradient-index (GRIN) lenses for miniaturized focusing was built by Göbel et al.[46]. Pre-compensation for the broadening of excitation light within the optic fiber was achieved by pre-chirping the laser pulses. Lateral and axial resolutions of 3.2 μm and 20 μm, respectively, were achieved. The pixelated image was smoothed with a Gaussian filter to compensate for the 1 μm spacing between individual fibers in the optic fiber bundle, which also reduced image contrast. As proof of concept for the device, in vivo imaging of fluorescein-injected, anesthetized rats was performed to visualize blood vessels.

Piyawattanametha et al.[47] reported a portable 2 PM microscope based on a microelectromechanical systems (MEMS) laser scanning mirror (**Figure 2.3b**). The system weighed 2.9 g. Moreover, the implantation of the MEMS scanner made the 2 PM system more compact, i.e. 2 cm × 1.9 cm × 1.1 cm in size. Separate optical fibers for fluorescence collection and excitation pulse delivery were utilized. The system had transverse and axial resolutions of 1.29 ± 0.05 μm

and 10.3 ± 0.3 μm, respectively, with a maximum FOV of 295 × 100 μm and was used to image neocortical capillaries in mice injected with fluorescein dye. In the line scanning mode, individual erythrocytes inside blood vessels could be tracked in an anesthetized animal.

Sawinski et al.[48] reported a miniaturized head-mounted 2 PM system for recording Ca2 + transients from the somata of layer 2/3 neurons in the visual cortex of awake, freely moving rats (**Figure 2.3c**). As described by the authors, 'a custom designed water-immersion lens and a leveraged non-resonant fiber scanner were employed, providing greater control over the scan pattern than resonant scanning'[48]. Their multi-lens setup provided higher excitation and detection numerical apertures (NA) compared to using a single GRIN lens. Besides neuronal activity resulting from visual stimuli, bending of the optical fiber also caused fluctuations in the detected fluorescence signals. To counteract this, two fluorescent dyes, a green calcium indicator (Oregon green BAPTA-1, OGB1) and sulforhodamine 101 (SR101) were employed. Since SR101 fluorescence was not related to neuronal activity, it was used to normalize the signal from the green fluorescent calcium indicator. They conducted one of the first in vivo experiments on freely moving animals on a semicircular track. They placed three monitors with different visual stimuli at the apex and the ends of the track. The experiment was conducted in the dark except for light stimulation from the monitors. Synchronized infrared videos were recorded during the experiment to investigate the relationship between animal movement and calcium indicator signals. A significant increase in calcium transients was observed when the

animal swept its gaze across the visual stimuli. It should be noted that motion artifacts were observed during chewing and head movement of the animals. Of these, lateral displacements were corrected by an automated algorithm as described in[49].

Barretto et al.[50] designed a micro-lens-based 2 PM imager. By combing a GRIN lens with a plano-convex lens, their setup was corrected for aberration and had a higher numerical aperture than just using the GRIN lens by itself. In vivo images of GFP-expressing pyramidal cells in region CA1 of the mouse hippocampus showed better resolution than images acquired using the GRIN lens alone. Finally, Helmchen et al. provide a detailed protocol for investigators interested in designing their own bespoke two-photon microscopy based systems for in vivo imaging in freely moving animals in [51]. The dissemination of such hardware 'recipes' using commercially available components should make imaging in awake animals more widespread.

The feasibility of other approaches, such as diffuse optical tomography[52], light-sheet-based microscopy[53] and two-photon microendoscopes[29, 54] has also been demonstrated in freely moving animals. Besides the abovementioned applications, head-mounted microscopes have also been used for studying cortical calcium waves in newborn mice[55], and for imaging hippocampal cells during virtual navigation tasks[22, 56].

2.3 Miniaturized optical systems based on endogenous contrast

The earliest form of intrinsic contrast based optical imaging was performed using multispectral imaging, which exploits the spectral properties of oxygenated and deoxygenated hemoglobin to visualize the relative oxygen saturation in biological tissue[57]. Recently, laser speckle contrast imaging (LSCI), that relies on flowing blood for image contrast[58], has also been miniaturized for freely moving animal experiments (**Table 2.1**).

2.3.1 Multispectral imaging system

Multispectral imaging has a long and established history in neuroscience[59]. However, it lacks complementary contrast from other tissue structures because it does not rely on any exogenous contrast agents, but rather on the spectrally dependent absorption properties of hemoglobin moieties[60]. Nonetheless, miniaturized multispectral imaging provides a convenient way to observe tissue oxygenation changes in the brain.

Murari et al.[61, 62] designed a microscope with the potential for multi-modality neuroimaging. This system occupied ~ 4 cm3 and weighed 5.4 g, while incorporating a highly sensitive custom-made CMOS camera. Cortical blood vessels 15–20 μm diameter could be visualized using this system. In vivo experiments on rats using a green LED light source demonstrated a reflectance change between the active state and rest state. Tests on fluorescence, LSCI and

multispectral imaging, demonstrated the feasibility of developing a multi-modality miniaturized microscope for neuroimaging applications.

2.3.2 Laser speckle contrast imaging systems

Laser speckle contrast imaging (LSCI) relies on the statistical properties of coherent light scattered by red blood cells (RBCs) moving inside perfused blood vessels. A higher blood flow velocity generates a greater speckle blur and a lower speckle contrast and vice versa. This mechanism enables LSCI to assess relative blood flow changes as well as delineate microvascular structure from background tissue with a high contrast-to-noise ratio[12]. However, LSCI typically requires an image stack to compute relative blood flow maps, thereby limiting its intrinsic temporal resolution.

Miao et al.[63] designed a head-mounted microscope for laser speckle contrast imaging (**Figure 2.4a**). The microscope was ~ 20 g in weight and 3.1 cm in height. This head-mounted system consisted of a miniature macrolens system, image sensor, optical fiber bundle and circuits. The spatial resolution achievable was 16 lp/mm with less than 2% distortion. To eliminate motion artifacts, registered laser speckle contrast analysis (rLASCA) was applied to the raw speckle data, wherein each image from the image stack was aligned with the first image. While the rat was free moving, blood vessels approximately 4 pixels or ~ 50 μm in diameter could be identified (**Figure 2.4a**). This spatial resolution was comparable to that of standard benchtop laser speckle imaging systems and suitable for studying the cerebral blood flow (CBF) of major vessels under

different physiological conditions[63]. Liu et al.[32] designed a dual-modality LSCI/multispectral microscope, also extendable for fluorescence imaging (**Figure 2.4b**). The multi-modal microscope weighed 1.5 g, and the internal optical components were adjustable, providing different magnification ratios and FOVs. They conducted an extensive study on cortical spreading depression (CSD) in freely moving and anesthetized animals. Hemodynamic parameters were calculated from simultaneously acquired LSCI and dual-wavelength multispectral imaging data. The authors demonstrated that there was a significant difference in CSD propagation latencies between anesthetized and awake animals (Fig. 4b). CSD in isoflurane-anesthetized rats was significantly longer in duration, and agreed with previous studies demonstrating that anesthetics extend CSD duration and reduce CSD frequency[64]. Senarathna et al.[65, 66] reported the development of a miniaturized LSCI microscope weighing 7 g and occupying less than 5 cm3 (**Figure 2.4c**). The system consisted of a laser diode (tri-wavelength), focusing optics, CMOS sensor, with control circuits housed in a backpack. The tetherless setup made the microscope suitable for behavioral tests in freely moving rodents. LSCI images could be computed following acquisition of 240 raw speckle images. By converting speckle contrast to the correlation time of blood flow[67], relative CBF maps were generated (**Figure 2.4c**). As reported in Senarathna et al.[66], image quality degraded an hour after implantation. The authors concluded that this might be attributable to the refractive index matching material (i.e. mineral oil) gradually evaporating and the thinned skull optical window preparation eventually drying out. Also the use of a rolling shutter

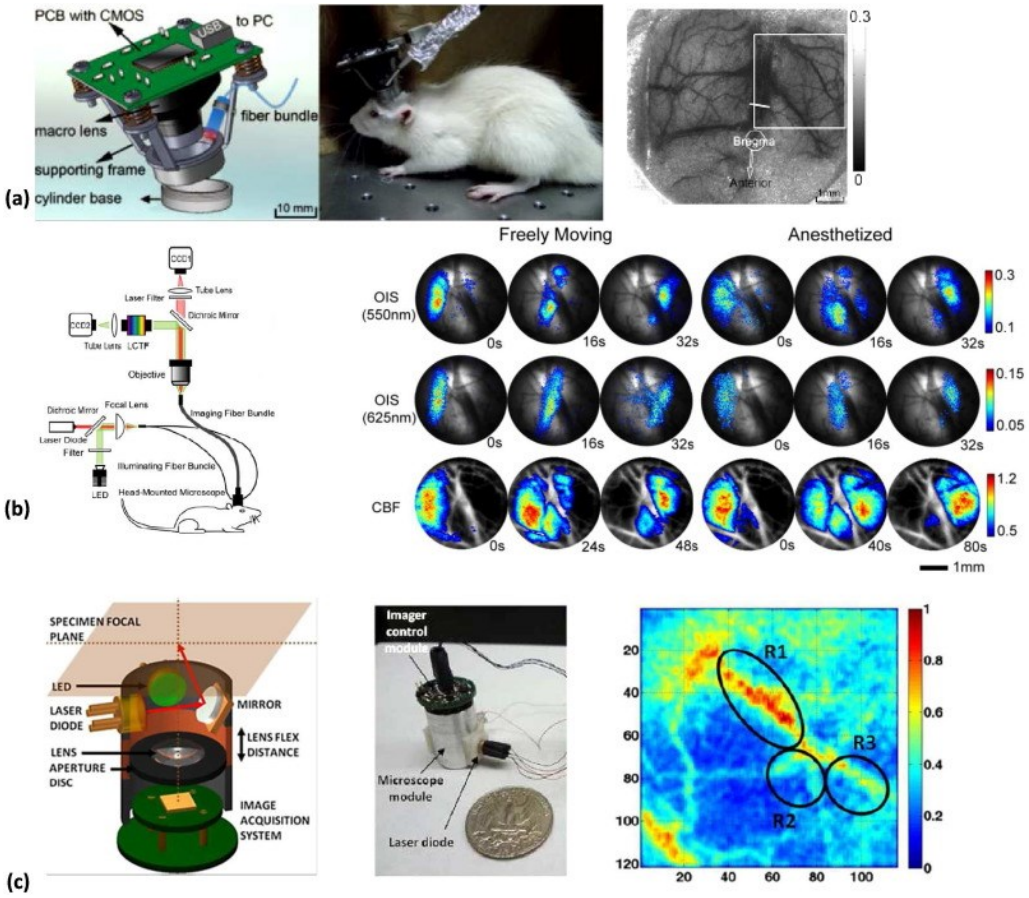

Figure 2.4 Miniaturized optical systems that utilize endogenous contrast agents. (a) Left panel: Schematic of a fiber-optics-based laser speckle imaging microscope. The illumination was fiber-coupled from a benchtop laser source and the camera chip was incorporated within the head piece. Middle panel: A rat with the head-mounted microscope that was ~ 20 g in weight and 3.1 cm in height. Right panel: In vivo laser speckle contrast image from a freely moving rat after co-registration[63]. The image shows the vascular network in the rat cortex over a 7 mm × 7 mm FOV. (b) Left panel: Schematic of dual-modal fiber-optic-based microscope designed by Liu et al. (2013). The system consisted of three parts: a fiber-coupled dual illumination source, a head-mounted microscope and two CCD cameras system for dual modality acquisition. Right panel: Spatio-temporal evolution of hemodynamic changes from a cortical spreading depression (CSD) model illustrating the difference between anesthetized

and awake states[31]. (c) Schematic (left panel) and photograph (middle panel) of a self-contained laser speckle imaging microscope in which light from a VCSEL is reflected by a side mirror to accommodate different focal planes. The speckle signals were focused onto a custom made CMOS sensor by a single lens[66]. Right panel: Relative blood flow map derived from speckle contrast images acquired using the microscope (laser wavelength λ = 795 nm) from the rat cortex over a ~ 1.85 mm × 2 mm FOV. The higher blood flow velocity of R1 indicates that R2 and R3 are downstream of R1 and that blood flow from R1 is branching off into R2 and R3.

technique for exposure time control together with a relatively low frame rate of ~ 6 fps, resulted in long exposure times that averaged out some of the speckle contrast. The spatial resolution of the system was 20 μm, which was the pixel size of the image sensor. Higher spatial resolution could be achieved by replacing it with a smaller pixel size CMOS sensor.

2.4 Discussion

Miniaturized brain imaging systems, while having the advantages of portability, size, and multimodality neuroimaging in awake/unrestrained animals are prone to several shortcomings. Therefore, the decision to utilize such an imaging system instead of a benchtop setup should be based on a balance of its strengths and weaknesses.

A major concern with miniaturized neuroimaging systems is the additional weight it imposes on the animal. While a benchtop system tethered to an animal via an optical fiber bundle imposes minimal additional weight, a fully miniaturized system requires the entire weight of the imaging system be borne by the animal.

Hence, it is vital that such imaging systems are designed with critical weight limits for the applications under consideration. A similar argument applies to the spatial footprint of the device attached to the animal's head, including the total height and size of the instrumentation. Use of a larger species of animals, e.g. rats versus mice, might partially obviate this concern. Nonetheless, it is crucial that experimental protocols involving miniaturized, head-mounted microscopes clearly establish that the animal behavior under study is not significantly affected by the implanted or mounted neuroimaging system[31].

Increased motion artifacts are another concern with studies in freely moving, unanesthetized animals. Beyond respiration and cardiac motion artifacts that are seen in benchtop imaging, miniaturized imaging platforms are susceptible to motion caused by whole-body movement as well as relative motion between the head-mounted microscope and the animal's body. Some imaging modalities are more sensitive to motion than others, e.g. 2 PM suffers more from motion artifacts than wide-field fluorescence microscopy. Different image registration and motion removal algorithms can be employed to enhance image quality[68].

A frequently overlooked aspect of miniaturized imaging systems is the challenge of building them from high-performance optical and electronic components in view of their size, weight and power constraints. Therefore, due to limitations in current hardware and optical component fabrication, compact imaging systems usually offer ‘bare-bones’ imaging capabilities that are customized to a given experimental paradigm. In doing so, such systems lack the imaging precision, accuracy and flexibility of conventional benchtop systems. For example, in

miniaturized LSCI systems, the VCSEL laser source may emit laser light that is not very coherent, thereby degrading speckle contrast. While a benchtop setup can be easily focused, the magnification changed and multiple wavelengths imaged conveniently, a miniaturized neuroimaging system has limited focusing ability and a fixed magnification level and imaging different wavelengths is often challenging. Therefore, flexibility and precision need to be considered before choosing a miniaturized neuroimaging system over a conventional benchtop imaging system.

An important aspect of imaging in awake, freely moving animals is correlating their behavior with their neural responses. Different types of monitoring tools have been employed to monitor animal activity for various applications. Typically, synchronized videos are recorded during experiments measuring neural response to document the animal's behavior. In Sawinski et al.[31], the positions of four infrared LEDs attached to the microscope were used to determine animal's movements and orientation of its head. By correlating the animal's behavior with visual stimuli presented on monitors in its field of view, the authors were able to study the relationship between visual perturbations and concurrently recorded calcium signals. In Dombeck et al.[22], running speeds were measured by the rotation of a spherical treadmill on which the animal was placed and infrared videos were recorded to catalog grooming and whisking behavior. The changes in the fluorescence trace of neurons labeled with calcium sensitive dye during running behavior were analyzed, with a significant fraction of neurons exhibiting a

strong running correlation. As reported by the authors, transients of some neurons mimicked the time course of running speed.

While in their simplest form many head mounted optical microscopes have utilized a single imaging modality, integrated systems with two imaging modalities have begun to emerge. Most commonly, multispectral imaging, given its relative simplicity in implementation, is combined with another modality such as fluorescent or speckle imaging[32, 62, 69]. Such systems provide scientists access to a multitude of biological variables enabling them to obtain a more holistic view of the neurobiology of awake and freely moving animals. Moving forward, given the need for acquiring multi-parametric data, the development of miniaturized systems with more than two imaging modalities may become commonplace.

Combining optical imaging with other neurobiological data such as electrophysiology[70], biochemical recordings etc., could lead to a multimodality system for studying the brains of freely moving animals. For example, visualizing cellular calcium dynamics with fluorescent imaging while simultaneously monitoring electrophysiology with a transparent electrocorticographic (ECoG) sensor array[71], could herald a new era of neurobiological investigation. Or one could envision experiments involving functional neuromodulation via electrical or optogenetic stimulation to assess interactions between stimulation and neuroimaging.

2.5 Conclusions and future directions

In the past decade, traditional benchtop based microscopy of anesthetized and constrained animals has slowly made way to neuroimaging in freely moving animals. Technological innovations in electronic hardware, miniaturized optics and computing power have converged to make this tremendous advance possible. This has brought about a paradigm shift in neuroscience, enabling scientific investigations geared towards uncovering natural brain function and dysfunction due to disease. Since optical imaging is relatively simple to operate in contrast to other imaging modalities such as ultrasound, MRI etc., the construction of miniaturized neuroimaging platforms has experienced an exponential growth (**Table 2.1**).

Early instrumentation for brain imaging in freely moving animals involved a standard benchtop microscope coupled to an optical fiber bundle that attached to an optical window over the animal's intact brain. The next generation of neuroimaging systems utilized optics inserted into the animal's head-mount, while keeping the rest of the microscope assembly unchanged. However, in the latest generation of neuroimaging systems, the development of miniaturized light sources and sensitive CMOS image sensors within the head-mounted microscope is making the need for optical fiber bundles less critical. Nonetheless, such imaging systems still require wires to connect the head-mounted instrumentation with advanced control circuitry on the benchtop, thus tethering the animal. Fully compact microscope systems that utilize miniature control and

storage electronics encased in a backpack worn by the animal have begun to emerge, enabling truly tetherless animal brain imaging. With impending improvements in electronic and optical design, supported by the availability of sophisticated computer aided design (CAD) and rapid prototyping tools, fully mobile and ultra-compact head mounted systems can be envisioned. These will increase user convenience and make possible a range of experiments that were previously unfeasible due to the presence of tethers. Examples include behavioral experiments involving complex maze structures as well as group studies wherein brain function of multiple freely interacting animals can be simultaneously tracked as an ensemble.

Future applications of miniaturized microscopes need not be limited to conventional neuroscience applications, but could include imaging in a wide array of preclinical disease models. For example, one could envisage the use of head mounted optical microscopes for 'life-time' imaging of brain tumor progression, or sudden onset/termination of seizures; imaging of neurovascular coupling, imaging neural plasticity or continuous imaging of the etiology of stroke. In summary, miniaturized optical head-mounted imaging systems have progressed considerably from their benchtop antecedents. We envision a future in which the use of such portable, user-friendly systems will become commonplace in neuroscience laboratories alongside advances in optogenetics and high-throughput electrophysiology. It is our belief that miniaturized optical neuroimaging in unrestrained animals will be a critical ingredient of the next-wave

of breakthroughs in the neurosciences and investigations of brain-related pathologies.

2.6 Acknowledgements

This research was funded by NCI grant no. 1R21CA175784-01

Chapter 3 **A Miniature Microscope for Multi-Contrast Optical Neuroimaging in Awake Animals**

Multi-contrast neuroimaging permits the simultaneous interrogation of multiple neurophysiologic variables, enabling a more complete understanding of brain function. Traditionally, this has required benchtop-based, custom-built imaging systems that often preclude *in vivo* neuroimaging of awake animals. To circumvent this issue, we designed and built a 'plug and play' miniaturized microscope that fits on a rodent's head and combines three optical contrast mechanisms: fluorescence (FL), hemoglobin intrinsic optical signals (IOS) and laser speckle contrast (LSC) and. This multi-contrast microscope weighs 9 g, occupies 5 cm^3 and can image *in vivo* neural activity and cortical hemodynamics in an awake rodent over 3×3 mm^2 at 5 μm resolution. We demonstrate its utility by: (i) imaging neuronal and hemodynamic responses to auditory stimulation, (ii) performing wide-area functional mapping analogous to classic fMRI, and (iii) characterizing hemodynamic and electrophysiological changes that accompany arousal from anesthesia. These broad range of applications demonstrate that this microscope provides a portable, miniature platform for multi-contrast neuroimaging in awake animals. Its affordability, customizability and expandability open up new vistas for *in vivo* brain experimentation.

3.1 Introduction

Multi-contrast optical neuroimaging[6, 72, 73] enables one to simultaneously interrogate multiple neurophysiologic variables, a feat that was not possible with traditional single-contrast optical imaging techniques[74-76]. Consequently, neuroscientists can now visualize in real-time the multi-faceted nature of brain function[77-80] and dysfunction[81] at optical spatial resolutions. However, their need to interrogate multiple neurophysiological variables necessitates the development of imaging systems that combine multiple optical contrast mechanisms. Such systems tend to be expensive and bulky as their components have a substantial benchtop 'footprint'. Moreover, multi-contrast imaging systems often need to be custom fabricated as they are not widely available. This has created a formidable entry barrier for multi-variable or multi-contrast neuroimaging systems. In addition, their bulkiness often requires the animal to be anesthetized, and restricts the use of complementary recording equipment, such as wired EEG recording arrays and amplifiers. Although miniaturized microscope designs[82] have emerged that lower this barrier, current systems are limited to performing either neural[28, 83, 84] or hemodynamic imaging[85-89], but not both. This in turn has limited *in vivo* experiments in awake animals to those that interrogate either neuronal or vascular function, but not both.

To fulfil this unmet need, we created a miniaturized microscope that combines three optical contrast mechanisms: fluorescence[90] (FL), hemoglobin intrinsic optical signals[91] (IOS) and laser speckle contrast[58] (LSC). The FL channel enables imaging of neural activity with voltage sensitive dyes[92] or via genetically

encoded calcium indicators such as GCaMP[93]. IOS and LSC enable imaging hemoglobin absorption and cerebral blood flow, respectively. This microscope costs significantly less than traditional benchtop systems due to our use of commercially available components such as LEDs, a micro-lens, a CMOS image sensor etc., as well as an entirely 3D printed housing. We also included a 'synchronization' (sync) channel as part of the microscope. This feature allows image acquisition to be 'time-locked' with complementary recording systems (e.g. a physiological monitoring system), or a system that provides a stimulus to the animal (e.g. a whisker deflector). Our microscope weighs 9 g and occupies 5 cm3, and is well suited for in vivo neuroimaging in awake mice and rats. The microscope has a 5 μm spatial resolution which enables resolving individual microvessels. It covers a 3×3 mm2 wide-field or mesoscopic field of view (FoV) permitting one to simultaneously interrogate an entire cortical region (e.g. the auditory cortex or motor cortex). Furthermore, the microscope acquires images at 15 frames per second (fps), allowing dynamic neurovascular changes to be captured with temporal fidelity.

We first present the design details of the microscope and compare its performance to a benchtop based multi-contrast imaging system. Next, we demonstrate its utility by performing multiple *in vivo* experiments that exploit its multi-contrast capabilities to interrogate both neural activity and concomitant hemodynamic changes in awake animals.

3.2 Results

3.2.1 A miniaturized design that incorporates three distinct optical contrast mechanisms

In contrast to previously reported miniature microscope designs[83, 84, 94], we marginally traded magnification in favor of a wider field of view (FoV). The resultant larger object distance enabled us to insert multiple illumination sources for multi-contrast imaging while retaining a 5 μm spatial resolution over a 3×3 mm^2 (i.e. 'wide-field' or mesoscopic) FoV.

The microscope comprises a 3D printed base and upper assembly (**Figure 3.1a-b** and **Detailed methods**). The base houses three illumination sources (**Figure 3.1a**): a blue (452 nm) LED provides excitation for fluorescence imaging; green (570 nm) LEDs and a red (680 nm) laser diode provide illumination for IOS imaging of total hemoglobin (HbT, at 570 nm) and deoxyhemoglobin absorption (dHb, at 680 nm), respectively. Additionally, acquiring speckle contrast images under red laser illumination enables us to map cerebral blood flow (CBF). Finally, a pair of orange LEDs acts as an optical *sync* signal for synchronizing image acquisition with external instruments or recording hardware.

The 3D printed upper assembly contains the elements necessary for light filtering, image formation and focusing (**Figure 3.1b**). A 510 nm long-pass filter rejects blue excitation light (< 510 nm) while permitting light from the other illumination sources to reach the image sensor. A single (f = 4.6 mm) aspheric lens was used for image formation. Images are captured by a 640×640 pixel, 10-

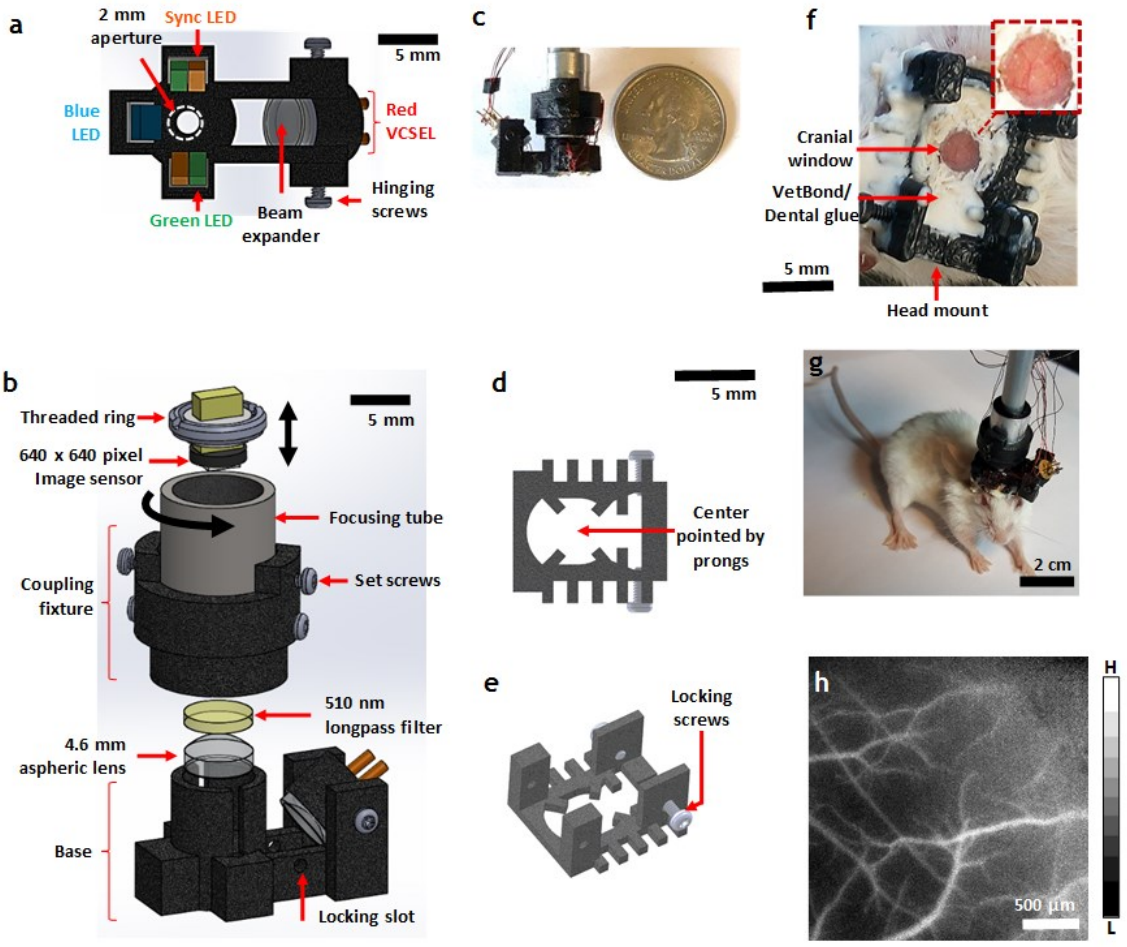

Figure 3.1 A miniaturized design that incorporates three distinct optical contrast mechanisms. (a) The microscope base unit. Excitation for green fluorescent imaging is provided by a blue LED, while HbT imaging is carried out with a pair of green LEDs. A red VCSEL, assisted by a beam expander and hinging screws, facilitates dHb and LSC imaging. A separate pair of orange LEDs (*sync* LEDs) is used for synchronizing with an external EEG system. The FoV lies directly below the aperture. (b) The upper unit of the microscope (shown together with the base) consists of a 4.6 mm focal length lens, a 510 nm long-pass filter to eliminate blue fluorescence excitation, a focusing tube and an image sensor. (c) The complete microscope assembly is shown with a U.S. quarter coin next to it for scale. (d, e) The bottom and side views of the head mount, respectively. The head mount is surgically implanted on the rodent's skull and

enables firm attachment of the microscope via a pair of locking screws. The pronged structure at the base of the head mount facilitates centering on the FoV. (f) Head mount attached to a mouse skull with the inset showing the cranial window preparation for optical access to the brain. (g) An awake and freely moving mouse with the microscope. (h) A grayscale CBF map acquired with the microscope using LSC from an awake mouse. All parts were rapid prototyped and 3D printed permitting a high degree of customization. Scale bars indicate length where applicable.

bit CMOS image sensor with a pitch of 3.6 μm. The final miniature microscope (**Figure 3.1c**) weighs 9 g, occupies 5 cm^3, is directly powered and controlled by a laptop computer, and can acquire images at 15 fps.

3.2.2 Disposable head mount enables microscope reusability

We designed a customized, disposable head mount (**Figure 3.1d, e** and **Methods**) for the microscope to interface with the rodent brain. Each head mount was 3D printed and attached permanently atop a surgically prepared cranial window **Figure 3.1f** and **Detailed methods**). Set screws within the head mount minimize microscope motion and enable robust attachment (**Figure 3.1g**) for high-resolution *in vivo* imaging (**Figure 3.1h**). Loosening the set screws allows the microscope to be conveniently detached and reattached whenever the experimental protocol demands it.

3.2.3 Supplementary control modules and GUI enhance 'plug and play' portability

We supplemented the microscope system with two compact control modules: an illumination controller (**Detailed methods and Supplementary Figure 3.1**) and a commercially available image acquisition controller (**Detailed methods**). Collectively, they miniaturize the hardware needed for illumination current generation and high speed image acquisition. A flexible wire bundle links the head-mounted microscope to the two control modules, which in turn are powered by USB connections to a standard laptop computer (**Detailed Methods** and **Supplementary Figure 3.2a, b)**. This configuration results in a completely portable imaging system that can be conveniently transported to any site for imaging in awake, behaving animals (**Supplementary Figure 3.2c**). A custom designed 'all-in-one' graphical user interface (GUI, **Supplementary Figure 3.2d**) facilitates control of all the imaging parameters while providing real-time image visualization. These features enhance the 'plug and play' utility of the system.

3.2.4 Performance of the miniature multi-contrast microscope was comparable to that of a similarly equipped benchtop imaging system

We performed high-resolution, wide-field micro-angiography of an anesthetized mouse brain with the microscope. To validate its performance for each optical contrast mechanism, we also imaged the same FoV with a comparable multi-contrast benchtop system (**Detailed methods**). Images of cortical

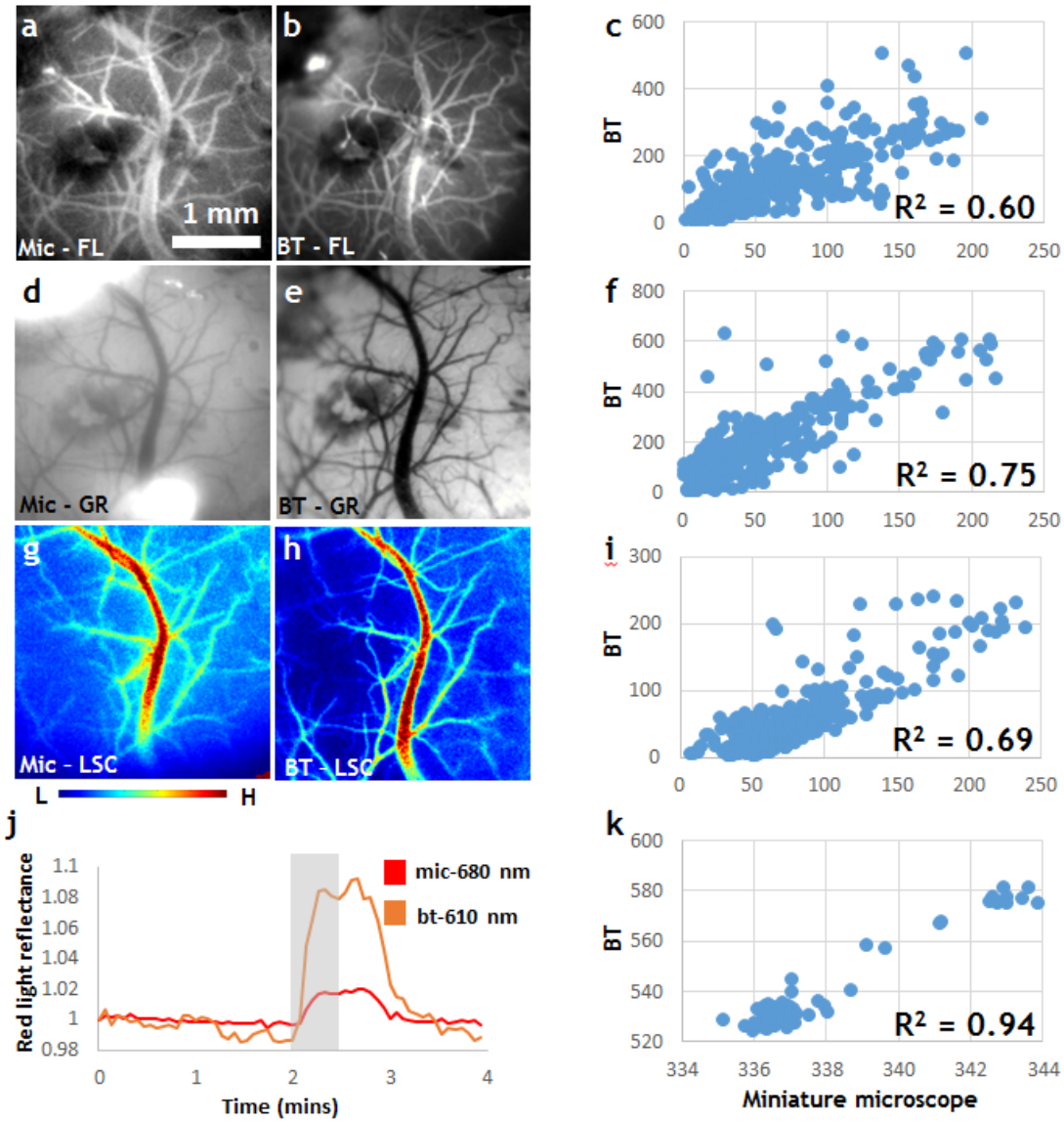

Figure 3.2 Performance of the miniature multi-contrast microscope was comparable to that of a similarly equipped benchtop imaging system. Multi-contrast images of a mouse brain acquired using our microscope (Mic) and a similarly equipped benchtop (BT) imaging system were compared. (a, b) A network of cerebral microvessels visualized with fluorescence imaging (FL) following a tail vein injection of dextran-FITC. (d, e) The same FoV imaged using green IOS (GR) illustrating HbT (or relative CBV) distribution. (g, h) Pseudo-colored maps of relative CBF velocities obtained by performing speckle contrast imaging under laser illumination (LSC). (j)

Time courses of the dHb-dependent red light reflectance from a central 20×20 pixel FoV showing the temporal response to an oxygen challenge (i.e. inhalation of 100% O_2 for 30s starting at 2 mins, followed by room air for the rest of the experiment). (c, f, i, k) Scatter plots of the *in vivo* BT vs. Mic measurements shown in (a-h). Spatial correlations were computed for a 20×20 pixel grid superimposed over a central 400×400 region. The scale bar indicates length assuming a magnification factor of ~0.75.

microvasculature obtained from the two systems with fluorescence (**Figs. 3.2a, b**), green light (**Figure 3.2d, e**) and laser speckle contrast (**Figure 3.2g, h**) were compared for similarity using a central 400×400 pixel region overlaid with a 20×20 pixel sampling grid. For each contrast mechanism, correlation coefficients (R^2) of 0.60, 0.75 and 0.69 were observed, respectively (**Figure 3.2c, f, i**). As additional validation, red light absorption was used to track temporal changes in dHb levels in response to an oxygen challenge. Time traces from each imaging system for a central 20×20 pixel region showed an increase in the red reflectance signal (**Figure 3.2j**), i.e. a decrease in dHb, as well as a an R^2 of 0.94 (**Figure 3.2k**). Collectively, these data validate the ability of our microscope to conduct *in vivo* imaging using each of the three optical contrast mechanisms.

3.2.5 Multi-contrast imaging reveals the spatio-temporal mismatch between focal neural activation and wide-area hemodynamic response to auditory stimulation

We performed multi-contrast imaging of the mouse auditory cortex in response to sound stimuli in an awake mouse (**Figure 3.3a** and **Detailed methods**). Here,

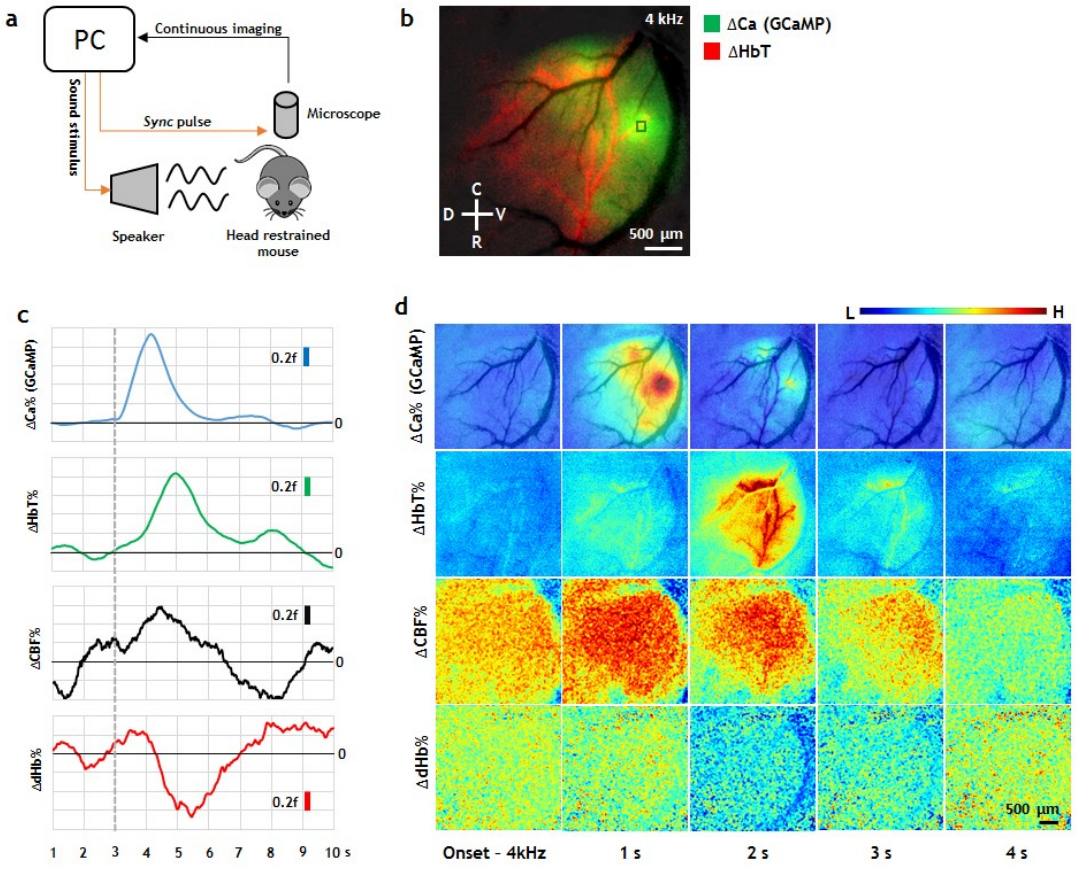

Figure 3.3 Multi-contrast imaging reveals the spatio-temporal mismatch between focal neural activation and wide-area hemodynamic response to an auditory stimulus. (a) Schematic of the experimental setup for the auditory stimulation and image acquisition. (b) A composite (i.e. RGB) map showing the maximum calcium response (green channel) and the corresponding maximum vasodilatory response (red channel) to a 4 kHz stimulus. Anatomical directions dorsal (D) – ventral (V), caudal (C) – rostral (R) are marked for reference. The black background image is a 'vessel mask' (i.e. binarized blood vessel image) underlay. (c) Time traces of the calcium and hemodynamic responses to a 4kHz stimulus in the 20×20 pixel region of interest (ROI) shown in (b). The ordinates for each plot are in fractions '*f*' of the peak response amplitude. The black line indicates the baseline for each trace. A sliding 1s window was used to smooth the time traces. (d) Snapshots illustrating the spatiotemporal evolution of the neurovascular response to 4 kHz stimulation. Each image sequence has been smoothed using a

3×3 median filter and normalized to 0.1% of its range. For visual clarity, the CBF and dHb images were additionally smoothed with a 10×10 mean filter before normalization. A vessel mask underlay is used in the first row of images to provide a visual reference. The image intensity in each row is normalized to 0.1% of the range. Scale bars are shown assuming a magnification of ~0.75.

we present results for a 4 kHz auditory stimulus. We successfully captured the time evolution of neural activation (via GCaMP bound calcium fluorescence[95]) and the concomitant hemodynamic response in terms of vasodilation (i.e. change in blood volume as indicated by the change in total hemoglobin concentration or HbT), cerebral blood flow (CBF) and oxygenation (dHb) changes (**Figure 3.3b**). Time-course analysis revealed the classic hyperemic lag between neural firing and the onset of the hemodynamic response[96] (**Figure 3.3c** and **Detailed methods**). The sharp rise in calcium accumulation due to neural firing was followed by a rise in total hemoglobin (HbT), an increase in local CBF and a dip in deoxyhemoglobin (dHb) with a delay of ~1 s. The calcium activity showed strong spatial specificity to distinct regions of the auditory cortex (**Figure 3.3d,** ΔCa%). Vasodilation, as indicated by the rise in HbT, showed the preferential recruitment of a specific microvascular 'irrigation territory' to cater to this increased metabolic demand (**Figure 3.3d,** ΔHbT%). In contrast, elevated CBF levels were observed globally and did not show any spatial specificity (**Figure 3.3d,** ΔCBF%). Moreover, most of the auditory cortex exhibited an increase in HbT along with a dip in dHb (**Figure 3.3d,** ΔdHb%), suggesting that much of the post-stimulus perfusion to the region was hyper-oxygenated. Finally, by

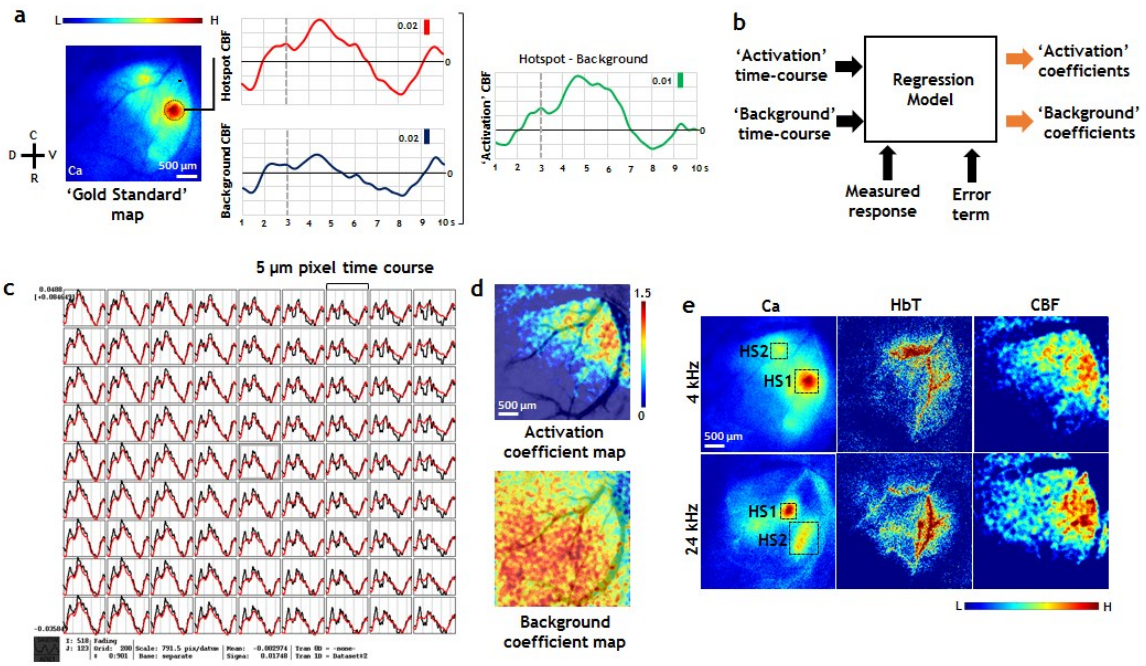

Figure 3.4 Microscope enables wide-area functional mapping analogous to classic task-based fMRI. (a) Generation of the 'activation' CBF time-course by subtracting the background CBF time-course from the hotspot (i.e. corresponding to the calcium activation pattern) CBF time-course. (b) Schematic of the image processing pipeline. The 'activation' and 'background' time-courses were used as regressors to compute the activation and background coefficients from the measured signal using a multiple linear regression model. (c) AFNI screenshot showing pixel-wise CBF time courses and their corresponding model fits (black: measured CBF response, red: model fit) over a 9×9 pixel area corresponding to the black square in (a). (d) Maps of the activation and background coefficients for a 4 kHz stimulation computed from the regression model. Negative coefficients are not displayed. Maps are overlaid on a vessel mask for visual reference. (e) Ca, HbT and CBF activation coefficient maps for 4 and 24 kHz stimuli. Ca maps were normalized to 0.1%.HbT and CBF fit coefficients are shown over 0–1.5. Two calcium hotspots are marked on each calcium activation map: HS1 and HS2. One can see that the HbT and CBF coefficient maps exhibit more tonotopic specificity to the Ca signal than the raw HbT and CBF maps.

comparing the pre-stimulus patterns in both **Figure 3.3c** and **d,** we note that the stimulus-evoked CBF response rides on top of a large non-stimulus (or resting-state) related fluctuation that is spatially non-specific.

3.2.6 Microscope enables wide-area functional mapping analogous to classic task-based fMRI

Task or stimulus based functional magnetic resonance imaging (fMRI) techniques[97] have been extensively used over the last two decades to interrogate the functionality of different brain regions[98]. Typically, the observed stimulus-evoked blood-oxygen-level-dependent (BOLD) response is input into a pixel-wise regression model to identify activated pixels by removing the effect of time constants (i.e. by deconvolving with an 'activation' hemodynamic response function), as well as eliminating the effects of background fluctuations and system noise (**Figure 3.4b**). Here, we processed our multi-contrast imaging data with a standard fMRI signal processing software (Analysis of Functional Neuro Images: AFNI[99]) and implemented an fMRI-type functional mapping of the auditory cortex. This approach is in contrast to conventional functional optical imaging approaches wherein one usually calculates an average signal over the desired FoV without displaying or computing the pixel-wise response.

We treated the calcium response map as the 'gold standard' for identifying activated areas, and created an ideal hemodynamic response (i.e. an 'activation' time-course) by subtracting the average background hemodynamic signal from

the hemodynamic response corresponding to the calcium hotspot pixels (**Detailed methods**). **Figure 3.4a** illustrates this using CBF time-courses. We then input this activation time-course and the background time-course into a linear regression model that generated pixel-wise 'fit coefficients' for each time-course (**Figure 3.4b** and **Detailed methods**). These 'fit coefficients' enabled us to assess activation differences on a 'pixel-wise' basis for the entire auditory cortex analogous to classic fMRI paradigms, instead of on a single time course spatially-averaged over the auditory cortex (**Figure 3.4c**). This approach also enabled us to isolate localized CBF changes from background CBF fluctuations (**Figure 3.4d**). We then applied the same image-processing pipeline to determine if we could map the tonotopy of the auditory cortex by comparing the HbT and CBF responses to a 4 and 24 kHz stimulus, respectively. We did not use the dHb responses because of their low signal-to-noise ratios (SNRs). In accordance with previous tonotopic studies of the murine auditory cortex[100], the 4 and 24 kHz calcium activation maps exhibited distinct spatial patterns (**Figure 3.4e, Ca**). Following the regression analysis, both the HbT and CBF activation coefficients demonstrated distinct spatial localization corresponding to the 4 and 24 kHz stimulus (**Figure 3.4e, HbT, CBF**). This was in contrast to the unprocessed HbT and CBF response observed in **Figure 3.4d**.

3.2.7 Multi-contrast imaging during arousal from anesthesia reveals that CBF changes correlate with average EEG power and neurovasculature exhibits differential compliance

Most *in vivo* neuroimaging experiments in rodents are conducted under general anesthesia[101-103]. In many cases, a one-time injection (e.g. a ketamine/xylazine cocktail) is used to provide anesthesia for the entire duration of the experiment[104-107]. Once the depth of anesthesia is confirmed (e.g. by toe-pinching), it is usually assumed that baseline brain physiology remains stable and that any observed variations are attributable to the experimental paradigm. We used the multi-contrast capability of our microscope to assess the validity of this assumption. We interrogated CBF changes (with LSC) over a 3×3 mm^2 FoV in the right hemisphere of the mouse brain (**Figure 3.5a and Detailed methods**). An EEG screw electrode was surgically implanted on the contralateral hemisphere, allowing concurrent global electrophysiology monitoring via an external EEG recording instrument (**Figure 3.5b and Methods**). Both CBF and EEG power continually decreased during deep anesthesia (**Figure 3.5b**, ~20%). At the end of an hour, anesthesia was re-confirmed by the lack of response to a hind-paw pinch. Signs of wakefulness (e.g. first twitching of whiskers, then body movement etc.) emerged at around two hours. Both CBF and EEG power had reached their minimum by this time, and increased with improving signs of wakefulness (**Figure 3.5b**). Total EEG power changes were correlated to CBF changes (R^2 = 0.70). Power in each of the standard EEG sub-bands showed

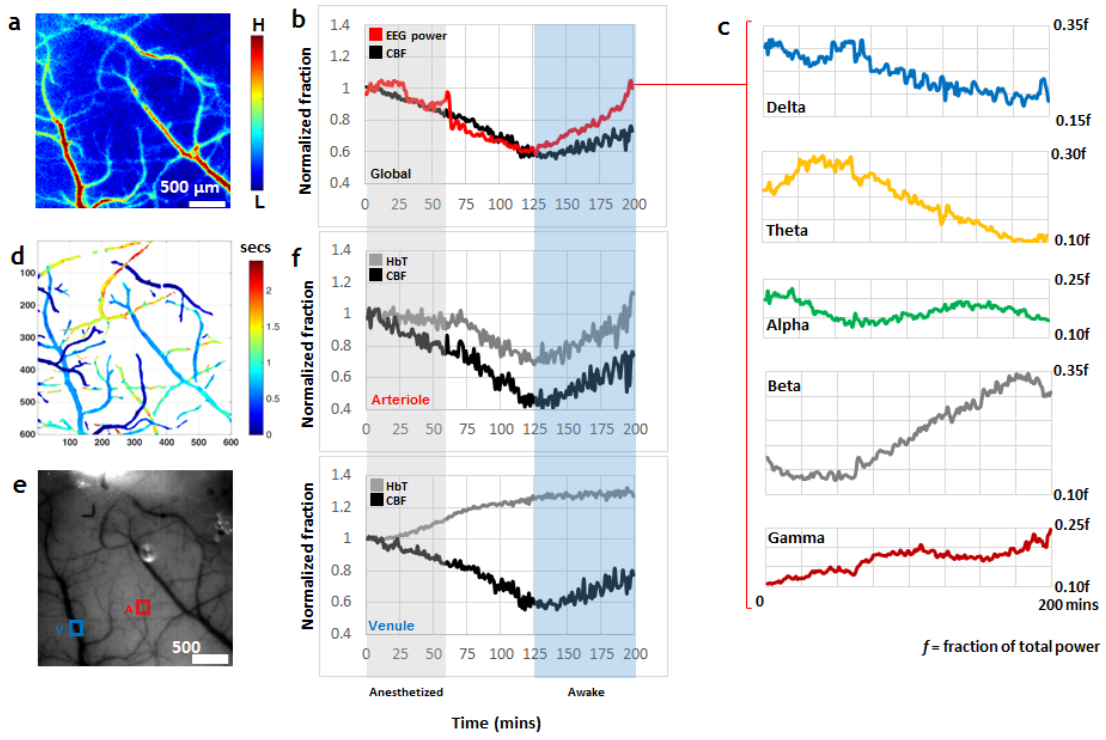

Figure 3.5 Multi-contrast imaging reveals that CBF changes correlate with average EEG power and the neurovasculature exhibits differential compliance during arousal from anesthesia. (a) Map of the average CBF over the duration of the experiment. (b) Fluctuations in global EEG power and CBF are correlated. The anesthetized phase and awake phases are indicated by a colored blocks. (c) Plots of the power in EEG sub-bands showing how each varied during arousal from anesthesia. The post-script 'f' depicts the power of each sub-band as a fraction of the total EEG power. (d) Pseudocolored map illustrating the differences in arrival time of an intravenously injected fluorescent tracer (dextran-FITC). Arrival times are indicated relative to the earliest appearance of the fluorescent tracer within the FoV. (e) IOS map acquired under green light illumination showing HbT absorption for the same FoV. An arteriole (A) and venule (V) are identified in the FoV. (f, g) Fluctuations in HbT (i.e. CBV) and CBF within the arteriole and venule, respectively.

typical fluctuations from a sleep to awake state[108], and did not reveal a similar correlation with CBF (**Figure 3.5c)**.

During the same experiment, we also used the fluorescence channel to differentiate the microvascular bed into its arterial and venous components by exploiting the arrival times of an intravenously injected fluorescent tracer (fluorescein-dextran, 70 kDa). (**Figure 3.5d** and **Detailed methods**). We then identified an arteriole and a venule (**Figure 3.5e**), and interrogated their blood flow (with LSC) and blood volume changes (with 570 nm IOS). The arteriole exhibited tight coupling between blood volume and blood flow (**Figure 3.5f**); namely an initial vasoconstriction phase with a decrease in flow and eventual vasodilation concomitant with recovery in blood flow, suggesting flow modulation based on vessel diameter. However, this relationship was different for the venule that exhibited blood flow alterations uncorrelated with its changes in blood volume (**Figure 3.5g**). Collectively, these observations suggest that global variations in brain physiology during the transition from anesthetized to awake states persist at the local or microvascular scale.

3.3 Discussion

In this work we shrank the dimensions of a conventional multi-contrast neuroimaging system[6, 72, 73] down from several feet (e.g. 5×5×5 feet) to the size of a fingertip (5 cm^3) (**Figure 3.1** and **Figure 3.2**). Miniaturization enables neuroscientists to head-mount our microscope on an awake and freely moving rodent to interrogate *in vivo* neural activity and concomitant hemodynamic changes. In addition, one only requires a standard laptop to power up and control the microscope, ensuring complete system portability. Our miniaturized

microscope offers 'plug and play' functionality, permits real-time imaging and control of all the imaging parameters via the user friendly GUI.

We exploited the microscope's high spatial (5 μm) and temporal (15 fps) resolution, and its 3×3 mm^2 FoV to simultaneously interrogate the entire auditory cortex at microvascular spatial resolution in an awake mouse (**Figure 3.3a, b**). We observed for the first time, how neural calcium dynamics, the vasodilation of individual microvessels and the elevation of local CBF levels were orchestrated by a functional auditory stimulus (**Figure 3.5c, d**). We then used an fMRI-type analysis pipeline (**Figure 3.4a, b**), to remove background fluctuations from each hemodynamic response variable, thereby permitting the visualization of more specific functional activation (**Figure 3.4c, d**). We were able to demonstrate the tonotopic specificity of the hemodynamic responses to 4 and 24 kHz auditory stimuli (**Figure 3.4e HbT, CBF**) by using the distinct spatial calcium dynamics (**Figure 3.4e, Ca**) as the tonotopic gold standard of activation.

We then used the microscope's *sync* channel to time-lock image acquisition with EEG recording. This permitted us to compare changes in global CBF to concomitant EEG recordings during anesthetized and awake states (**Figure 3.5a, b**). We found that the CBF and average EEG power were highly correlated (R^2 = 0.70) and varied significantly (~40%), reaching a minimum during the sleep-wake transition (**Figure 3.5b**). In contrast, the power of standard EEG sub-bands did not reveal similar correlations with CBF (**Figure 3.5c**). We exploited the microscope's fluorescence channel to perform arterial-venous discrimination by measuring arrival times of an intravenously injected fluorescent dye (**Figure**

3.5d). We then used this information to demonstrate that arterioles and venules show unique variations in their respective flow-volume relationships (**Figure 3.5e-g**). These global and local variations imply that one must exercise caution when comparing results from *in vivo* functional imaging experiments in anesthetized and awake animals.

Our microscope represents a critical advancement in engineering design and miniaturized fabrication. In contrast to previous fluorescence microscope designs[2, 28, 83], we marginally relaxed our magnification requirements to achieve a wider FoV (e.g. 18× described by Ghosh et al[2]). This wide-field capability permits us to interrogate an entire cortical region (e.g. the entire murine motor cortex) or to analyze the 'functional overlap' between adjacent cortical regions (e.g. auditory-somatosensory cortices in mice). Moreover, this design modification made it possible to combine three optical contrast mechanisms within one miniature housing by creating space for additional illumination sources (**Figure 3.1a-c**).

The multi-contrast capability of our microscope enables us to interrogate aspects of neurophysiology that are critical to neuroscience and neuropathology. In addition to visualizing calcium dynamics in neurons[109, 110] and astrocytes[111, 112], the inclusion of a fluorescence channel facilitates imaging of fluorescently tagged cells[113, 114] as well as the uptake of fluorescently labeled pharmacological agents[115, 116]. The availability of separate green light IOS[91] and laser speckle contrast[12] imaging channels enables the independent observation of microvascular morphology and blood flow. This is especially useful in

applications in which the regulation of blood flow and vessel architecture is dysregulated (e.g. during tumor angiogenesis[117, 118]), or when the microvascular network is poorly perfused (e.g. during stroke[119, 120]). Concurrent measurement of dHb absorption under red light illumination supplements the other contrast mechanisms with vital information on oxygenation status and helps identify hypoxic regions (e.g. ischemia[121], tumor necrosis[122]) and hyperoxic regions (e.g. functional activation[123, 124]). The capability to map dHb can also be exploited to directly validate BOLD fMRI data with optical imaging data[125]. Correlating multi-contrast images from our microscope with behavioral observations in awake animals would add another dimension of insight to current neurophysiological studies. For example, with our head-mounted microscope we could conduct *in vivo* imaging of cognitive activity while the mouse is exploring a maze.

We also showcased the use of a non-standard image processing pipeline (i.e. fMRI-type analysis) on high-resolution multi-contrast optical imaging data (**Figure 3.4**). In contrast to the convention of showing a single time-course from the activated region (**Figure 3.3c**), we demonstrated the ability of our microscope to conduct wide-area mapping of neural activity and the accompanying hemodynamic responses (**Figure 3.4c, e**). Moreover, this multi-contrast approach to functional imaging wherein both, the neural and hemodynamic responses can be characterized simultaneously and independently has the potential to improve and inform image processing strategies for other imaging modalities. Our demonstration can serve as a model for microscopy, image processing and provide a data analysis framework for other researchers.

Our microscope offers all these benefits at a fraction of the cost of a benchtop multi-contrast benchtop imaging system. This is due to our extensive use of 3D printing techniques that are more economical than conventional machining/fabrication, as well as our use of off-the-shelf opto-electronic components. The disposable head mounts and flexible microscope attachments (**Figure 3.1c, d**) allow the microscope to be removed from the animal when imaging is not being conducted. This feature enables our microscope to be used concomitantly on multi-animal cohorts wherein longitudinal (e.g. daily) *in vivo* imaging is necessary. We believe this microscope's affordability and flexibility will play a major role in making it a ubiquitous laboratory tool in the near future. We envision several exciting additions to the microscope that could enhance its extant capabilities. For example, the use of a tri-modal (multi-wavelength) laser diode[126] instead of a single mode laser would enhance the estimation of oxygen saturation. The addition of an LED for optogenetic stimulation[127] could equip our microscope with the capacity to excite or inhibit neural activity while performing concurrent multi-contrast imaging. In addition, the cranial window preparation through which imaging is carried out could be modified to incorporate a transparent electrocorticographic (ECoG) grid[128] to allow direct recording of neural activity. Simultaneously recording ECoG along with blood flow or oxygen saturation estimation would be very useful in imaging stroke and its penumbra region[119, 129, 130], or imaging areas of spreading depression[131, 132], or areas spawning epileptogenic response to focal drug injection[133, 134].

With its current capabilities and potential for expandability, we believe our microscope will herald an exciting new era in neuroscience research.

3.4 Detailed methods

3.4.1 Microscope base

The base contains all the light sources necessary for multi-contrast imaging (**Figure 3.1a**). Excitation for green fluorescence imaging is provided by a blue surface mount light emitting diode (SMT LED) with a center wavelength of 452 nm, and a full width half maximum (FWHM) of ±13 nm (Osram Opto Semiconductors, LD CN5M-1R1S-35-1-Z). Imaging of total hemoglobin (HbT) levels is accomplished by using a pair of green SMT LEDs with 570±20 nm illumination (Broadcom, HSMF-C157). A miniature 680 nm vertical cavity surface emitting laser (VCSEL) diode (Vixar, IO-680S-0000-B093) , assisted by a 6 mm focal length concave lens (Anchor optics, 27753) for beam expansion and a pair of hinge screws (McMaster-Carr, 96710A050) for fine-tuning the laser spot location, facilitates imaging deoxyhemoglobin (dHb) absorption. Performing LSC calculation under laser light illumination enables imaging of CBF. A separate pair of orange colored LEDs (as part of Broadcom, HSMF-C157 package) serve as a *sync* signal for synchronizing external systems with our microscope. The 3×3 mm FoV lies directly underneath the 2 mm aperture of the microscope.

3.4.2 Microscope upper assembly

The upper assembly contains the rest of the elements of the microscope (**Figure 3.1b**). A 6 mm diameter, 4.6 mm focal length aspheric lens (Thorlabs, A-390) is

used to focus light with a magnification of 0.75. A 510 nm, 1 mm thick optical long-pass filter (Omega Optical, 510ALP) selectively excludes blue excitation light. A 640×640 pixel grayscale image sensor (CMOSIS, NanEyeGS) is used to acquire images. The 3.6 μm pitch pixels with 10-bit digital resolution facilitate high quality image acquisition at ~15 fps. The image sensor is mounted on a focusing tube (Thorlabs, AD8T) attached to a custom built coupling fixture, allowing its position to be varied vertically to achieve focus. A pair of set screws (McMaster-Carr, 96710A050) locks the image sensor position once focusing has been achieved.

Both the microscope base and upper assembly were rapid prototyped with ABSplus material using a 3D printer (Stratasys, Dimension bst1200es).

3.4.3 Head mount design

Figure 3.1c, d show the bottom and the side views of the head mount. The head mount is implanted on a surgically exposed rodent skull, and enables our microscope to firmly attach via a pair of locking screws (McMaster-Carr, 96710A050). The prong structure at the bottom face of the head mount allows it to be centered on the surgically prepared FoV at the time of implantation. Friction caused by the tight fit between the microscope base and the head mount assists the locking screws in holding the microscope in place.

A different head mount design was used for the auditory stimulus experiment as it required attachment of the microscope to a head-immobilized mouse (**Supplementary Figure 3.3**).

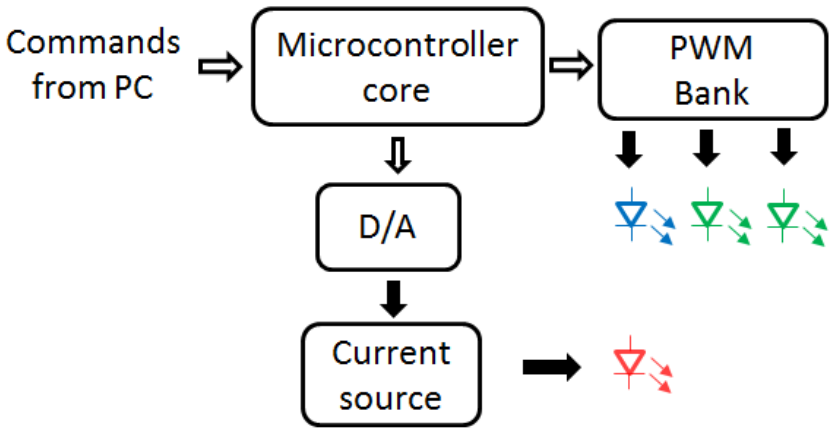

Supplementary Figure 3.1 Schematic of the illumination control module. Commands from the master program residing in the PC are sent to the microcontroller core via serial communication. Accordingly, the microcontroller activates the PWM modules or the D/A converter. If LED illumination is desired, a combination of three separate PWM modules is activated: one each for the blue LED, and the left and right green LEDs. In the case of laser illumination, the D/A creates an analog voltage which is converted into a steady current level by the current source, which then delivers the current through the laser diode. Digital transmission is indicated by hollow arrows while analog connections are indicated by solid arrows.

3.4.4 Illumination control module

We designed a compact illumination control module to deliver user-programmable levels of illumination (**Supplementary Figure 3.1**). A microcontroller (Arduino Uno) receives commands from the master program (residing on the PC) regarding the ON/OFF status of each illumination source as well as the amount of current to be delivered across each illumination source. If

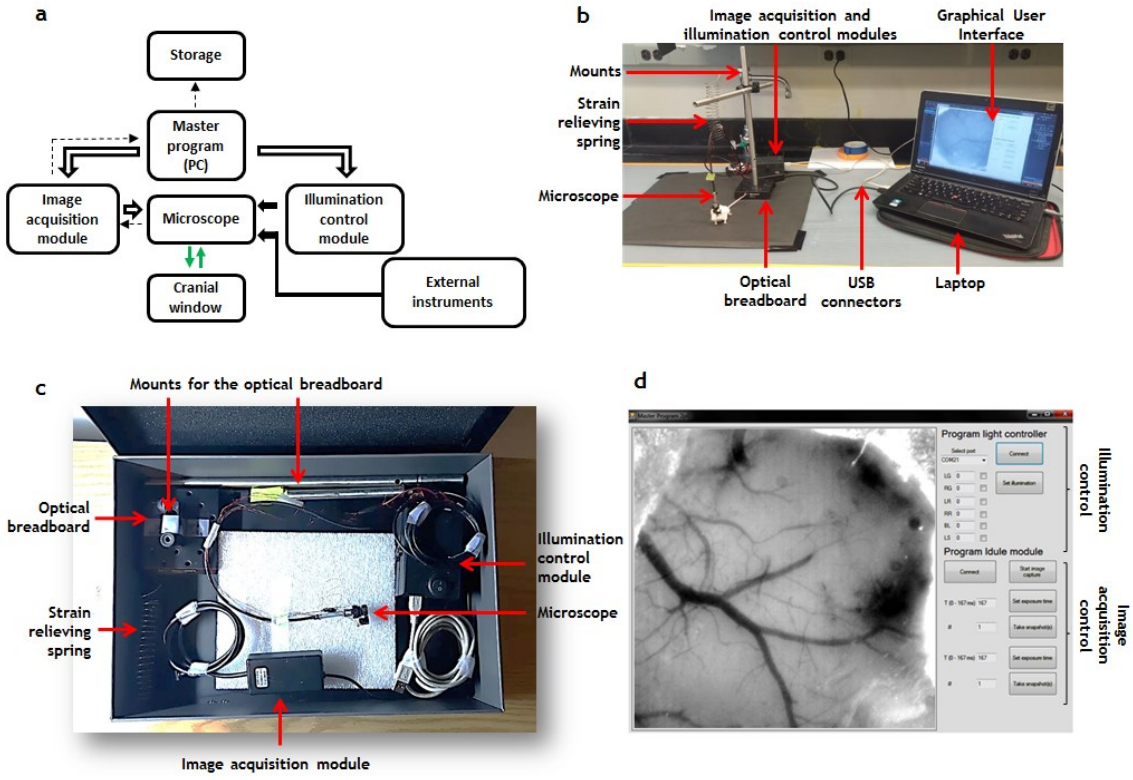

Supplementary Figure 3.2 The system architecture for microscope control. (a) A master program running on a PC plays the role of a central hub to all control and data flow. It sends digital commands via a USB interface to the illumination control module to switch ON/OFF individual illumination sources at different light levels. In turn, the illumination control module creates the required current levels and drives the light sources in the microscope base unit. In addition, the master program sends commands to the image acquisition module which interacts with the image sensor inside the microscope. Images acquired by the image sensor are relayed back through the image acquisition module to the master program which deposits the images into a storage medium. External instruments can be synchronized with microscope image acquisition via the synchronization (*sync*) channel. Digital communication is indicated in hollow arrows while analog current supply is shown by a solid arrow. Light illumination of and the collection from the cranial window by the microscope is represented by a pair of green arrows. The path of acquired images from the microscope through the image acquisition module, the master program until the storage medium is shown in dashed arrows. (b) The entire imaging system is controlled and

powered by a standard laptop computer. (c) A 'briefcase' version of the microscope: all microscope parts can be easily stowed away for easy transportation. (d) A screen shot of the GUI.

LED illumination is desired, the Arduino will activate one of its pulse width modulation (PWM) modules. The

appropriate duty cycle to be used is calculated by the program running in the Arduino. Each of the blue, left and right green LEDs have their own dedicated PWM module allowing flexibility in illumination control. The laser diode requires a continuous current. Therefore, an analog-to-digital (A/D) module (Microchip, MCP4821) is used to create an analog voltage level that is converted into a corresponding current level by a voltage-to-current converter circuit. Current levels of up to 5 mA are used to drive the blue LED, while the green LEDs each require ~20 mA. The laser is driven at 2~2.5 mA.

3.4.5 System architecture

The overall system architecture is shown in **Supplementary Figure 3.2a**. A custom written master program residing on a personal computer (PC) controls all data and command flow. The commands received by the illumination controller result in switching ON/OFF of different illumination sources at desired current levels. Additionally, the master program communicates with the image acquisition module (CMOSIS, Idule module) to set the exposure time of the image sensor, as well as initiate image capture. Images acquired by the sensor are sent via the

image acquisition module to the master program that then stores the data on external storage. Image processing was carried out off-line.

3.4.6 Cranial window preparations

For microscope validation and arousal from anesthesia experiments: Anesthesia was induced with an intraperitoneal injection of ketamine (90 mg/kg) and xylazine (5 mg/kg). After checking the depth of anesthesia with manual forepaw or tail stimulation (pinching), eye ointment (Purelube, NDC 17033-211-38) was spread over the mouse's eyes to prevent dehydration. The fur over the scalp was trimmed and the exposed area sterilized with 70% ethanol. An incision was made over the right parietal bone and the overlying skin and fascia removed. After thoroughly drying the exposed area, the boundary of the cranial window to be

drilled was marked with a pen. Next, the skull was thinned with a microdrill (Aseptica, AEU-10SS) until the underlying vasculature became visible. The entire area was flushed with saline and thoroughly dried. The head mount was centered on the cranial window and attached using a thin layer of cyanoacrylate glue (Loctite, 43903). A self-curing dental cement (Parkell S380) was used to further secure the head mount to the skull and cover any exposed areas (**Supplementary Figure 3.1e**).

For the auditory stimulus experiment: Anesthesia was induced with 4% isoflurane at an O_2 flow rate of 0.5 L/min. The mouse head was secured to a stereotaxic frame with a bite bar while anesthesia was maintained at 1-2% isoflurane with 0.5 L/min through a tube attached to the bite bar. Petroleum jelly (Vaseline) was

spread over the mouse's eyes to prevent dehydration. The hair over the scalp was trimmed and the exposed area sterilized with 70% ethanol. Injections of dexamethasone (2 mg/kg) and carpofren (5 mg/kg) were administered. After lidocaine (2% with 1:100,000 epinephrine) was injected locally, an incision was made on the midline of the head. The skin and fascia were removed over the area of the cranial window. The area was thoroughly dried and a primer (Optibond, 33533) applied to the surface. A custom-built steel head post was secured with an UV-cured dental cement (Heraeus, 0197) to the exposed area of the skull. Using vasculature and local landmarks, the area of the cranial window (above the left auditory cortex) was identified with a pen. A craniotomy was performed with a microdrill (Fordom, MH-170) and the bone detached from the skull leaving the dura intact. After clearing the area of debris, a cover-slip was placed on top of the craniotomy and secured with self-curing dental cement (Parkell, S380). During the procedure, 0.9% saline was injected to prevent dehydration. After the procedure was finished, buprenorphine (.5 mg/kg) was injected (analgesic) and Bacitracin (Fougera) administered topically (**Supplementary Figure 3.3d**).

3.4.7 Brain imaging procedures

Microscope validation: A thinned-skull cranial window was prepared on a male Fisher (25g) mouse as described before. After recovery, the mouse was anesthetized briefly with isoflurane in a chamber. Subsequently, anesthesia was maintained through a nose cone by providing 2% isoflurane mixed with room air at 1 L/min flow rate. An oxygen challenge was performed under red laser

illumination: 30 s of oxygen was provided after a 2 min baseline of room air. Imaging was continued for a total of 4 mins. Next, a stack of images was acquired under green light illumination. For fluorescence imaging, 0.2 mL of 10 mg/kg fluorescein-dextran (70 kDa) was injected through the tail vein. Images under blue illumination were captured before and after the injection. The mouse was then moved to the benchtop imaging system, and the same imaging protocols performed. Note: a second injection of FITC was not performed on the benchtop as the mouse already had a high dose of FITC in its blood stream.

Optical functional imaging experiment: An open skull cranial window was prepared over the left auditory cortex of a female tetO-GCaMPs×CaMKII-tTA mouse[95]. Next, a head post was surgically attached on the mouse skull. After complete recovery from surgery and habituation to the imaging setup (~ 2 months), the mouse was briefly anesthetized by isoflurane inhalation in a

chamber, and subsequently its head immobilized in the imaging apparatus. The mouse remained awake for the entire duration of the experiment. Imaging runs were split into sixty epochs of 10 s each (i.e. total imaging duration = 10 min) and images acquired under blue light illumination at an exposure time of 50 ms at 15 fps. Within each epoch, a 300 ms auditory stimulus was presented at the 3s time point. The auditory stimulus was randomized to be either 4 kHz or 24 kHz. A total of 30 stimulus presentations for each 4 kHz and 24 kHz were conducted. This procedure was then repeated under green light and red laser illumination. The green light and laser imaging were done at 50 ms and 10 ms exposure times, respectively. The frame rate remained ~15 fps. The auditory stimulus generated

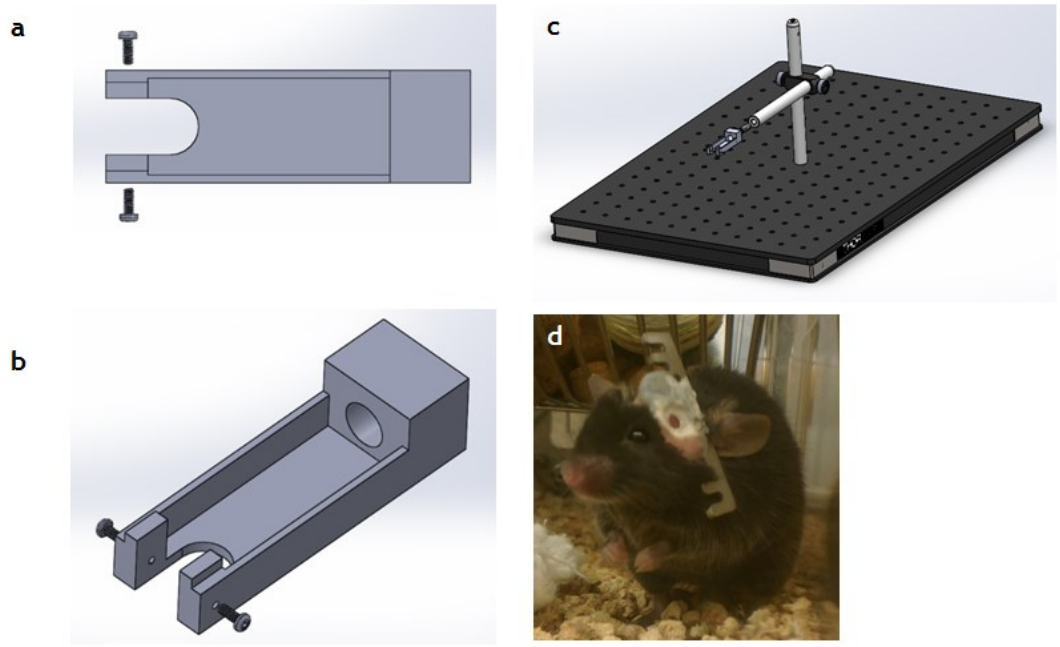

Supplementary Figure 3.3 Setup for the functional imaging experiment. (a-b) Top and side views of the head mount used in the auditory stimulus experiment. The head mount has a threaded hole which can be used to attach it firmly on an optical bread board. (c) The head mount shown attached to an optical breadboard. (d) A mouse bearing the steel head-post necessary for fixing its head during the experiment.

a pulse that flashed the *sync* channel LED at the beginning of each 10 min trial. This enabled the microscope data and the stimuli to be time-synced. Each image acquired by the microscope was time-stamped with ms temporal resolution.

Arousal from anesthesia experiment: A thinned-skull cranial window was prepared on a female Fisher (22g) mouse. The animal was anesthetized with 0.45 mL of ketamine/xylazine within the scope of 2 hours needed for the surgery,

microscope fixation and the administration of the dextran conjugated FITC dye (0.2 mL, 10 mg/kg, 70 kDa). Images were continuously acquired under blue light illumination (50 ms, 15 fps) while the dye was being injected. Imaging was continuously carried out for the next 200 mins until the mouse showed signs of being fully awake. During this period, a stack of 100 red laser images (5 ms exposure time) and 10 green light images (100 ms exposure time) were acquired every minute.

3.4.8 Image processing

Laser speckle contrast: LSC was calculated by processing a stack of red laser images. The speckle contrast (k) at each pixel (x, y) is calculated as[12]:

$$k(x,y) = \frac{\sigma(x,y)}{\mu(x,y)} \quad (1)$$

Here, μ and σ are the mean and standard deviation of light intensity at each pixel in the chosen image stack. The image stack size depends on the frame rate and temporal resolution desired for the LSC image. I.e. with 15 fps, a 4s time resolution will allow a stack of 60 images.

The speckle contrast (k) is related to blood flow speed by[12]:

$$k^2 = \frac{\tau}{2T}\left\{2 - \frac{\tau}{T}\left[1 - exp\left(-\frac{2T}{\tau}\right)\right]\right\} \quad (2)$$

Here exposure time is denoted by T and τ denotes the decorrelation coefficient, a quantity inversely proportional to blood flow speed. For small τ values

(associated with typical microcirculation imaged by our microscope), eq. 2 can be simplified to:

$$\frac{1}{\tau} \propto \frac{1}{k^2} \quad (3)$$

Eq. 3 was used to compute CBF speed.

Microscope validation: Benchtop images were registered to microscope images by performing a landmark-based image registration (ImageJ, TurboReg). Correlation coefficients for the blue, green, and laser speckle contrasted images were calculated after 5×5 pixel median filtering, and background subtraction with a radius of 50 pixels (ImageJ). A 20×20 pixel grid over the central 400×400 pixel FoV was used to calculate the correlation coefficients. The same procedures were performed on a 20×20 pixel region of the FoV for calculations of the correlation coefficients for red light absorption images. However, no background subtraction step was used as the emphasis was on correlating temporal variations.

Optical functional imaging experiment: Images from the last 25 trials (out of 30) for each stimulus presentation was used to calculate the neuronal activation maps. Since the image sensor frame rate can vary slightly, each image was time-stamped at ms temporal resolution. This permitted the acquired images to be resampled to a temporal resolution of 10 ms (Matlab) using linear interpolation. Then, both calcium and hemodynamic responses were calculated as (ImageJ):

$$r(t) = \frac{x(t) - \bar{x}_B}{\bar{x}_B} \quad (4)$$

Here, $r(t)$ is the calculated response, $x(t)$ the measured variable, and $\bar{x}_B$ is the baseline (0 – 3 s) mean of the measured variable. In the case of calcium fluorescence imaging, the light reflectance levels were taken as the measured variable. For HbT and dHb imaging, inverted green light and red laser light images were used respectively, while the relative blood flow levels calculated by LSC were used for CBF.

Wide area functional mapping analogous to classic task-based fMRI processing: The overall signal processing model is schematically shown in **Figure 3.4a, b**. Here, the effect of a stimulus specific hemodynamic response function (the 'activation' time-course), and the presence of a cortex wide hemodynamic fluctuation (the 'background' time-course) were factored in to derive the spatial distribution of fit coefficients for both, the stimulus-specific activation and the background fluctuation in hemodynamics. An error term was also included.

The hemodynamic data was first spatially median filtered (3×3 pixel window), and then temporally filtered (2 Hz low-pass filter) to remove noise. Then, a preliminary version of the 'activation' time-course was created by taking the average hemodynamic time-course for a region exhibiting peak neural activity (identified as a 'hotspot' from the maximum intensity projection of calcium signals, **Figure 3.4a**). The 'background' time-course was computed by taking the cortex-wide average. This 'background' time-course was then subtracted from the 'hotspot' time-course to produce the 'activation' time-course (**Figure 3.4a**).

The filtered hemodynamic data, together with these two time-courses was input to a least-squares regression model[135] as shown below (**Figure 3.4b**):

$$r(t) = c_0 + c_1 a(t) + c_2 g(t) + e(t) \quad (5)$$

Here, $a(t)$ and $g(t)$ are the 'activation' and 'background' time-courses, respectively. c_1 and c_2 are their corresponding 'fit coefficients' computed by the model. $r(t)$ is the measured hemodynamic response, $e(t)$ is the error term and c_0 is an offset adjusting constant.

This pipeline was performed separately for HbT and CBF hemodynamics. The CBF hemodynamics underwent further 20×20 pixel mean filtering to remove additional noise before being input to the model. The entire procedure was first performed for 4 kHz stimulus data and then repeated for the 24 kHz stimulus data.

Arousal from anesthesia experiment: Hemodynamics of individual vessel segments were analyzed by removing the effects of two factors: a) the background signal, and b) the fluctuations in incident illumination intensity. The estimated background signal was removed by applying a background subtraction

Band	Stop band 1 (Hz)	Pass band 1 (Hz)	Pass band 2 (Hz)	Stop band 2 (Hz)	Type	Order
Delta			4	5	Lowpass FIR	500
Theta	3	4	7	8	Bandpass FIR	500
Alpha	7	8	15	16	Bandpass FIR	500
Beta	15	16	31	32	Bandpass FIR	500
Notch	58	59	61	62	Bandstop FIR	500
Gamma	31	32	100	101	Bandpass FIR	500

Supplementary Table 3.1 Filter settings for electrophysiology.

filter (ImageJ, 50 pixel radius). For green and red light absorption images, the images were inverted before subtracting the background. For LSC Flow images, background was directly subtracted. Fluctuations in illumination intensity affected only the absorption images. LSC flow images are immune to incident intensity variations. Therefore, the background subtracted inverted green/red images were divided by an indicator of the incident illumination level. We chose a heavily smoothed version of the non-inverted green/red light image (200×200 pixels) to approximate the incident light levels. Finally, an artery and a vein region (30x30 pixels each) were chosen for displaying hemodynamic trends.

3.4.9 EEG signal processing

EEG was recorded at 12207 Hz (Tucker Davis Technologies, FL). We down-sampled the EEG data by a factor of 40 for subsequent processing (Matlab). Bandpass filters were implemented for the standard EEG frequency bands: delta, theta, alpha, beta and gamma (**Supplementary Table 3.1**). Additionally, to filter power-line noise, a 50 Hz notch-filter was implemented before passing the EEG data through the gamma filter. Signal power in each band was calculated by computing the filtered signal variance in 1 min blocks. A 3 sample median filter was added to reduce noise. The total EEG power was taken as the summation of powers across the five bands.

3.5 Acknowledgements

This research was funded by NCI grant no. 1R21CA175784-01 and P30 NS050274. The authors wish to thank Mr. Jay Burns of Johns Hopkins University for help with microscope fabrication, Mr. B. Douglas Ward of the Medical College of Wisconsin for assistance with signal processing and Drs. Ingie Hong and Richard Huganir for providing transgenic mice.

Chapter 4 **A Novel Optical Imaging Platform for Characterizing Tumor Hemodynamics at Microvascular Spatial Resolution**

Optical imaging enables one to characterize tumor hemodynamics *in vivo* at microvascular spatial scales. However, most optical imaging systems are capable of acquiring images with a single contrast mechanism, and therefore can only interrogate a single hemodynamic variable. This precludes understanding the complex role of hemodynamics in the tumor microenvironment. To overcome this barrier, we developed a novel multi-contrast optical imaging system that can simultaneously interrogate *in vivo* microvascular scale changes in (i) tumor perfusion, (ii) blood volume, and (iii) intravascular oxygen saturation over the entire spatial extent of the tumor. Herein we present the development of the imaging system, a multi-contrast image processing pipeline and initial results from *in vivo* imaging of an orthotopic breast tumor model.

4.1 Introduction

A tumor's microvasculature (and hemodynamic microenvironment) is crucial to its survival[136-138]. Therefore, tumor vasculature represents a potent target for arresting tumor progression. This new class of vascular targeted agents is known

as antiangiogenics[117, 139, 140]. In addition, traditional treatment regimens such as chemotherapy and radiation therapy are profoundly impeded by aberrant tumor hemodynamics. For example, leaky tumor microvessels often cause chemotherapeutic agents to leak into the interstitial space before reaching their intended targets. Hypoxia due to inadequate perfusion permits tumor cells to survive DNA damage caused by radiation therapy[141-143]. Therefore, *in vivo* characterization of tumor hemodynamics is a crucial step in understanding tumor biology and therapeutic strategies.

Many tumor studies, such as those performed with magnetic resonance imaging (MRI)[144-146] and positron emission tomography (PET)[147-149], do not have the spatial resolution to characterize hemodynamic events at their native: i.e. microvascular, spatial scale. Optical imaging methods, such as intrinsic optical signals (IOS) imaging[91] and laser speckle contrast (LSC) imaging[12], are capable of overcoming this barrier by resolving tumor hemodynamics at the level of individual microvessels. However, these optical methods are often performed one at a time: i.e. only IOS imaging to reveal oxygenation[9, 150] or only LSC imaging to reveal tumor perfusion[10], but not both at the same time. Hence, these studies are incapable of assessing the multi-faceted and complex nature of tumor hemodynamics.

To address this unmet need, we developed a novel multi-contrast optical imaging platform that enables concurrent interrogation of tumor (i) perfusion (blood flow), (ii) blood volume, and (iii) intravascular oxygen saturation. Our system acquires a

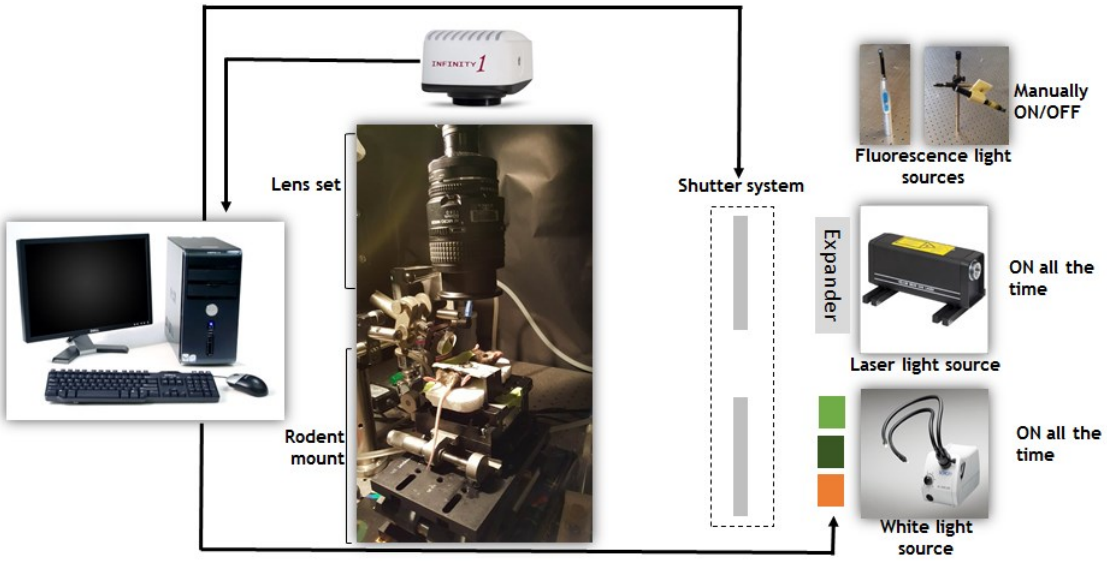

Figure 4.1 Schematic of the imaging assembly. Fluorescent illumination sources are switched on/off manually as they are used only once during each imaging session. The rest of the illumination sources: white light and laser, are controlled via two shutters by an automated program running in the personal computer (PC). The rodent is mounted on a focusing stage within a custom built contraption. Images acquired through the highly sensitive camera are directly fed to the personal computer which dynamically stores them. Both the control of illumination sources and the image acquisition are synchronized by the same master program running on the personal computer.

field of view (FoV) as wide as 5 x 5 mm at a microvascular resolution of 5 μm and can acquire images continuously for extended durations (hours).

4.2 Results

4.2.1 A benchtop based multi-contrast optical imaging system

We built a benchtop based optical imaging system that combines three optical contrast mechanisms: green fluorescence (FL), laser speckle contrast (LSC) and intrinsic optical signals (IOS). **Figure 4.1** shows a schematic of our system. Green FL was used to visualize the spatial extent of green fluorescent protein (GFP) tagged tumor cell growth (**Detailed Methods**). LSC was used to create maps of relative tumor perfusion (**Detailed Methods**). Finally, IOS signals acquired under 560, 570 and 600 nm illumination were used to create maps of total hemoglobin (equivalent to blood volume) and intravascular oxygen saturation (**Detailed Methods**). The surgically prepared mouse was mounted on a custom holder for *in vivo* imaging (**Detailed Methods**).

Our system operates with a 5 μm spatial resolution and covers a FoV of 5 x 5 mm. Each multi-contrast cycle of imaging (i.e. perfusion, blood volume and intravascular oxygen saturation) takes 30 seconds to complete. This frame rate enabled us to acquire images over extended durations (~hours) without unnecessarily using up memory capacity. The benchtop based design provided ample space to conveniently perform surgical and experimental manipulations required for imaging the orthotopic breast tumor model.

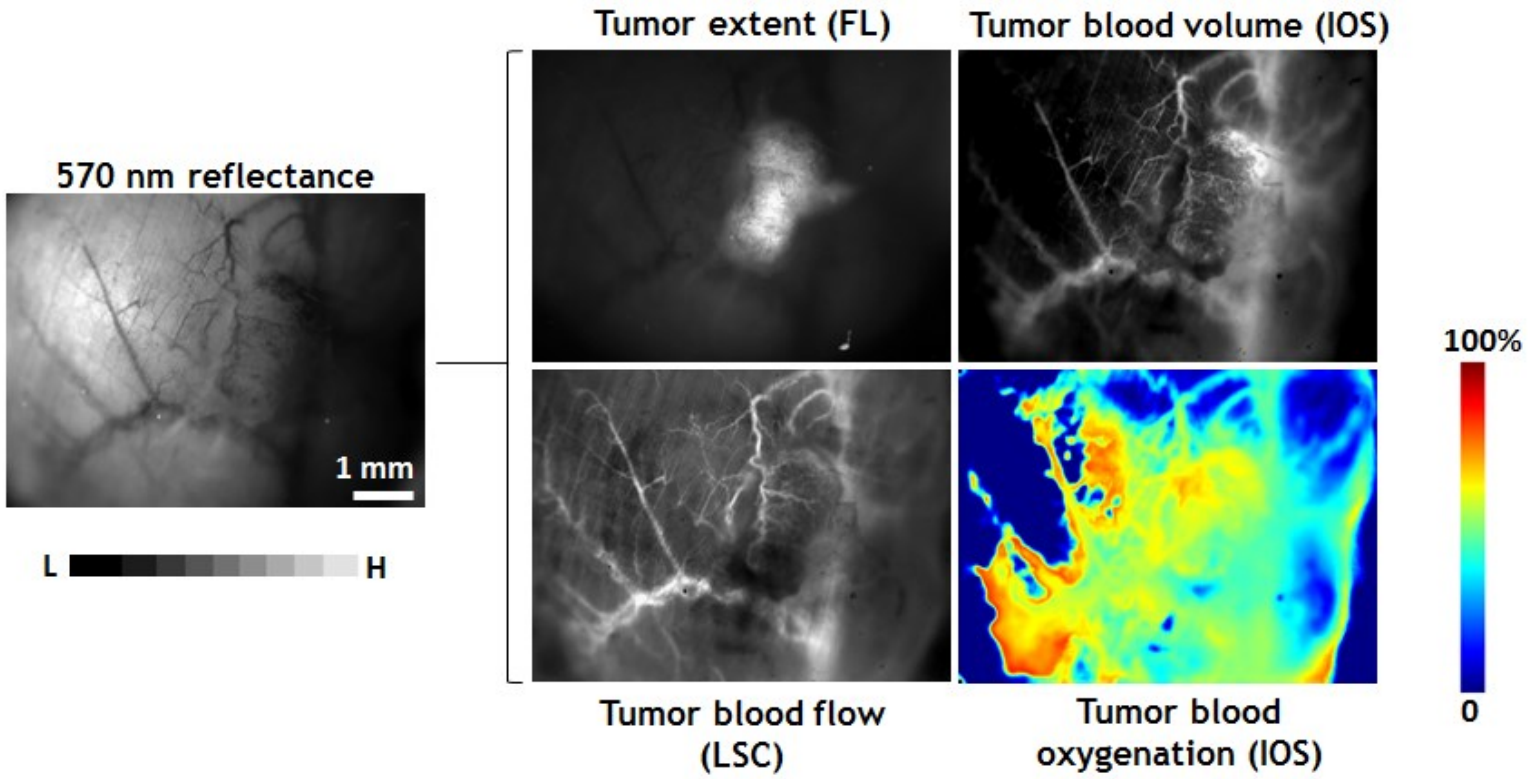

Figure 4.2 Co-localized tumor microenvironment variables. A 570 nm green light reflectance image is shown on the left as a reference. Four tumor microenvironment variables are shown on the right: tumor extent with fluorescence imaging of GFP tagged tumor cells, tumor blood flow from LSC, and tumor blood volume and intravascular oxygenation with IOS imaging. The oxygen saturation map is shown in pseudo-color for visualization purposes.

4.2.2. Colocalized visualization of tumor physiology

We used our system to image both tumor extent and tumor hemodynamic variables in an orthotropic breast tumor model (**Detailed Methods**)**.** Briefly, female athymic nude mice were inoculated with GFP tagged MDA-MB-231 human breast tumor cells in the 4^{th} mammary fat pad. The tumor was allowed to grow for 1 – 2 weeks after which the animal was anesthetized, surgically prepared and imaged for several hours.

Figure 4.2 shows a representative example. A 570 nm green light absorption image is shown on the left hand side to indicate the level of information obtained by visual inspection. The panel on the right shows four tumor variables. The tumor extent is visualized by imaging the GFP tagged tumor cells with green fluorescence (FL). Tumor blood flow is visualized via laser speckle contrast (LSC) imaging. Tumor blood volume and oxygen saturation is computed using multi-wavelength IOS signals (**Detailed Methods**).

A traditional single contrast imaging approach would have revealed only one of these four variables. However, multi-contrast imaging enables us to observe how the entire tumor extent (**Figure 4.2**, FL) is overlaid with a highly angiogenic microvascular architecture (**Figure 4.2**, blood volume) that is inadequately perfused (**Figure 4.2**, depression in blood flow) with low oxygen content blood (**Figure 4.2**, depression in intravascular oxygen saturation).

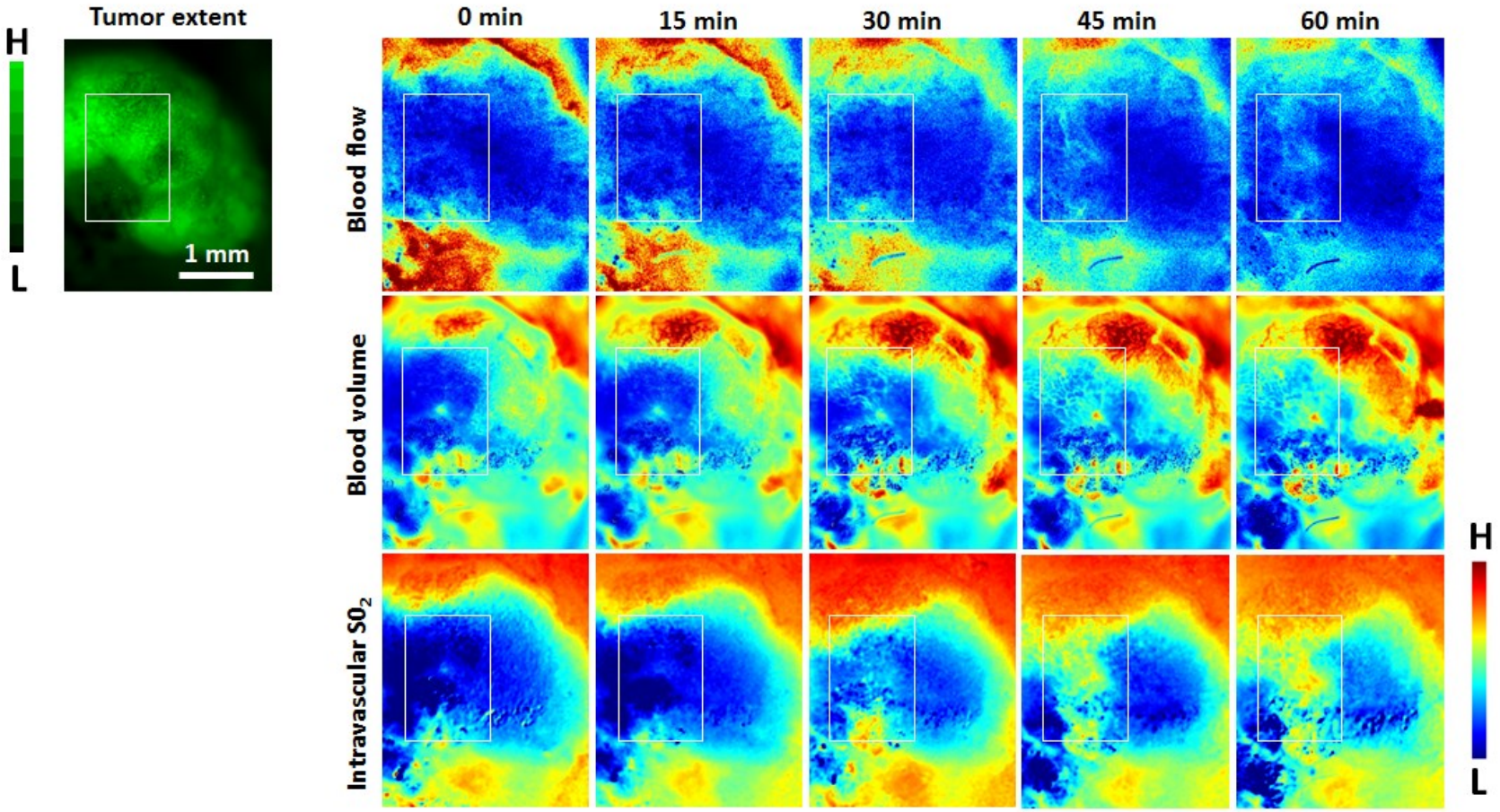
H
L
Tumor extent
1 mm
0 min
15 min
30 min
45 min
60 min
Blood flow
Blood volume
Intravascular SO_2
H
L

Figure 4.3 Monitoring variations in tumor hemodynamics (example one). Tumor extent is shown on left (green color coded image of tumor GFP fluorescence). The panel on the right shows how perfusion (blood flow), bold volume (HbT) and intravascular SO_2 fluctuate within an hour. Each image set was normalized to its 99^{th} percentile to clearly show spatial dynamics. The scale bar of 1 mm applies for all images. A white box is overlaid on each image to indicate a region of interest (ROI) where vascular reperfusion occurs.

4.2.3. Monitoring instabilities in tumor hemodynamics

We then used our imaging system to monitor *in vivo* microvascular scale spatio-temporal instabilities in tumor hemodynamics over the entire tumor extent. We performed this task continuously for two hours. To the best of our knowledge, this is a first of its kind tumor image acquisition. **Figure 4.3** shows a representative example of tumor hemodynamic instabilities over the first hour of recording. A green color coded GFP fluorescence image is shown on the left as a reference for the tumor extent. The panel on the right shows how three hemodynamic variables: perfusion, blood volume and intravascular oxygen saturation, evolve over time. A white box indicates a region of interest (ROI) wherein vascular reperfusion occurred (**Figure 4.3,** blood flow). Concomitantly, entire segments of microvessels 'appeared' in the blood volume map (**Figure 4.3**, blood volume). A similar pattern was observed in intravascular oxygen saturation (**Figure 4.3**, intravascular oxygen saturation), reflecting the higher levels of blood oxygen saturation in the newly perfused area.

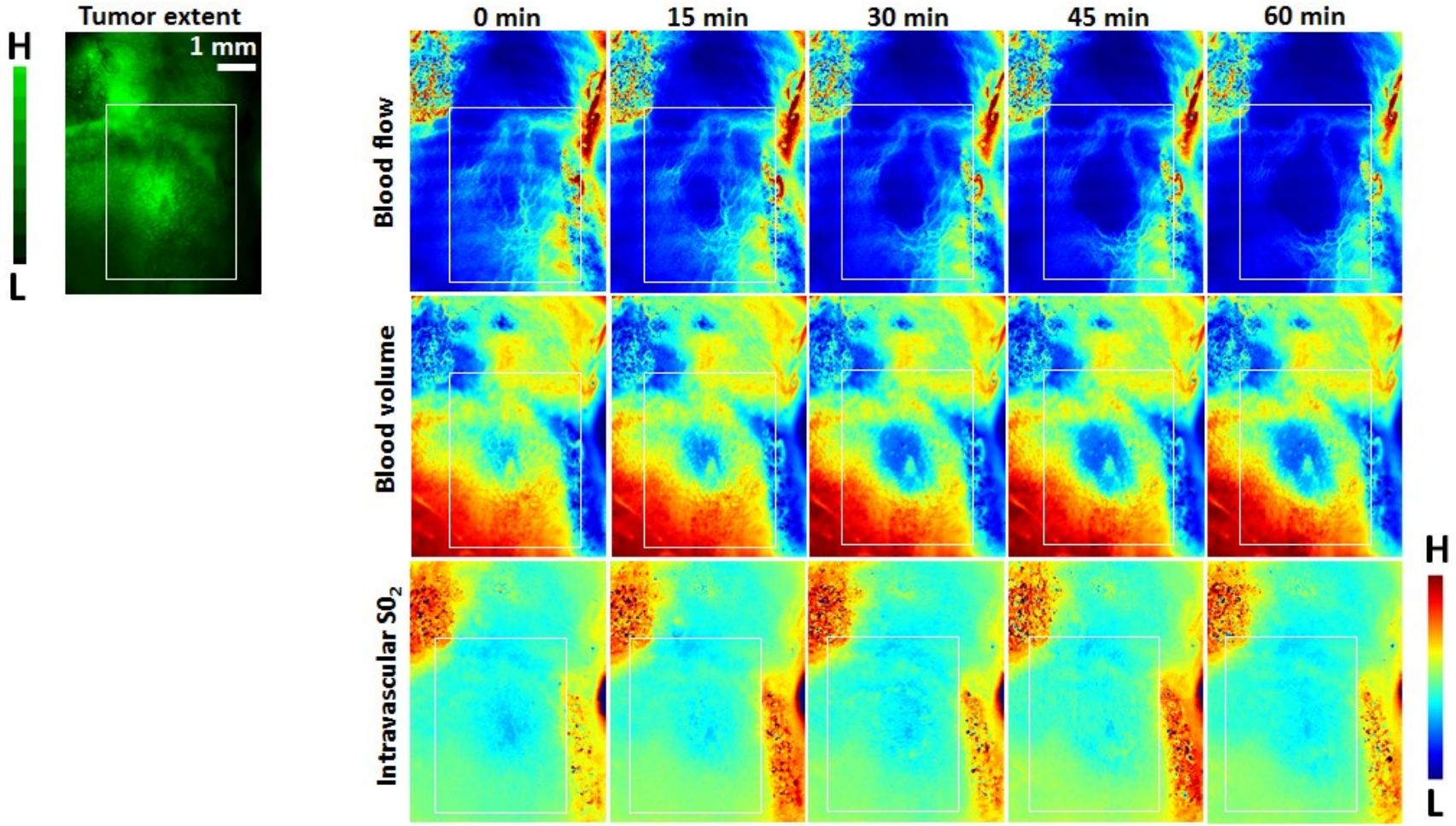
Tumor extent
H
L
1 mm
0 min
15 min
30 min
45 min
60 min
Blood flow
Blood volume
Intravascular SO_2
H
L

Figure 4.4 Monitoring instabilities in tumor hemodynamics (example two). Tumor extent is shown on left (green color coded image of tumor GFP fluorescence). The panel on the right shows how perfusion (blood flow), bold volume (HbT) and intravascular SO_2 fluctuate within an hour. Each image set was normalized to its 99^{th} percentile to clearly show spatial dynamics. The scale bar of 1 mm applies for all images. A white box is overlaid on each image to indicate a region of interest (ROI) where a significant reduction in vascular perfusion occurs.

Figure 4.4 shows another such example. However, in this case the hemodynamic instability is the opposite: i.e. perfusion and blood volume in a section of the tumor (**Figure 4.4**, white box) diminished over time while the intravascular oxygen saturation remained low.

4.2.4. Microvascular correlation analysis

We then developed a processing pipeline to quantify these diverse changes in tumor hemodynamics at the scale of individual microvessels. Here we have shown our processing pipeline applied on the dataset used in **Figure 4.2**. 30 minutes of continuously acquired hemodynamic data were used.

First, we manually annotated and segmented all the microvessel segments in the tumor region (**Figure 4.5a**). This enabled us to select each microvessel segment and interrogate hemodynamic quantities on a microvascular basis (**Figure 4.5b**). **Figure 4.5c-e** shows mean blood volume, blood flow and intravascular oxygen saturation for each microvessel segment.

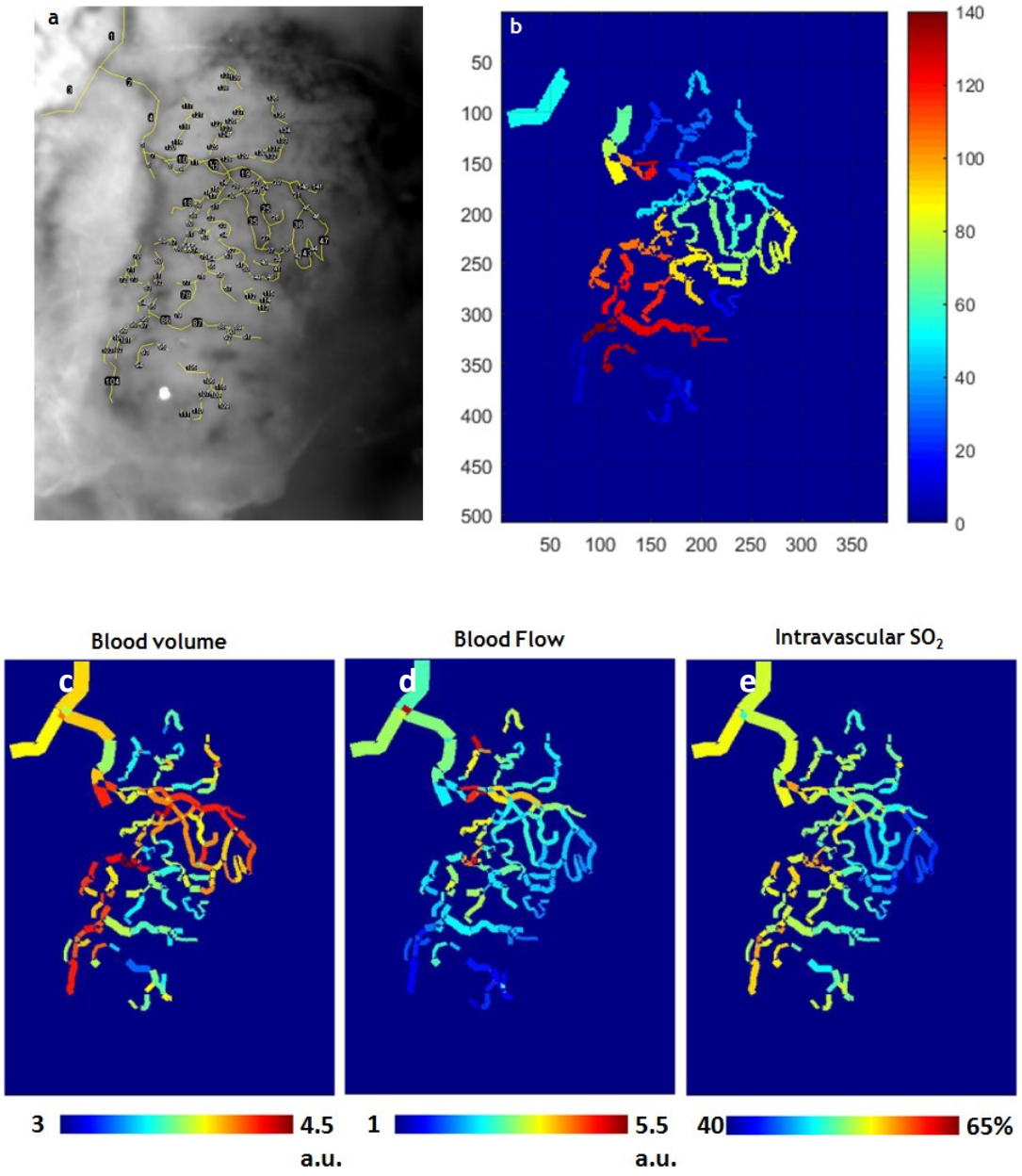

Figure 4.5 Microvessel segmentation. (a) Annotated microvessel segments. (b) Each vessel segment color coded by the segment number.(c-e) shows the average blood volume, blood flow and vascular oxygen saturation for each microvessel segment, respectively. An area of 400 x 500 pixels: 2 mm x 2.5 mm is shown.

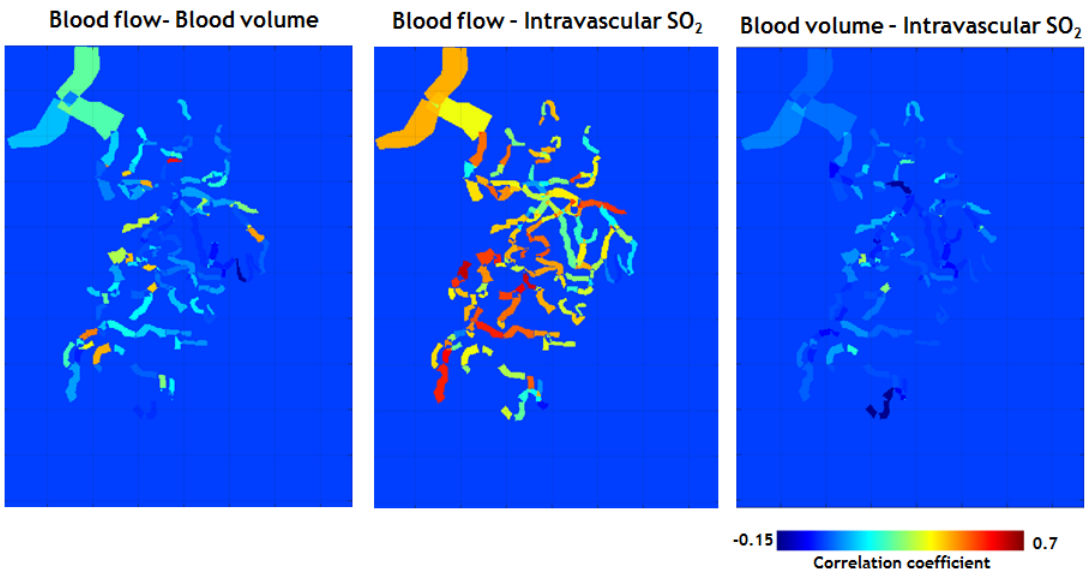

Figure 4.6 Correlation between hemodynamic quantities at microvascular scale. All quantities are calculated over 30 minutes of continuous recording (at a sample rate of 2 samples per minute)

We then correlated the three hemodynamic variables with each other for each microvessel segment (**Figure 4.6**). For this specific tumor example, a moderate correlation was observed between perfusion (blood flow) and intravascular oxygen saturation. Blood volume was not correlated with blood flow, or with the level of intravascular oxygen saturation. This lack of correlation suggests that microvascular blood flow was not dictated by local vasodilation or constriction in this specific instance.

We plan to apply this processing pipeline to a larger cohort of tumors and extensively characterize the spatio-temporal relationships among microvascular scale tumor hemodynamics.

4.3 Discussion

Here we reported a novel microvascular resolution, multi-contrast optical imaging platform and demonstrated its utility by colocalizing and concurrently interrogating relationships between tumor perfusion, blood volume and intravascular oxygen saturation.

Historically, attempts to interrogate multiple tumor hemodynamic variables relied on high frame rate video microscopy[141, 151, 152] (to visualize and count erythrocytes in motion) or point based flow measurements[153] (e.g. laser doppler flowmetry), and microelectrode based perivascular oxygen partial pressure measurements[141, 151-153]. Owing to the high magnification needed to visualize individual erythrocytes, the video microscopy approach only yielded a limited field of view (FoV), and was unable to cover the entire tumor. Furthermore, counting of individual erythrocytes to establish blood flow speeds was extremely tedious. Therefore, counting was performed only on selected microvessels. Point based blood flow measurements needed a measuring probe for each new spatial location to be interrogated. Therefore, both the video microscopy and point based techniques were not sufficient to observe tumor–wide hemodynamics at its native spatial resolution. The microelectrode approach for oxygenation also suffered from the same limitation as point based flow measures. Therefore the number of measurement sites was restricted. Our multi-contrast optical imaging platform overcomes all the above limitations, and enables truly wide field (5 x 5 mm) interrogation of blood flow, blood volume and intravascular oxygen saturation at microvascular (5 μm) spatial resolution over the entire tumor extent.

First, we colocalized blood flow, blood volume and intravascular oxygen saturation with tumor extent (**Figure 4.2**). These maps showed a clear depression in blood flow and intravascular oxygen saturation and the development of angiogenic microvessels within the tumor. As expected, this trend was common to all tumors. We then used our imaging system to continuously monitor dynamic changes in these quantities over hours. This enabled us to observe multi-variable hemodynamic instabilities previously not reported (**Figure 4.3** and **Figure 4.4**). We also demonstrated a processing pipeline to correlate such hemodynamic variables at the microvascular scale.

We envision several exciting additions to our experimental and imaging capabilities. A chronical window preparation[154] would permit us to perform longitudinal studies. This would also allow us to assess complex microvascular scale alterations induced by various cancer treatment paradigms and link them to survival outcome. Supplementing our hemodynamic imaging platform with methods of tumor metabolism imaging (such as glucose uptake and mitochondrial membrane potential)[155] would enable us to map alterations in tumor metabolism to corresponding multi-variable hemodynamic variations.

Our processing pipeline can be extended to support more advanced forms of analysis. For example, comparison of microvascular scale hemodynamic correlations (such as those in **Figure 4.6**) among healthy and tumor bearing subjects may reveal how the presence of a tumor affects subtle changes in microvascular level hemodynamic correlations. A Sholl analysis with the distribution of correlation statistics mapped as a function of their proximity to

tumor epicenter may be used as a marker for early tumor detection. We can also investigate the correlation among different microvessel segments for each hemodynamic quantity. This may reveal how different sub-sets of tumor microvessels coordinate local perfusion.

We intend to apply our novel imaging system and processing pipeline to extensively characterize spatio-temporal relationships in tumor hemodynamics at its native microvascular scale. With its current capabilities and capacity for improvements, we believe this work will inspire a new branch of tumor research that seeks to illuminate the complex role of hemodynamics within the tumor microenvironment.

4.4 Detailed Methods

4.4.1 The multi-contrast optical imaging system

We used three types of illumination sources, one each for each image contrast mechanism. For fluorescence (FL) imaging, either a UV curing gun (400 – 480 nm) or a green laser (532 nm) was used. The UV curing gun was used to excite green fluorescence protein (GFP) where tumor cells were tagged with GFP. A 496 nm longpass filter was used as an emission filter. No excitation filter was used. The green laser coupled with a 555 nm $\pm$ 25 nm Bandpass emission filter was kept as a standby for exciting varieties of red fluorescence dyes if needed. Typically, a quick succession of fluorescent images is taken at the beginning of

each experiment to establish tumor extent. The excitation light source is then switch off to allow other imaging modalities for the rest of the imaging session.

A 632 nm laser light source coupled with a beam expander was used to perform laser speckle contrast (LSC) imaging. For intrinsic optical signal (IOS) imaging, a broadband white light source was used in conjunction with a programmable filter wheel. The filter wheel contains four filters (560, 570, 600 and 610 $\pm$ 5 nm), an empty slot to pass white light when needed, and a dark slot to block the white light.

Both the laser light and the white light were kept switched on for the entire imaging session. A custom built shutter system was used to selectively exclude each illumination source when needed.

The rodent to be imaged was mounted on an X-Y-Z focusing stage. Image acquisition was performed through a high quality Nikon lens set coupled to a 16 bit CCD camera. The image acquisition, shutter selection as well as the filter wheel position where controlled electronically via a central program (written in Matlab) operating in the PC.

This imaging system achieved 10 frames per second temporal resolution while imaging a 5 x 5 mm field of view with 5 μm resolution. Conversely, the spatial resolution can be shrunk (10 - 20 μm) to observe a wider (10 x 10 – 20 x 20 mm) field of view.

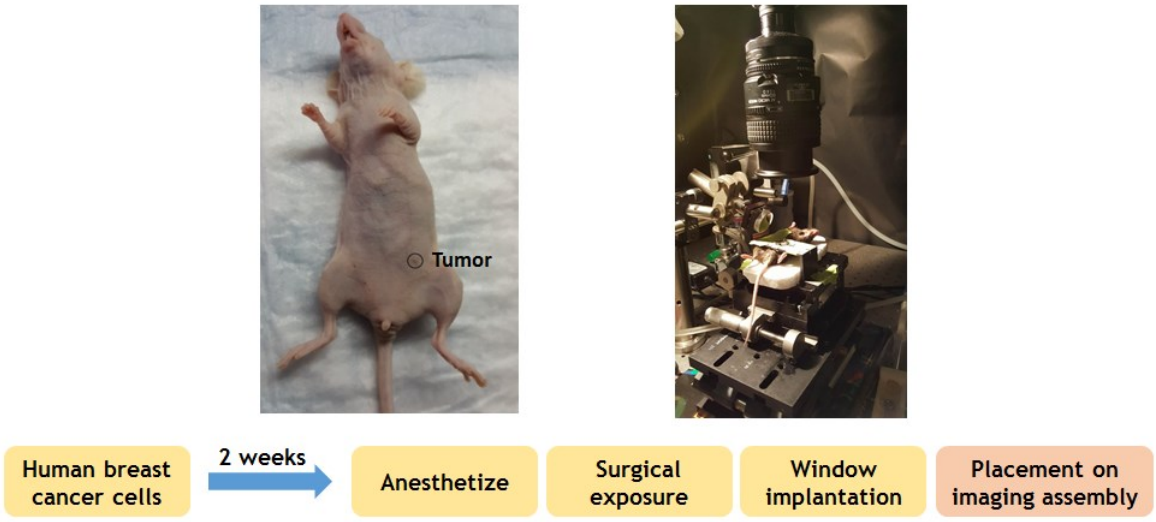

Supplementary Figure 4.1 Schematic of the animal model

4.4.2 The orthotopic breast tumor model

Almost all widefield optical imaging studies that resolve individual tumor microvessels have been performed on heterotopic tumor models. That is, the tumors are implanted in an environment not native to them. The most common example is the rodent dorsal skinfold chamber for tumor innoculation[150, 156]. Such heterotopic models sandwich the tumor within a small (few mm) thickness, and minimize the scattering experienced by light, thereby allowing high resolution imaging. On the other hand, most orthotopic environments allow unrestricted growth space for the tumor, and are embedded deep inside layers of tissue, thereby causing extensive light scattering, and thus poor image quality.

We sought to achieve a middle ground between these two extremes by inoculating human breast tumor cells superficially on a rodent's mammary fat pad, and imaging them early in their growth stage. The superficial inoculation

allows for clear optical access with a careful surgical preparation, and imaging during the early stages of the tumor (i.e. when the tumor is only 1 – 2 mm) allows capturing images representative of the whole tumor. **Supplementary Figure 4.1** shows the overall process.

4.4.3 Tumor inoculation procedure

All animal related procedures were approved by the Johns Hopkins University Animal Care and Use Committee (JHUACUC). Female athymic nude mice (~ 25 g, 3 months old) were anesthetized via intraperitoneal (IP) injection of a mixture of ketamine (90 mg/kg), xylazine (5 mg/kg), and saline. After checking the depth of the anesthetic with forepaw or tail stimulation via a pinch, the mouse was placed on a cotton surgical pad. 0.5 Million tumor cells (MDA-MB-231, GFP tagged) suspended in 0.5 mL of Hank's Balanced Salt Solution (HBSS) was injected from a U-100 insulin syringe to the $4/5^{th}$ mammary fat pad through one of its nipples. The mouse is allowed to regain consciousness and is monitored daily for tumor size. The tumor was surgically exposed and imaged between 2-3 weeks post inoculation.

4.4.4 Surgical preparation for imaging

The mice were anesthetized via an intraperitoneal (IP) injection of a mixture of ketamine (90 mg/kg), xylazine (5 mg/kg), and saline. After checking the depth of the anesthetic with forepaw or tail stimulation via a pinch, the mouse was placed on a cotton surgical pad. Eye ointment was spread over the mouse's eyes to prevent dehydration. The mouse was laid on its back such that the tumor on the

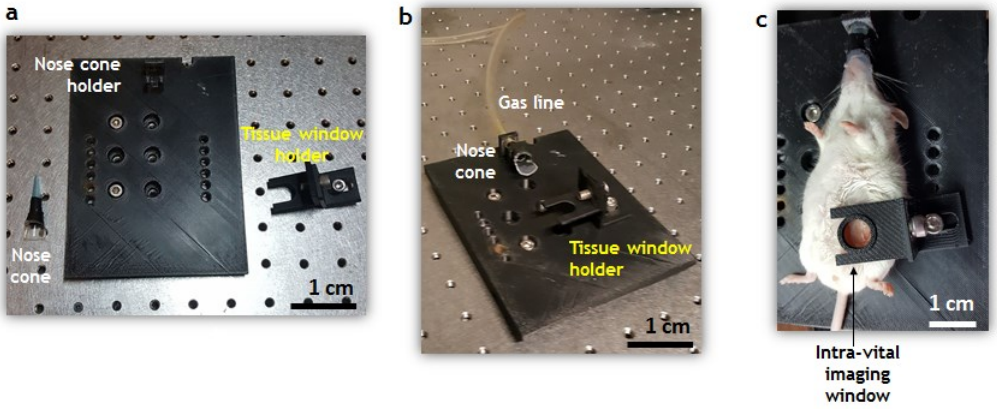

Supplementary Figure 4.2 3D printed mouse holder and mammary fat pad window. (a-b) The mouse holder. (c) A practice mouse placed on the mouse holder with the window implanted atop the 4th mammary fat pad

4th nipple/mammary fat pad was visible. A subcutaneous incision was made 1 to 1.5 cm away from the tumor. The skin was separated from the underlying tissue by spreading the tips of the surgical scissor towards the direction of the tumor. When the tumor is located, it was exposed as much as possible without damaging the surrounding vessels. If there was any connective tissue that is independent of the tumor and the surrounding vessels, it was removed carefully with fine scissors. A 3D-printed mount was fitted on the body with cyanoacrylate so that the tumor was at the center of circular mount (**Supplementary Figure 4.2**). Then, the mount was fit onto a custom holder attached to the frame of the imaging stage. After the cyanoacrylate was completely dry, it was filled with saline and a glass coverslip was placed on top of the mount. When the mouse began to gain consciousness, anesthesia was induced and maintained thereafter by inhalation of minimal levels of isoflurane (0.2 ~ 0.5%) mixed with room air

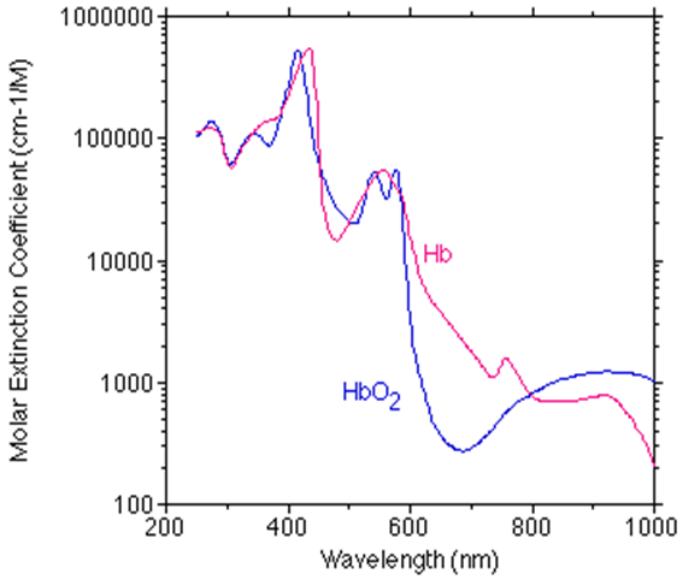

Supplementary Figure 4.3 Wavelength dependent absorption characteristics of deoxyhemoglobin (Hb) and oxyhemoglobin (HbO_2).

(1L/min). Throughout the experiment, the depth of anesthesia was frequently checked with isoflurane levels being adjusted accordingly (maximum of 1%).

4.4.5 Intrinsic optical signal processing

Biological tissue contains two species of hemoglobin: deoxy- and oxy-hemoglobin, that dominate absorption at visible light wavelengths (400 – 700 nm) [157]. Therefore, the amount of visible light absorbed by a particular mass of biological tissue indicates the amount of hemoglobin species within that mass. As indicated in **Supplementary Figure 4.3**, each of the hemoglobin species has distinct wavelength dependent absorption characteristics[158]. Therefore, by

combining absorption levels at multiple optical wavelengths, it is possible to estimate the level of each hemoglobin species, and, estimate the amount of total hemoglobin (equivalent to blood volume) and the level of blood oxygen saturation.

This can be showing with the following mathematical formulation that uses the modified Beer-Lambert Law[159].

$$I_r(\lambda) = I_{in}(\lambda) \times e^{-a} \times f_b \quad (2.1)$$

Where,

λ = wavelength of light.

I_{in} = Amount of light illuminating the biological tissue.

I_r = Amount of light returning from the biological tissue. I.e. the reflectance level recorded in the captured image.

f_b = The fraction of back scattered light.

a = Amount of light absorption by both species of hemoglobin.

Therefore, by taking $\varepsilon_{Hb}(\lambda)$ and $\varepsilon_{HbO}(\lambda)$as the absorption of deoxy- and oxy-hemoglobin at wavelengthλ, we can write

$$a = \varepsilon_{Hb}(\lambda) \times [Hb] + \varepsilon_{HbO}(\lambda) \times [HbO] \quad (2.2)$$

Here, $[Hb]$ and $[HbO]$ are deoxy- and oxy-hemoglobin amounts, respectively.

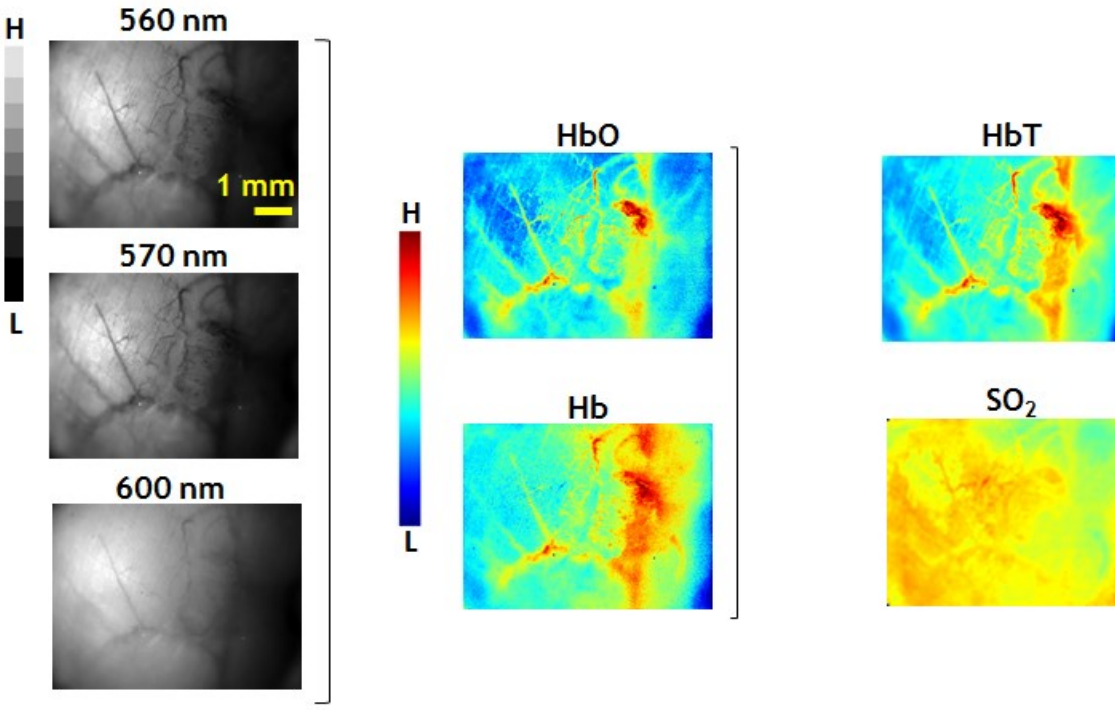

Supplementary Figure 4.4 Calculation of hemoglobin quantities and oxygen saturation from IOS wavelengths.

Now, by taking the natural logarithm on both sides of Eq. 2.1, and inserting values from Eq. 2.2, we have:

$$ln[I_r(\lambda)] = ln[I_{in}(\lambda) \times f_b] - \varepsilon_{Hb}(\lambda) \times [Hb] - + \varepsilon_{HbO}(\lambda) \times [HbO] \quad (2.3)$$

The above linear equation has four unknowns. One unknown $ln[I_{in}(\lambda) \times f_b]$ can be reasonably assumed to be constant in the narrow wavelength range (i.e. between 560 nm – 610 nm) we perform imaging. Therefore, by imaging in three separate wavelengths 560 nm, 570 nm and 600 nm, we can write the following formulation of Eq. 2.3:

$$\begin{bmatrix} ln[I_r(560\,nm)] \\ ln[I_r(570\,nm)] \\ ln[I_r(600\,nm)] \end{bmatrix} = \begin{bmatrix} 1 & \varepsilon_{Hb}(560\,nm) & \varepsilon_{HbO}(560\,nm) \\ 1 & \varepsilon_{Hb}(570\,nm) & \varepsilon_{HbO}(570\,nm) \\ 1 & \varepsilon_{Hb}(600\,nm) & \varepsilon_{HbO}(600\,nm) \end{bmatrix} \times \begin{bmatrix} ln[I_{in} \times f_b] \\ [Hb] \\ [HbO] \end{bmatrix} \quad (2.4)$$

Thus, by solving the set of linear equations in (2.4), we can arrive at:

$$[HbT] = [Hb] + [HbO] \quad (2.5)$$

And,

$$S_{O_2} = \frac{[HbO]}{[HbT]} \times 100\% \quad (2.6)$$

Supplementary Figure 4.4 shows a pictorial representation of this process.

Note1: According to the modified Beer Lambert Law[159], what we calculated as 'hemoglobin amounts' is actually the multiplication between the hemoglobin concentration and optical path length. We assume optical path length to remain constant, hence consider the above calculated quantities as equivalent to the actual hemoglobin concentrations.

Note 2: The above formulation assumed that $I_{in}(\lambda)$ is constant among the closely spaced optical wavelengths used. However, this is not true. Measurements on a test sample revealed that the 570 nm illumination is 16% less than the other two wavelengths. We added this as a correction factor before arriving at the final values.

Note 3: The wavelength dependence of the image sensor's sensitivity to received light is another factor that needs to be considered. However, the measurements indicated in Note 2 above were performed with the same image

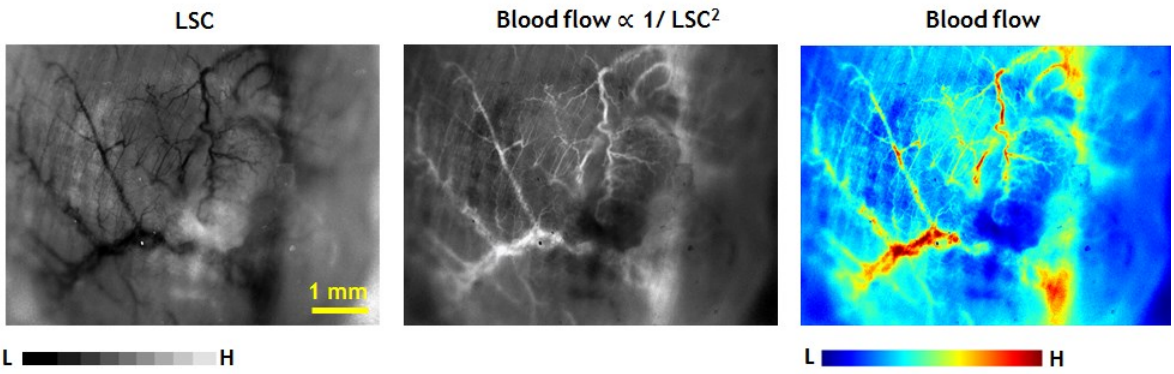

Supplementary Figure 4.5 : Results of laser speckle contrast imaging.

sensor. Hence, the modification above automatically addressed this consideration.

Note 4: Wavelength dependence of scattering was not factored in, as it would complicate the above model.

4.4.6 Laser speckle contrast processing

Laser Speckle Contrast (LSC) imaging[160, 161] is a label free technique that enables visualization of relative blood flow values. In simple terms, blood flowing within vessels behaves as a 'virtual contrast agent'[162] to highlight flow characteristics. One can calculate a quantity termed laser speckle contrast (LSC), by taking the ratio between the standard deviation (σ) and mean (μ) of light intensity in a stack of images:

$$LSC(x,y) = \frac{\sigma(x,y)}{\mu(x,y)} \tag{2.7}$$

Here, (x,y) are pixel co-ordinates. In practice, this quantity can then be approximated to reveal a relative blood flow level by the relationship[163]:

$$Blood\ flow \propto \frac{1}{LSC^2} \quad (2.8)$$

Supplementary Figure 4.5 shows a sample set of LSC and blood flow images (of the same field of view as the IOS images) obtained through laser speckle contrast calculations.

4.5 Acknowledgements

This research was funded by NCI grant no. 1R01CA196701-01.

Chapter 5 **Conclusions and Future Directions**

The goal of this research was to develop multi-contrast optical methods to enable new biological observations *in vivo* that were not possible with extant imaging system. We developed two such new imaging systems and accompanying processing pipelines for: (i) a miniature rodent head-mountable microscope for imaging both neural and hemodynamic activity in awake animals and (ii) a custom built benchtop based imaging system to interrogate blood flow, volume and oxygenation at microvascular resolution within an orthotopic tumor microenvironment.

Our miniaturized imaging system has the capability to interrogate both neural and hemodynamic activity in a freely moving rodent. We introduced a novel mode of analysis analogous to fMRI processing using multi-contrast optical data to provide functional mapping at microvascular resolution. We envision the addition of several supplementary capabilities. These can be either in the form of additional modalities of recording that supplement imaging (e.g. direct electrophysiology measurements through a transparent ECoG grid[71], neurochemical recording with an integrated chemical sensor[164] etc.), as well as means of interfering with the biology observed (e.g. electrical[165] or optogenetic[166] stimulation etc.). Another promising avenue would be to completely remove the microscope tethers: i.e. go wireless (by mounting an ultra-miniaturized control

and storage module on the back of the animal), thereby enabling chronic and even multi-animal imaging. With its current capabilities, and its adaptability to include optogenetic stimulations as well as electrophysiology recordings, we believe our microscope could herald a new era in neuroscientific research.

Our benchtop imaging system enabled us to co-localize tumor extent with three tumor hemodynamic variables: blood flow, blood volume and intravascular oxygen saturation. This allowed us to visualize concomitant multi-faceted tumor hemodynamics at the microvascular scale over the course of hours. The exquisite level of microvascular detail enabled us to explore correlations among these hemodynamic variables at the scale of individual microvessels. The variability and heterogeneity of the observed results suggest the need for a rigorous analytical framework for assessing microvascular resolution tumor hemodynamic data that may permit characterizing tumor microenvironments from a completely new standpoint.

In summary, this dissertation endeavors to introduce multi-contrast optical imaging as an enabling tool to explore biology *in vivo* at the microvascular scale in a more complete manner than previously possible. We believe our work will inspire future generations to push the imaging envelope further with these technologies.

Bibliography

1. Ferezou, I., Bolea, S. & Petersen, C. C. H. Visualizing the cortical representation of whisker touch: voltage-sensitive dye imaging in freely moving mice. *Neuron* **50**, 617-629 (2006).

2. Ghosh, K. K. *et al*. Miniaturized integration of a fluorescence microscope. *Nat. Methods* **8**, 871-878 (2011).

3. Sigal, I. et al. *Chronic monitoring of cortical hemodynamics in behaving, freely-moving rats using a miniaturized head-mounted optical microscope* (SPIE BiOS, International Society for Optics and Photonics, 2016).

4. Miao, P., Lu, H., Liu, Q., Li, Y. & Tong, S. Laser speckle contrast imaging of cerebral blood flow in freely moving animals. *J. Biomed. Opt.* **16**, 90502 (2011).

5. Ringuette, D., Jeffrey, M. A., Carlen, P. L. & Levi, O. *Multi-modal in vivo imaging of brain blood oxygenation, blood flow and neural calcium dynamics during acute seizures* (SPIE BiOS, International Society for Optics and Photonics, 2016).

6. Bouchard, M. B., Chen, B. R., Burgess, S. A. & Hillman, E. M. C. Ultra-fast multispectral optical imaging of cortical oxygenation, blood flow, and intracellular calcium dynamics. *Opt. Express* **17**, 15670-15678 (2009).

7. Jain, R. K. *et al*. Angiogenesis in brain tumours. *Nature Reviews Neuroscience* **8**, 610-622 (2007).

8. Chambers, A. F. *et al*. Steps in tumor metastasis: new concepts from intravital videomicroscopy. *Cancer Metastasis Rev.* **14**, 279-301 (1995).

9. Sorg, B. S., Moeller, B. J., Donovan, O., Cao, Y. & Dewhirst, M. W. Hyperspectral imaging of hemoglobin saturation in tumor microvasculature and tumor hypoxia development. *J. Biomed. Opt.* **10**, 044004-044004-11 (2005).

10. Rege, A. *et al*. Longitudinal in vivo monitoring of rodent glioma models through thinned skull using laser speckle contrast imaging. *J. Biomed. Opt.* **17**, 126017-126017 (2012).

11. Yu, H. et al. *Effect of cranial window type on monitoring neurovasculature using laser speckle contrast imaging* (SPIE BiOS, International Society for Optics and Photonics, 2016).

12. Senarathna, J., Rege, A., Nan Li & Thakor, N. V. Laser Speckle Contrast Imaging: Theory, Instrumentation and Applications. *IEEE Rev. Biomed. Eng.* **6**, 99-110 (2013).

13. Heeger, D. J. & Ress, D. What does fMRI tell us about neuronal activity? *Nat. Rev. Neurosci.* **3**, 142-151 (2002).

14. Nasrallah, I. & Dubroff, J. An overview of PET neuroimaging. *Semin. Nucl. Med.* **43**, 449-461 (2013).

15. Cianfoni, A., Colosimo, C., Basile, M., Wintermark, M. & Bonomo, L. Brain perfusion CT: principles, technique and clinical applications. *Radiol. Med.* **112**, 1225-1243 (2007).

16. Zhang, J., Campbell, R. E., Ting, A. Y. & Tsien, R. Y. Creating new fluorescent probes for cell biology. *Nat. Rev. Mol. Cell Biol.* **3**, 906-918 (2002).

17. Kerr, J. N. & Denk, W. Imaging in vivo: watching the brain in action. *Nature Reviews Neuroscience* **9**, 195-205 (2008).

18. Tye, K. M. & Deisseroth, K. Optogenetic investigation of neural circuits underlying brain disease in animal models. *Nat. Rev. Neurosci.* **13**, 251-266 (2012).

19. Theer, P., Hasan, M. T. & Denk, W. Two-photon imaging to a depth of 1000 μm in living brains by use of a Ti: Al2O3 regenerative amplifier. *Opt. Lett.* **28**, 1022-1024 (2003).

20. Bonhomme, V. *et al*. Influence of anesthesia on cerebral blood flow, cerebral metabolic rate, and brain functional connectivity. *Curr Opin Anaesthesiol* **24**, 474-479 (2011).

21. Theuwissen, A. J. P. CMOS image sensors: State-of-the-art. *Solid-State Electronics* **52**, 1401-1406 (2008).

22. Dombeck, D. A., Khabbaz, A. N., Collman, F., Adelman, T. L. & Tank, D. W. Imaging large-scale neural activity with cellular resolution in awake, mobile mice. *Neuron* **56**, 43-57 (2007).

23. Ng, D. C. *et al*. An implantable and fully integrated complementary metal-oxide semiconductor device for in vivo neural imaging and electrical interfacing with the mouse hippocampus. *Sensors and Actuators a-Physical* **145**, 176-186 (2008).

24. Ng, D. C., Tokuda, T., Shiosaka, S., Tano, Y. & Ohta, J. Implantable microimagers. *Sensors* **8**, 3183-3204 (2008).

25. Haruta, M. *et al*. An implantable CMOS device for blood-flow imaging during experiments on freely moving rats. *Japanese Journal of Applied Physics* **53** (2014).

26. Kerr, J. N. & Nimmerjahn, A. Functional imaging in freely moving animals. *Curr. Opin. Neurobiol.* **22**, 45-53 (2012).

27. Jones, P. B. *et al*. Simultaneous multispectral reflectance imaging and laser speckle flowmetry of cerebral blood flow and oxygen metabolism in focal cerebral ischemia. *J. Biomed. Opt.* **13**, 11 (2008).

28. Ferezou, I., Bolea, S. & Petersen, C. C. Visualizing the cortical representation of whisker touch: voltage-sensitive dye imaging in freely moving mice. *Neuron* **50**, 617-629 (2006).

29. Flusberg, B. A. *et al*. High-speed, miniaturized fluorescence microscopy in freely moving mice. *Nat. Methods* **5**, 935-938 (2008).

30. Helmchen, F., Fee, M. S., Tank, D. W. & Denk, W. A miniature head-mounted two-photon microscope: high-resolution brain imaging in freely moving animals. *Neuron* **31**, 903-912 (2001).

31. Sawinski, J. *et al*. Visually evoked activity in cortical cells imaged in freely moving animals. *Proc. Natl. Acad. Sci. U. S. A.* **106**, 19557-19562 (2009).

32. Liu, R. *et al*. Extendable, miniaturized multi-modal optical imaging system: cortical hemodynamic observation in freely moving animals. *Opt. Express* **21**, 1911-1924 (2013).

33. Bassi, A., Fieramonti, L., D'Andrea, C., Mione, M. & Valentini, G. In vivo label-free three-dimensional imaging of zebrafish vasculature with optical projection tomography. *J. Biomed. Opt* **16**, 3 (2011).

34. Mutoh, H., Perron, A., Akemann, W., Iwamoto, Y. & Knöpfel, T. Optogenetic monitoring of membrane potentials. *Exp. Physiol.* **96**, 13-18 (2011).

35. Mittmann, W. *et al*. Two-photon calcium imaging of evoked activity from L5 somatosensory neurons in vivo. *Nat. Neurosci.* **14**, 1089-1093 (2011).

36. Chalfie, M., Tu, Y., Euskirchen, G., Ward, W. W. & Prasher, D. C. Green fluorescent protein as a marker for gene expression. *Science* **263**, 802-805 (1994).

37. McVea, D. A., Mohajerani, M. H. & Murphy, T. H. Voltage-sensitive dye imaging reveals dynamic spatiotemporal properties of cortical activity after spontaneous muscle twitches in the newborn rat. *The Journal of Neuroscience* **32**, 10982-10994 (2012).

38. Petersen, C. C. H., Grinvald, A. & Sakmann, B. Spatiotemporal dynamics of sensory responses in layer 2/3 of rat barrel cortex measured in vivo by voltage-sensitive dye imaging combined with whole-cell voltage recordings and neuron reconstructions. *The Journal of Neuroscience* **23**, 1298-1309 (2003).

39. Mank, M. *et al*. A genetically encoded calcium indicator for chronic in vivo two-photon imaging. *Nature Methods* **5**, 805-811 (2008).

40. Murayama, M., Perez-Garci, E., Luscher, H. R. & Larkum, M. E. Fiberoptic system for recording dendritic calcium signals in layer 5 neocortical pyramidal cells in freely moving rats. *J. Neurophysiol.* **98**, 1791-1805 (2007).

41. Cha, J., Paukert, M., Bergles, D. E. & Kang, J. U. *Fiber optic fluorescence microscopy for functional brain imaging in awake mobile mice*, International Society for Optics and Photonics, 2014).

42. Osman, A. et al. *A head-mountable microscope for high-speed fluorescence brain imaging* (BioCAS, IEEE, 2011).

43. Osman, A. *et al*. Design Constraints for Mobile, High-Speed Fluorescence Brain Imaging in Awake Animals. *IEEE Trans. Biomed. Circuits Syst.* **6**, 446-453 (2012).

44. Park, J. H. *et al*. Head-mountable high speed camera for optical neural recording. *J. Neurosci. Methods* **201**, 290-295 (2011).

45. O'Sullivan, T. D. *et al*. 3756575; Real-time, continuous, fluorescence sensing in a freely-moving subject with an implanted hybrid VCSEL/CMOS biosensor. *Biomed Opt Express* **4**, 1332-1341 (2013).

46. Göbel, W., Kerr, J. N. D., Nimmerjahn, A. & Helmchen, F. Miniaturized two-photon microscope based on a flexible coherent fiber bundle and a gradient-index lens objective. *Opt. Lett.* **29**, 2521-2523 (2004).

47. Piyawattanametha, W. *et al*. In vivo brain imaging using a portable 2.9 g two-photon microscope based on a microelectromechanical systems scanning mirror. *Opt. Lett.* **34**, 2309-2311 (2009).

48. Sawinski, J. *et al*. Visually evoked activity in cortical cells imaged in freely moving animals. *Proc. Natl. Acad. Sci. U. S. A.* **106**, 19557-19562 (2009).

49. Greenberg, D. S. & Kerr, J. N. D. Automated correction of fast motion artifacts for two-photon imaging of awake animals. *J. Neurosci. Methods* **176**, 1-15 (2009).

50. Barretto, R. P., Messerschmidt, B. & Schnitzer, M. J. 2849805; In vivo fluorescence imaging with high-resolution microlenses. *Nat Methods* **6**, 511-512 (2009).

51. Helmchen, F., Denk, W. & Kerr, J. N. Miniaturization of two-photon microscopy for imaging in freely moving animals. *Cold Spring Harb Protoc.* **2013**, 904-913 (2013).

52. Holzer, M. et al. *4D functional imaging in the freely moving rat*, IEEE, 2006).

53. Engelbrecht, C. J., Voigt, F. & Helmchen, F. Miniaturized selective plane illumination microscopy for high-contrast in vivo fluorescence imaging. *Opt. Lett.* **35**, 1413-1415 (2010).

54. Saunter, C. D., Semprini, S., Buckley, C., Mullins, J. & Girkin, J. M. Micro-endoscope for in vivo widefield high spatial resolution fluorescent imaging. *Biomedical optics express* **3**, 1274-1278 (2012).

55. Adelsberger, H., Garaschuk, O. & Konnerth, A. Cortical calcium waves in resting newborn mice. *Nature Neuroscience* **8**, 988-990 (2005).

56. Dombeck, D. A., Harvey, C. D., Tian, L., Looger, L. L. & Tank, D. W. Functional imaging of hippocampal place cells at cellular resolution during virtual navigation. *Nat. Neurosci.* **13**, 1433-1440 (2010).

57. Hillman, E. M. C. Optical brain imaging in vivo: techniques and applications from animal to man. *J. Biomed. Opt.* **12**, 051402 (2007).

58. Rege, A., Senarathna, J., Li, N. & Thakor, N. V. Anisotropic Processing of Laser Speckle Images Improves Spatiotemporal Resolution. *IEEE Transactions on Biomedical Engineering* **59**, 1272-1280 (2012).

59. Ts'o, D.,Y., Frostig, R. D., Lieke, E. E. & Grinvald, A. Functional organization of primate visual cortex revealed by high resolution optical imaging. *Science* **249**, 417-420 (1990).

60. Murari, K. *et al*. Contrast-enhanced imaging of cerebral vasculature with laser speckle. *Appl. Opt.* **46**, 5340-5346 (2007).

61. Murari, K., Greenwald, E., Etienne-Cummings, R., Cauwenberghs, G. & Thakor, N. *Design and characterization of a miniaturized epi-illuminated microscope* (Engineering in medicine and biology society, 2009. EMBC 2009. Annual international conference of the IEEE, IEEE, 2009).

62. Murari, K., Etienne-Cummings, R., Cauwenberghs, G. & Thakor, N. *An integrated imaging microscope for untethered cortical imaging in freely-moving animals* (Conf Proc IEEE Eng Med Biol Soc Ser. 2010, 2010).

63. Miao, P., Lu, H., Liu, Q., Li, Y. & Tong, S. Laser speckle contrast imaging of cerebral blood flow in freely moving animals. *J. Biomed. Opt.* **16**, 090502 (2011).

64. Kudo, C., Nozari, A., Moskowitz, M. A. & Ayata, C. The impact of anesthetics and hyperoxia on cortical spreading depression. *Exp. Neurol.* **212**, 201-206 (2008).

65. Senarathna, J., Murari, K., Etienne-Cummings, R. & Thakor, N. V. *Design of a novel head-mountable microscope system for laser speckle imaging*, IEEE, 2011).

66. Senarathna, J., Murari, K., Etienne-Cummings, R. & Thakor, N. V. A Miniaturized Platform for Laser Speckle Contrast Imaging. *Ieee Transactions on Biomedical Circuits and Systems* **6**, 437-445 (2012).

67. Duncan, D. D. & Kirkpatrick, S. J. Can laser speckle flowmetry be made a quantitative tool? *JOSA A* **25**, 2088-2094 (2008).

68. Dombeck, D. A., Graziano, M. S. & Tank, D. W. Functional clustering of neurons in motor cortex determined by cellular resolution imaging in awake behaving mice. *The Journal of Neuroscience* **29**, 13751-13760 (2009).

69. Liu, Y., Liao, L., Chan, S. J., Bandla, A. & Thakor, N. V. *An integrated neuroprotective intervention for brain ischemia validated by ECoG-fPAM* (EMBC, IEEE, 2016).

70. Szuts, T. A. *et al*. A wireless multi-channel neural amplifier for freely moving animals. *Nat. Neurosci.* **14**, 263-269 (2011).

71. Ledochowitsch, P., Olivero, E., Blanche, T. & Maharbiz, M. M. *A transparent μECoG array for simultaneous recording and optogenetic stimulation* (EMBC, IEEE, 2011).

72. Martin, C., Martindale, J., Berwick, J. & Mayhew, J. Investigating neural-hemodynamic coupling and the hemodynamic response function in the awake rat. *Neuroimage* **32**, 33-48 (2006).

73. Ringuette, D., Jeffrey, M. A., Carlen, P. L. & Levi, O. *Multi-modal in vivo imaging of brain blood oxygenation, blood flow and neural calcium dynamics during acute seizures* (Proc SPIE Int Soc Opt Eng Ser. 9690, International Society for Optics and Photonics, 2016).

74. Frostig, R. D., Wiesel, T. N., Grinvald, A., Lieke, E. & Gilbert, C. D. Functional architecture of cortex revealed by optical imaging of intrinsic signals. *Nature* **324**, 361-364 (1986).

75. Tian, P. *et al*. Cortical depth-specific microvascular dilation underlies laminar differences in blood oxygenation level-dependent functional MRI signal. *Proc. Natl. Acad. Sci. U. S. A.* **107**, 15246-15251 (2010).

76. Durduran, T. *et al*. Spatiotemporal quantification of cerebral blood flow during functional activation in rat somatosensory cortex using laser-speckle flowmetry. *J. Cereb. Blood Flow Metab.* **24**, 518-525 (2004).

77. Ma, Y. *et al*. Wide-field optical mapping of neural activity and brain haemodynamics: considerations and novel approaches. *Philos. Trans. R. Soc. Lond. B. Biol. Sci.* **371** (2016).

78. O'Herron, P. *et al*. Neural correlates of single-vessel haemodynamic responses in vivo. *Nature* **534**, 378–382 (2016).

79. Dunn, A. K. *et al*. Simultaneous imaging of total cerebral hemoglobin concentration, oxygenation, and blood flow during functional activation. *Opt. Lett.* **28**, 28-30 (2003).

80. Ma, Y. *et al*. Resting-state hemodynamics are spatiotemporally coupled to synchronized and symmetric neural activity in excitatory neurons. *Proc. Natl. Acad. Sci. U. S. A.* **113**, E8471 (2016).

81. Sun, N., Luo, W., Li, L. Z. & Luo, Q. Monitoring hemodynamic and metabolic alterations during severe hemorrhagic shock in rat brains. *Acad. Radiol.* **21**, 175-184 (2014).

82. Yu, H., Senarathna, J., Tyler, B. M., Thakor, N. V. & Pathak, A. P. Miniaturized optical neuroimaging in unrestrained animals. *Neuroimage* **113**, 397-406 (2015).

83. Osman, A. et al. *A head-mountable microscope for high-speed fluorescence brain imaging*, IEEE, 2011).

84. Ghosh, K. K. *et al*. 3810311; Miniaturized integration of a fluorescence microscope. *Nat Methods* **8**, 871-878 (2011).

85. Liu, R. *et al*. Extendable, miniaturized multi-modal optical imaging system: cortical hemodynamic observation in freely moving animals. *Optics Express* **21**, 1911-1924 (2013).

86. Munro, E. A., Levy, H., Ringuette, D., O'Sullivan, T. D. & Levi, O. Multi-modality optical neural imaging using coherence control of VCSELs. *Opt. Express* **19**, 10747-10761 (2011).

87. Sigal, I. et al. *Chronic monitoring of cortical hemodynamics in behaving, freely-moving rats using a miniaturized head-mounted optical microscope*, International Society for Optics and Photonics, 2016).

88. Miao, P., Lu, H., Liu, Q., Li, Y. & Tong, S. Laser speckle contrast imaging of cerebral blood flow in freely moving animals. *J. Biomed. Opt.* **16**, 090502 (2011).

89. Lu, H., Miao, P., Liu, Q., Li, Y. & Tong, S. *Dual-modal (OIS/LSCI) imager of cerebral cortex in freely moving animals* Ser. 8329, International Society for Optics and Photonics, 2011).

90. Osman, A. *et al*. Design constraints for mobile, high-speed fluorescence brain imaging in awake animals. *Biomedical Circuits and Systems, IEEE Transactions on* **6**, 446-453 (2012).

91. Hillman, E. M. Optical brain imaging in vivo: techniques and applications from animal to man. *J. Biomed. Opt.* **12**, 051402-051402-28 (2007).

92. Ebner, T. J. & Chen, G. Use of voltage-sensitive dyes and optical recordings in the central nervous system. *Prog. Neurobiol.* **46**, 463-506 (1995).

93. Lin, M. Z. & Schnitzer, M. J. Genetically encoded indicators of neuronal activity. *Nat. Neurosci.* **19**, 1142-1153 (2016).

94. Dombeck, D. A., Khabbaz, A. N., Collman, F., Adelman, T. L. & Tank, D. W. Imaging large-scale neural activity with cellular resolution in awake, mobile mice. *Neuron* **56**, 43-57 (2007).

95. Wekselblatt, J. B., Flister, E. D., Piscopo, D. M. & Niell, C. M. Large-scale imaging of cortical dynamics during sensory perception and behavior. *J. Neurophysiol.* **115**, 2852-2866 (2016).

96. Hillman, E. M. C. *et al*. Depth-resolved optical imaging and microscopy of vascular compartment dynamics during somatosensory stimulation. *Neuroimage* **35**, 89-104 (2007).

97. Boynton, G. M., Engel, S. A., Glover, G. H. & Heeger, D. J. Linear systems analysis of functional magnetic resonance imaging in human V1. *J. Neurosci.* **16**, 4207-4221 (1996).

98. Zuo, X. *et al*. Toward reliable characterization of functional homogeneity in the human brain: Preprocessing, scan duration, imaging resolution and computational space. *Neuroimage* **65**, 374-386 (2013).

99. Cox, R. W. AFNI: Software for Analysis and Visualization of Functional Magnetic Resonance Neuroimages. *Comput. Biomed. Res.* **29**, 162-173 (1996).

100. Issa, J. B. *et al*. Multiscale optical Ca2+ imaging of tonal organization in mouse auditory cortex. *Neuron* **83**, 944-959 (2014).

101. Horton, N. G. *et al*. In vivo three-photon microscopy of subcortical structures within an intact mouse brain. *Nat. Photon.* **7**, 205-209 (2013).

102. Hong, G. *et al*. Through-skull fluorescence imaging of the brain in a new near-infrared window. *Nature Photonics* **8**, 723-730 (2014).

103. Gu, L. *et al*. Long-term in vivo imaging of dendritic spines in the hippocampus reveals structural plasticity. *J. Neurosci.* **34**, 13948-13953 (2014).

104. Chisholm, K. I. *et al*. In Vivo Imaging of Flavoprotein Fluorescence During Hypoxia Reveals the Importance of Direct Arterial Oxygen Supply to Cerebral Cortex Tissue. *Adv. Exp. Med. Biol.* **876**, 233-239 (2016).

105. Jung, C. K. E. & Herms, J. Structural dynamics of dendritic spines are influenced by an environmental enrichment: an in vivo imaging study. *Cereb. Cortex* **24**, 377-384 (2014).

106. Schoknecht, K. *et al*. Monitoring stroke progression: in vivo imaging of cortical perfusion, blood-brain barrier permeability and cellular damage in the rat photothrombosis model. *J. Cereb. Blood Flow Metab.* **34**, 1791-1801 (2014).

107. Bergonzi, K. M., Bauer, A. Q., Wright, P. W. & Culver, J. P. Mapping functional connectivity using cerebral blood flow in the mouse brain. *J. Cereb. Blood Flow Metab.* **35**, 367-370 (2015).

108. Abdullah, H., Maddage, N. C., Cosic, I. & Cvetkovic, D. Cross-correlation of EEG frequency bands and heart rate variability for sleep apnoea classification. *Med. Biol. Eng. Comput.* **48**, 1261-1269 (2010).

109. Stosiek, C., Garaschuk, O., Holthoff, K. & Konnerth, A. In vivo two-photon calcium imaging of neuronal networks. *Proc. Natl. Acad. Sci. U. S. A.* **100**, 7319-7324 (2003).

110. Smetters, D., Majewska, A. & Yuste, R. Detecting action potentials in neuronal populations with calcium imaging. *Methods* **18**, 215-221 (1999).

111. Hirase, H., Qian, L., Barthó, P. & Buzsáki, G. Calcium Dynamics of Cortical Astrocytic Networks In Vivo. *PLoS Biol.* **2**, e96 (2004).

112. Otsu, Y. *et al*. Calcium dynamics in astrocyte processes during neurovascular coupling. *Nat. Neurosci.* **18**, 210-218 (2015).

113. Hoffman, R. Green fluorescent protein imaging of tumour growth, metastasis, and angiogenesis in mouse models. *Lancet Oncol.* **3**, 546-556 (2002).

114. MacDonald, T. J., Tabrizi, P., Shimada, H., Zlokovic, B. V. & Laug, W. E. Detection of brain tumor invasion and micrometastasis in vivo by expression of enhanced green fluorescent protein. *Neurosurgery* **43**, 1443 (1998).

115. Liu, Z., Tabakman, S., Welsher, K. & Dai, H. Carbon nanotubes in biology and medicine: In vitro and in vivo detection, imaging and drug delivery. *Nano Res.* **2**, 85-120 (2009).

116. Vivero-Escoto, J. L., Slowing, I. I., Trewyn, B. G. & Lin, V. S. -. Mesoporous Silica Nanoparticles for Intracellular Controlled Drug Delivery. *Small* **6**, 1952-1967 (2010).

117. Folkman, J. Tumor angiogenesis: therapeutic implications. *N. Engl. J. Med.* **285**, 1182-1186 (1971).

118. Raghunand, N., Gatenby, R. A. & Gillies, R. J. Microenvironmental and cellular consequences of altered blood flow in tumours. *Br. J. Radiol.* **76 Spec No 1**, 11 (2003).

119. Armitage, G. A., Todd, K. G., Shuaib, A. & Winship, I. R. Laser speckle contrast imaging of collateral blood flow during acute ischemic stroke. *J. Cereb. Blood Flow Metab.* **30**, 1432-1436 (2010).

120. Parthasarathy, A. B., Kazmi, S. M. S. & Dunn, A. K. Quantitative imaging of ischemic stroke through thinned skull in mice with Multi Exposure Speckle Imaging. *Biomed. Opt. Express* **1**, 246-259 (2010).

121. Luo, L. *et al*. Association between Hypoxia and Perinatal Arterial Ischemic Stroke: A Meta-Analysis. *PLoS One* **9**, e90106 (2014).

122. Jensen, R. L. Brain tumor hypoxia: tumorigenesis, angiogenesis, imaging, pseudoprogression, and as a therapeutic target. *J. Neurooncol.* **92**, 317-335 (2009).

123. Grinvald, A., Lieke, E., Frostig, R. D., Gilbert, C. D. & Wiesel, T. N. Functional architecture of cortex revealed by optical imaging of intrinsic signals. *Nature* **324**, 361-364 (1986).

124. Frostig, R. D., Lieke, E. E., Ts'o, D. Y. & Grinvald, A. Cortical functional architecture and local coupling between neuronal activity and the microcirculation revealed by in vivo high-resolution optical imaging of intrinsic signals. *Proc. Natl. Acad. Sci. U. S. A.* **87**, 6082-6086 (1990).

125. Tian, P. *et al*. Cortical depth-specific microvascular dilation underlies laminar differences in blood oxygenation level-dependent functional MRI signal. *Proc. Natl. Acad. Sci. U. S. A.* **107**, 15246-15251 (2010).

126. Gad, R. et al. *Miniature device for chronic, label-free multi-modal optical imaging of cortical hemodynamics in rats* (SPIE BiOS, International Society for Optics and Photonics, 2015).

127. Deisseroth, K. Optogenetics. *Nat. Methods* **8**, 26-29 (2011).

128. Ledochowitsch, P., Olivero, E., Blanche, T. & Maharbiz, M. M. *A transparent μECoG array for simultaneous recording and optogenetic stimulation*, IEEE, 2011).

129. Bauer, A. Q. *et al*. Optical imaging of disrupted functional connectivity following ischemic stroke in mice. *Neuroimage* **99**, 388-401 (2014).

130. Feng, S., Chao, Z., Zhang, B. & Miao, P. *An integrated device for simultaneously monitoring electrocorticography and cerebral blood flow in rat's brain* (BMEI, IEEE, 2014).

131. Ba, A. M. *et al*. Multiwavelength optical intrinsic signal imaging of cortical spreading depression. *J. Neurophysiol.* **88**, 2726-2735 (2002).

132. Dunn, A. K., Bolay, T., Moskowitz, M. A. & Boas, D. A. Dynamic imaging of cerebral blood flow using laser speckle. *Journal of Cerebral Blood Flow and Metabolism* **21**, 195-201 (2001).

133. Jiang, M. et al. *Dynamic Imaging of Cerebral Blood Flow Using Laser Speckle During Epileptic Events* (Biomedical Optics, Optical Society of America, 2012).

134. Zhao, M. *et al*. Optical triggered seizures using a caged 4-Aminopyridine. *Front. Neurosci.* **9** (2015).

135. Stigler, S. M. Gauss and the Invention of Least Squares. *The Annals of Statistics* **9**, 465-474 (1981).

136. Folkman, J. *Role of angiogenesis in tumor growth and metastasis* Ser. 29, Elsevier, 2002).

137. Fukumura, D. *et al*. Hypoxia and acidosis independently up-regulate vascular endothelial growth factor transcription in brain tumors in vivo. *Cancer Res.* **61**, 6020-6024 (2001).

138. Hanahan, D. & Weinberg, R. A. The hallmarks of cancer. *Cell* **100**, 57-70 (2000).

139. Hlatky, L., Hahnfeldt, P. & Folkman, J. Clinical application of antiangiogenic therapy: microvessel density, what it does and doesn't tell us. *J. Natl. Cancer Inst.* **94**, 883-893 (2002).

140. Badruddoja, M. A. *et al*. Antiangiogenic effects of dexamethasone in 9L gliosarcoma assessed by MRI cerebral blood volume maps. *Neuro Oncol.* **5**, 235-243 (2003).

141. Kimura, H. *et al*. Fluctuations in red cell flux in tumor microvessels can lead to transient hypoxia and reoxygenation in tumor parenchyma. *Cancer Res.* **56**, 5522-5528 (1996).

142. Chaplin, D. J., Olive, P. L. & Durand, R. E. Intermittent blood flow in a murine tumor: radiobiological effects. *Cancer Res.* **47**, 597-601 (1987).

143. Dewhirst, M. W., Cao, Y. & Moeller, B. Cycling hypoxia and free radicals regulate angiogenesis and radiotherapy response. *Nature Reviews Cancer* **8**, 425-437 (2008).

144. Jordan, B. F. *et al*. Dynamic contrast-enhanced and diffusion MRI show rapid and dramatic changes in tumor microenvironment in response to inhibition of HIF-1α using PX-478. *Neoplasia* **7**, 475-485 (2005).

145. Bradley, D. P. *et al*. Examining the acute effects of cediranib (RECENTIN, AZD2171) treatment in tumor models: a dynamic contrast-enhanced MRI study using gadopentate. *Magn. Reson. Imaging* **27**, 377-384 (2009).

146. Chertok, B. *et al*. Iron oxide nanoparticles as a drug delivery vehicle for MRI monitored magnetic targeting of brain tumors. *Biomaterials* **29**, 487-496 (2008).

147. Tyler, J. *et al*. Metabolic and hemodynamic evaluation of gliomas using positron emission tomography. *J. Nucl. Med.* **28**, 1123-1133 (1987).

148. Ahn, S. Y. *et al*. Prediction of microvascular invasion of hepatocellular carcinoma using gadoxetic acid-enhanced MR and 18F-FDG PET/CT. *Abdom. Imaging* **40**, 843-851 (2015).

149. Krause, B., Beck, R., Souvatzoglou, M. & Piert, M. PET and PET/CT studies of tumor tissue oxygenation. *The quarterly journal of nuclear medicine and molecular imaging* **50**, 28 (2006).

150. Sorg, B. S., Hardee, M. E., Agarwal, N., Moeller, B. J. & Dewhirst, M. W. Spectral imaging facilitates visualization and measurements of unstable and abnormal microvascular oxygen transport in tumors. *J. Biomed. Opt.* **13**, 014026-014026-11 (2008).

151. Dewhirst, M. W. *et al*. Microvascular studies on the origins of perfusion-limited hypoxia. *Br. J. Cancer Suppl.* **27**, S247-51 (1996).

152. Lanzen, J. *et al*. Direct demonstration of instabilities in oxygen concentrations within the extravascular compartment of an experimental tumor. *Cancer Res.* **66**, 2219-2223 (2006).

153. Braun, R. D., Lanzen, J. L. & Dewhirst, M. W. Fourier analysis of fluctuations of oxygen tension and blood flow in R3230Ac tumors and muscle in rats. *Am. J. Physiol.* **277**, H551-68 (1999).

154. Yuan, F. *et al*. Time-dependent vascular regression and permeability changes in established human tumor xenografts induced by an anti-vascular endothelial growth factor/vascular permeability factor antibody. *Proc. Natl. Acad. Sci. U. S. A.* **93**, 14765-14770 (1996).

155. Martinez, A. F. *Metaboloptics: In Vivo Optical Imaging to Enable Simultaneous Measurement of Glucose Uptake, Mitochondrial Membrane Potential, and Vascular Features in Cancer* (2016).

156. Fukumura, D., Duda, D. G., Munn, L. L. & Jain, R. K. Tumor Microvasculature and Microenvironment: Novel Insights Through Intravital Imaging in Pre-Clinical Models. *Microcirculation* **17**, 206-225 (2010).

157. Hillman, E. M. Optical brain imaging in vivo: techniques and applications from animal to man. *J. Biomed. Opt.* **12**, 051402-051402-28 (2007).

158. http://omlc.org/spectra/hemoglobin/summary.html.

159. Kohl, M. *et al*. Determination of the wavelength dependence of the differential pathlength factor from near-infrared pulse signals. *Phys. Med. Biol.* **43**, 1771 (1998).

160. Fercher, A. & Briers, J. D. Flow visualization by means of single-exposure speckle photography. *Opt. Commun.* **37**, 326-330 (1981).

161. Briers, J. D. Laser speckle contrast imaging for measuring blood flow. *Optica Applicata* **37**, 139 (2007).

162. Murari, K. *et al*. Contrast-enhanced imaging of cerebral vasculature with laser speckle. *Appl. Opt.* **46**, 5340-5346 (2007).

163. Boas, D. A. & Dunn, A. K. Laser speckle contrast imaging in biomedical optics. *J. Biomed. Opt.* **15**, 011109-011109-12 (2010).

164. Murari, K., Stanacevic, M., Cauwenberghs, G. & Thakor, N. V. Integrated potentiostat for neurotransmitter sensing. *IEEE Engineering in Medicine and Biology Magazine* **24**, 23-29 (2005).

165. Greenwald, E. *et al*. A CMOS Current Steering Neurostimulation Array With Integrated DAC Calibration and Charge Balancing. *IEEE Transactions on Biomedical Circuits and Systems* **PP**, 1-12 (2017).

166. Cardin, J. A. *et al*. Targeted optogenetic stimulation and recording of neurons in vivo using cell-type-specific expression of Channelrhodopsin-2. *Nat. Protocols* **5**, 247-254 (2010).

Curriculum Vita

Janaka Senarathna graduated with a first class in Electronics and Telecommunications Engineering from the University of Moratuwa, Sri Lanka in 2008. He was the department gold medalist and the joint recipient of the Prof. Dayantha S. Wijesekera Award for the Most Outstanding Graduate. Janaka spent a year in the Zone 24x7 – UoM research laboratory under the guidance of Drs. Ranga Rodrigo and Chulantha Kulasekere. He then joined Dr. Nitish V. Thakor's Neuroengineering and Biomedical Instrumentation laboratory at The Johns Hopkins University, Baltimore in 2009 to pursue a Master of Science in Engineering degree in Biomedical Engineering. After successfully finishing his Masters degree, Janaka join the PhD program at the same department where he conducted research under Drs. Arvind P. Pathak and Nitish V. Thakor. He is set to defend his doctoral work this March and intends to continue as a research fellow with Dr. Pathak. In addition to his academic activities, Janaka has extensively partaken and held the role of President/Co-President at the Hopkins Toastmasters Club (2012), Hopkins Biomedical Engineering PhD Students' Council (2013) and Johns Hopkins Biomedical Engineering Extramural

Development in Graduate Education (2013). Janaka is an avid fan of science fiction stories.